

Microwave-Catalyst Interactions in the Reforming of Hydrocarbons

by

Steven Edward Edmund

A dissertation submitted in partial fulfillment
of the requirements for the degree of
Doctor of Philosophy
(Chemical Engineering)
in The University of Michigan
2013

Doctoral Committee:

Professor Johannes W. Schwank, Chair
Adjunct Professor Galen B. Fisher
Associate Professor John E. Foster
Assistant Research Scientist Andrew R. Tadd
Professor Robert M. Ziff

© Steven E. Edmund 2013
All Rights Reserved

For My Family

ACKNOWLEDGEMENTS

Many people have contributed their thoughts and labor to this dissertation and I am extremely grateful to each of them for their guidance and wisdom along the way. Chief among those contributing to this collaborative effort is my advisor, Johannes Schwank, who has provided constant support and the space in which to learn and explore. Many members of the Schwank research group past and present have helped to hone my reasoning and presentation skills over the years. In particular, Sameer Parvathikar has been a constant companion in the journey through a Ph.D. and I am immensely thankful for his optimistic spirit and keen intellect. Andrew Tadd has also provided much guidance and I am thankful for his assistance in teaching me many analytical and experimental techniques.

Many thanks to my thesis committee, Andrew Tadd, Galen Fisher, Robert Ziff and John Foster for their wisdom and ideas along the way, providing insight beyond what is available in the literature and only known from years spent in lab. Two individuals who have had an immense impact on my life are Paul Laing and Robert McCabe of Ford Motor Company. They have been wonderful and supportive mentors along the way and the lessons I have learned from these two men will be lifelong.

There are an immense number of people at the University of Michigan and in Ann Arbor who have made my time in Michigan fun and enjoyable. I thank all of those friends and colleagues who have contributed to this wonderful environment. Many members of my family have been wonderfully supportive over the years including Debbie Colitas, Jennifer Osborn, David Osborn and Martha Osborn.

The bulk of my success is owed to my mother, Lois Edmund, who has been nothing but supportive over the years and has enabled me to learn and grow through her hard work and sacrifice. I am also thankful to my son, Henry, who has provided more motivation and perspective on life than anyone else possibly could.

Above all I must acknowledge my wife, Deborah. She has been a true partner in this endeavor, supporting me and encouraging me in challenging times. Her insights into my research have been invaluable and she has continually pushed me to expand my understanding and potential.

TABLE OF CONTENTS

DEDICATION	ii
ACKNOWLEDGEMENTS	iii
LIST OF FIGURES	viii
LIST OF TABLES	xiii
LIST OF APPENDICES	xv
LIST OF ABBREVIATIONS	xvi
ABSTRACT	xviii
CHAPTER	
I. Introduction to Catalytic Fuel Reforming and Microwaves	1
1.1 Current Energy Challenges	1
1.2 Literature Review	5
1.2.1 Introduction to Catalytic Hydrocarbon Reforming	5
1.2.2 Background of Microwave Heating	11
1.2.3 Microwave-Material Interactions	14
II. Microwave Effects on Carbon Deposition and Product Dis-	
tributions	17
2.1 Introduction	17
2.2 Experimental	19
2.2.1 Preliminary Experiments in Microwave Cavity Oper-	
ation	19
2.2.2 Catalyst Preparation	22
2.2.3 Flow Reactor Description	23
2.2.4 Reaction Conditions	30
2.2.5 Reactor Startup and Shutdown	32

2.2.6	Analysis of Reforming Behavior	33
2.2.7	Catalyst Characterization	34
2.3	Results	37
2.3.1	Partial Oxidation Experiments	37
2.3.2	Autothermal Reforming Experiments	39
2.3.3	Temperature Programmed Oxidation and Reduction	39
2.3.4	Raman Analysis	43
2.3.5	Surface Area Measurements	45
2.4	Discussion	46
2.4.1	Elevated Sample Temperature Composition Comparison	46
2.4.2	Microwave Specific Effects	52
2.5	Conclusions	56
III. Microwave Effects on Sulfur Poisoned Catalysts		60
3.1	Introduction	60
3.2	Experimental	62
3.2.1	Catalyst Preparation	62
3.2.2	Flow Reactor Description	62
3.2.3	Reaction Conditions	62
3.2.4	Reactor Startup and Shutdown	63
3.2.5	Analysis of Reforming Behavior	64
3.2.6	Catalyst Characterization	65
3.3	Results	66
3.4	Discussion	69
3.4.1	Furnace Temperature Comparison	69
3.5	Conclusions	76
IV. Determination of Temperature Within an Active Reforming Catalyst Subject to Microwave Radiation		79
4.1	Introduction	79
4.2	Materials and Methods	81
4.3	Discussion	83
4.3.1	Thermocouples	83
4.3.2	Infrared Emission	84
4.3.3	Overall Equilibrium Composition	84
4.3.4	Elevated Sample Temperature Composition Comparison	85
4.3.5	Temperature Programmed Oxidation of Carbon	88
4.3.6	Water-Gas Shift Equilibrium	95
4.3.7	Water-Gas Shift Equilibrium Under Reforming Conditions	96
4.3.8	System Modeling and Model-Data Comparison	98

4.4 Summary and Limitations	110
V. Conclusions	115
APPENDICES	119
BIBLIOGRAPHY	144

LIST OF FIGURES

Figure

1.1	U.S. liquid fuels supply, 1970 - 2035 (million barrels per day), Reproduced from U.S. Energy Information Administration [1].	3
1.2	Flexible process for the production of chemicals and power using a mixed feed of liquid, gaseous and solid feeds with a common synthesis gas (syngas) intermediate.	6
2.1	Magnetically coupled twin cavity TE mode microwave cavity design. (A) External view and internal field distribution. Sizing of the cavity and iris are dependent upon loading characteristics which dictate the waveguide wavelength. (B) Completed cavity made of aluminum with magnetron removed from left side of waveguide. (C) Completed system installed using a consumer microwave power supply.	21
2.2	(A) Overall gas flow diagram for hybrid microwave-thermal reactor including gas and liquid feeds, 4-way valve, heated lines and furnace. (B) Diagram of microwave system with water cooling and instrumentation.	26
2.3	(A) Overview of the reactor system situated within a walk in hood. (B) Closeup view of the Microwave applicator.	27
2.4	(A) Catalysts with varying levels of coke deposition from propane partial oxidation (GHSV = 30,000, O/C = 1.0 Furnace = 500°C). (A1) fresh cordierite monolith, (A2) fresh reduced catalyst, (A3) 5 minutes POX, (A4) 20 minutes POX, (A5) 60 minutes POX. (B) Absorbed power of a 4 wt% Ni impregnated on Cordierite sample pre and post partial oxidation (5 minutes Propane/Air GHSV = 30,000, O/C = 1.0). (C) Absorbed microwave power as a function of impregnated Ni loading on Cordierite monoliths.	29

2.5	Hydrogen mole fractions (A) and adiabatic reactor temperatures (B) as a function of the atomic oxygen to carbon and water to carbon ratios at a feed temperature of 250 °C as calculated by ASPEN. Species considered in the Gibbs free energy minimization include: H ₂ , H ₂ O, O ₂ , N ₂ , CH ₄ , C ₂ H ₂ , C ₂ H ₄ , C ₂ H ₆ , C ₃ H ₆ , C ₃ H ₈ , CO and CO ₂ .	31
2.6	Coking behavior of Ni/CZO/Cordierite catalyst under POX conditions. Mean values with standard deviations, exponential trend line.	32
2.7	XRD patterns of Ce _{0.75} Zr _{0.25} O ₂ , blank cordierite, 10 wt.% Ni on Ce _{0.75} Zr _{0.25} O ₂ and cordierite loaded with 20 wt.% of washcoat [10 wt.% Ni on Ce _{0.75} Zr _{0.25} O ₂].	36
2.8	POX Results: (A) Conversions, (B-C) Yields and (D) Power absorbed by the catalyst as a function of the applied forward power.	38
2.9	ATR Results: (A) Conversions, (B-C) Yields and (D) Power absorbed by the catalyst as a function of the applied forward power.	40
2.10	Temperature Programmed Oxidation of carbon deposits on catalyst samples after POX (A) and ATR (B) reaction conditions.	41
2.11	Carbon present on catalyst samples after reforming as a function of the applied microwave power.	42
2.12	TPR derivative weight loss curves for POX catalysts post reaction (A) and post TPO (C) and ATR catalysts post reaction (B) and post TPO (D).	44
2.13	Comparison of selected yields and conversions between samples run under microwave conditions and those run under elevated temperatures within a furnace for ATR (A) and POX (B) conditions.	49
2.14	Effective component temperatures and average values with 95% confidence intervals for POX (A) and ATR (B) conditions.	50
2.15	Comparison of coking under microwave and furnace heating environments as a function of the estimated and measured effluent temperature for POX (A) and ATR (B) conditions.	51
2.16	SEM micrographs of samples having undergone ATR reaction exposed to 0 W (A) and 900 W (B) of microwave irradiation.	52

2.17	Incidences where yields obtained under microwave irradiation do not match those obtained by elevating the sample temperature within a furnace for CO (A) and C ₂ H ₂ (B) under POX conditions and CO ₂ (C) and C ₃ H ₆ (D) under ATR conditions. Microwave data is plotted against temperatures determined in yield comparisons.	54
2.18	Comparison of rates of product formation and fuel consumption obtained under conditions of maximum furnace temperature before pre-combustion [550 °C (Furnace)] and maximum microwave irradiation before onset of plasma formation [900 W (MW)]. Also shown is the base case non irradiated samples run within the microwave waveguide (0W) for POX (A) and ATR (B) systems.	57
3.1	Syngas yield versus time for sulfur free and sulfur containing experiments exposed to 200 ppmw atomic sulfur in the form of thiophene while exposed to the specified intensities of microwave irradiation.	67
3.2	ATR w/S Results: Conversion & Yields (A-C), Power absorbed by the catalyst as a function of the applied forward power (D). Circled data points are sulfur free, all others are with sulfur present.	68
3.3	(A) Comparison of yields obtained by traditional furnace heating as a function of the catalyst exit temperature used to find effective temperatures for H ₂ and CO ₂ . (B) Effective component temperature and average value with 95% confidence intervals.	71
3.4	Comparison of trends in effluent concentrations within the elevated temperature environment of a furnace and irradiated samples within the microwave waveguide. Data is plotted as a function of the measured effluent temperature for furnace data and the average effective temperature for microwave data. Displayed are (A) C ₃ H ₈ conversion, (B) C ₃ H ₆ yield, (C) C ₂ H ₄ yield, (D) CH ₄ yield.	73
3.5	Bisected catalysts post reduction in H ₂ at 600 °C.	74
3.6	Carbon present on catalysts post 60 minutes of reaction as a function of the measured effluent temperature for furnace data and the average effective temperature for microwave data points.	75
3.7	Comparison of rates of product formation and fuel consumption obtained under conditions of maximum furnace temperature, 550 °C (Furnace) before pre-combustion and maximum microwave irradiation, 600 W (Microwave) before onset of plasma formation along with base case non irradiated samples (0W).	76

4.1	IR measured temperatures and standard deviations of measured values under POX (A) and ATR (B) conditions.	85
4.2	Thermodynamic equilibrium calculations for a mixture of H ₂ , H ₂ O, O ₂ , N ₂ , CH ₄ , C ₂ H ₂ , C ₂ H ₄ , C ₂ H ₆ , C ₃ H ₆ , C ₃ H ₈ , CO and CO ₂ . Mole fractions for feed conditions of: (A) ATR, (B) ATR dry effluent, (C) POX, (D) Calculated effluent flow rates.	86
4.3	Comparison of selected yields and conversions between samples run under microwave conditions and those run under elevated temperatures within a furnace for ATR (A) and POX (B) conditions. . . .	89
4.4	POX (A) and ATR (B) temperatures obtained from furnace data comparisons.	90
4.5	Temperature Programmed Oxidation of carbon deposits on catalyst samples after POX (A) and ATR (R) reaction conditions.	91
4.6	TPO peaks of samples run within the microwave waveguide and furnace at specified temperatures under POX (A) and ATR (B) conditions. 93	93
4.7	Heat treated carbon. Excess heat treatment temperature experienced by sample as a function of the observed TPO peak shift. 95% confidence intervals provided in green.	94
4.8	Water-Gas Shift data for a catalyst containing equilibrium data (ASPEN Model), characteristic curve of the catalyst (Furnace Data), K _{WGS} plotted vs. IR Temperature (Microwave Data), and actual sample temperature while irradiated (Effective Temperature). . . .	97
4.9	Water-Gas shift comparison of thermodynamically predicted system temperature based off of the WGS equilibrium (T _{WGS,eq}) as a function of the measured exit temperature within the furnace (T _{Furnace}) (A). Observed change in temperature of operation for irradiated samples under POX (B) and ATR (C) conditions as a function of MW power with 95% confidence intervals.	99
4.10	Diagrams of Reaction system: (A) Catalyst within reaction tube with annular pre-heat gas flow and insulation contained in waveguide. (B) Layering of model to capture heat transfer dynamics. (C) System layout for modeling	101
4.11	Composite ϵ'' using volume average of pure component Cordierite, CZO and Ni nano-particles. Cordierite and CZO ϵ'' values approximated from electrical conductivity data.	105

4.12	Model of catalytic system under steady state operation with catalyst temperature superimposed within dashed box. Image is a vertical slice with gas entering from the top. Exit gas temperature at a thermocouple position is 658 °C, consistent with experimental results. . .	107
4.13	(A) Increase in sample temperature over base case conditions at specified points. (B) Power dissipation within catalyst. (C) Profiles of catalyst temperature increase under specified EM field strength. . . .	109
4.14	Comparison of model and experimental power absorption data. (A) Power absorbed by the experimental system used to obtain values of electric field strength. (B) Estimated parasitic load based on absorbed power as a fraction of LHV. (C) Model estimated catalyst exit temperature increase under irradiation.	111
4.15	Summary of methods for determining temperature change within in irradiated catalyst system under POX (A) and ATR (B) conditions.	114
A.1	(Top) Conversion curves for high and low washcoat loadings of the two representative catalysts used. (Bottom) TOF data for the respective catalysts. GHSV of 1,500,000 ($\text{cm}^3_{\text{gas}} \text{cm}^{-3}_{\text{catalyst}} \text{hr}^{-1}$), 500 ppm CO, 257 ppm O ₂	129
A.2	Slope of the conversion vs. temperature curve for samples over a defined range of $X = 0.45 - 0.55$. GHSV of 1,500,000 ($\text{cm}^3_{\text{gas}} \text{cm}^{-3}_{\text{catalyst}} \text{hr}^{-1}$), CO concentration of 500 ppm and O ₂ concentration of 257 ppm.	132
A.3	Conversion curves for samples with similar catalyst loadings and differing washcoat thicknesses at 1,500,000 ($\text{cm}^3_{\text{gas}} \text{cm}^{-3}_{\text{catalyst}} \text{hr}^{-1}$), 500 ppm CO and 257 ppm O ₂ . Thick and thin washcoat loadings are 45 ± 5 wt.% and 8.8 ± 0.5 wt.% respectively.	134
A.4	Sample conversion curves for a first-order system demonstrating the effects of various mass transfer limitations on conversion curves: generated by Paul Laing.	135
B.1	Patent Application: Use of Microwave Energy to Remove Contaminating Deposits from a Catalyst US 2011/0118105 A1.	138
C.1	Electron Ionization Mass Spectra data from the NIST Chemistry Database. Primary peak for each species is scaled to 1,000 a.u. . . .	141

LIST OF TABLES

Table

2.1	Operating conditions for POX and ATR experiments.	30
2.2	Raman carbon analysis: Peak area ratios and standard deviation on measured values.	43
2.3	Chemisorption Results: Dispersion, Metallic surface area and Crystallite size for selected conditions.	45
2.4	Catalyst exit temperatures recorded under each operating condition. Uncertainty on values is $\pm 12 - 21$ °C.	48
3.1	Autothermal reforming with sulfur operating conditions.	63
4.1	Operating Conditions for POX and ATR experiments.	82
4.2	Catalyst exit temperatures recorded under each operating condition. Uncertainty on values is $\pm 12 - 21$ °C.	88
4.3	TPO position of maximum peak feature for samples reacted without irradiation in the waveguide and furnace.	92
4.4	Tabular summary of the model water-gas shift analysis presented in Figure 4.8.	96
4.5	Microwave reactor model parameters.	106
4.6	Temperature shift experienced by irradiated catalysts as measured by specified methods (Type of error reported). POX Conditions: 0 W $T_{exit} = 550 \pm 15$ °C ATR Conditions: 0 W $T_{exit} = 573 \pm 21$ °C.	112
A.1	Reaction flow conditions at 1,500,000 GHSV over selected Pd/Al ₂ O ₃ catalysts.	127

A.2	Surface area and dispersion results for Pd/Al ₂ O ₃ catalysts.	128
A.3	Activation energy for the oxidation of CO over Pd.	130
A.4	TOF values for the oxidation of CO over Pd systems.	131
A.5	Weisz-Prater parameter at 540 K. Systems are considered to be free of diffusion limitations when $\Phi \ll 1$	132
A.6	Catalysts used for aligning conversion curves over different washcoat thicknesses: 0.7 wt.% Pd TH100/150 catalyst material.	133
C.1	Relative Ionization Intensities obtained for this study.	140
D.1	Propagation of error: Contribution of error from reactor system components.	143

LIST OF APPENDICES

Appendix

A.	CO Oxidation on Pd/Al ₂ O ₃ : Kinetics in the Absence of Heat and Mass Transfer Effects	120
B.	Technology Disclosures and Patents	137
C.	Mass Spectrometer Calibration	139
D.	Experimental Error Analysis	142

LIST OF ABBREVIATIONS

ATR	Autothermal Reforming
CZO	$\text{Ce}_{0.75}\text{Zr}_{0.25}\text{O}_2$
DI	Deionized
EM	Electromagnetic
F_x	molar flow of component x
GC	Gas Chromatograph
GHSV	Gas Hourly Space Velocity
$\text{H}_2\text{O}/\text{C}$	steam to atomic carbon ratio
MS	Mass Spectrometer
MW	Microwave
NO_x	oxides of nitrogen (NO, NO_2)
O/C	atomic oxygen to atomic carbon ratio
POX	Partial-Oxidation
RF	Radio Frequency
sccm	Standard Cubic Centimeters per Minute
SEM	Scanning Electron Microscopy
SR	Steam Reforming
TGA	Thermogravimetric Analysis
TPO	Temperature Programmed Oxidation
TPR	Temperature Programmed Reduction

WGS Water-Gas Shift

W Watts

XRD X-Ray Diffraction

Y_{sg} synthesis gas yield

ABSTRACT

Microwave-Catalyst Interactions in the Reforming of Hydrocarbons

by

Steven E. Edmund

Chair: Johannes W. Schwank

Portable reforming technology for the production of synthesis gas (CO & H₂) from hydrocarbons has the potential to be used in distributed chemical manufacturing, emissions control and engine cold-start technology, as well as in portable power generation in conjunction with fuel-cells. Catalytic reforming of hydrocarbon fuels is frequently plagued by deactivation *via* carbon deposition and sulfur poisoning. Performance further degrades when catalysts are supplied with non-ideal feed gas compositions.

The present study examines a method of dealing with hypothetical feed disturbance events and resulting deactivation by irradiation of the catalyst in the microwave band (2.45 GHz). A high temperature microwave reactor was constructed to probe interactions of electromagnetic radiation with catalysts consisting of cordierite monoliths washcoated with Ni on a Ce-Zr mixed oxide. Reaction conditions were selected to promote carbon deposition with low O/C and H₂O/C ratios using propane and ethylene as the fuel. Irradiation of active reforming catalysts was found to alter product distributions and carbon deposition.

Experiments were conducted to probe the effects of microwave irradiation on product distributions and carbon deposition while operating under regimes of partial-oxidation and autothermal reforming with and without sulfur present in the form of thiophene. Comparisons were drawn between irradiated samples and samples exposed to elevated temperatures within a furnace to extract microwave specific heating effects. The microwave-heating environment was found to exhibit unique effects dependent upon the feed composition. Operation under highly oxygen deficient partial-oxidation conditions produced similar changes in products and carbon deposition under microwave and conventional thermal heating. Addition of water in autothermal reforming with and without sulfur present resulted in significant departures from conventional thermal behavior with reduced coking and improved synthesis gas yields when irradiated. Volumetric microwave heating was found to reduce the prevalence of cracking and dehydrogenation products in sulfur poisoned experiments while supplying energy to the typically heat-transfer-limited downstream endothermic steam-reforming region of the catalyst.

Finally, several methods for estimating the temperature rise experienced by an irradiated reforming catalyst are presented to gain further insight into the conditions experienced when reforming hydrocarbons within an electromagnetic field. Under certain conditions the catalyst temperature is estimated to increase by over 200 °C.

For the first time, data is presented on the interaction of microwaves with hydrocarbon reforming catalysts operating under deleterious conditions, and the results are compared with traditional thermal heating to determine those effects attributable to microwave specific heating effects. Microwaves were found to couple strongly to carbon, resulting in selective oxidation of carbon deposits when sufficient oxygen is available. Similarly, product distributions were found to change based on enhanced steam-reforming and water-gas shift activity resulting from volumetric heating of the catalyst and reduced entrance region temperatures.

CHAPTER I

Introduction to Catalytic Fuel Reforming and Microwaves

1.1 Current Energy Challenges

Concerns over energy security and energy supply are highly influential on politics, economics, and technology development within the United States and beyond. There has been a continual drive to decrease the use of fossil fuels, driven largely by economics but also with the looming specter of a growing consensus on the effects of anthropogenic emissions on climatic systems. In 2010 the United States imported 49% of the crude oil consumed in the production of distillate products such as gasoline and diesel used primarily for the transportation and portable power markets [1]. For the foreseeable future, the U.S. is expected to continue importing large quantities of petroleum as shown in Figure 1.1 Purchase of oil from the international market results in a daily export of \$722 million U.S. dollars per day. Additional costs of securing global supply routes and maintaining stability throughout the world poses a further burden on the economy. The global power of petroleum is apparent in the number of petro-dictators, authoritarian regimes, and corrupt governments that are supported through oil revenue [2].

In the near-future it appears that petroleum will continue to provide the vast

majority of energy for transportation systems. Despite this, there is a continuing emphasis on technologies that will assist in making the long-term transition to sources of energy that can reduce geo-political instability and result in an improved business climate with certainty in energy prices and regulatory environments. While it is unlikely that changes to the global climatic system will be entirely avoided, it is possible that through changes in our energy systems we may avoid the worst case scenarios.

Numerous routes to reduce dependence on imported oil have been proposed over the years including increased use of ethanol and other biofuels, electric-propulsion, and the transition to a “Hydrogen Economy”. It is the very scale of our transportation energy use that limits the entry of new technologies, as the momentum of over a century of petroleum domination continues to carry the global economy forward. Within the United States, the transportation sector used 27.63 quadrillion BTU’s in 2010, the equivalent amount of energy consumed by 15.4 billion 60 Watt light-bulbs over that year, 50 for each individual in the United States. While there are opportunities for biofuels to displace part of this demand, it is clear that a simple switch to biofuels is not possible. Similarly, with the majority of our electricity from fossil fuel sources, there are debatable environmental benefits from using all-electric vehicles, though a greater case can be made based on energy independence using coal and natural gas resources to displace imported oil. While it has been well established that there is significant off peak capacity in the U.S. that could be utilized for vehicle charging, a complete conversion of our transportation system would require substantial changes to the electricity grid to handle the capacity and address concerns over global warming. There are also modes of transportation such as heavy trucking, trains and airplanes where the high energy density of liquid fuels make them difficult to replace with electricity (though Europe has been successful at creating vast electric train corridors).

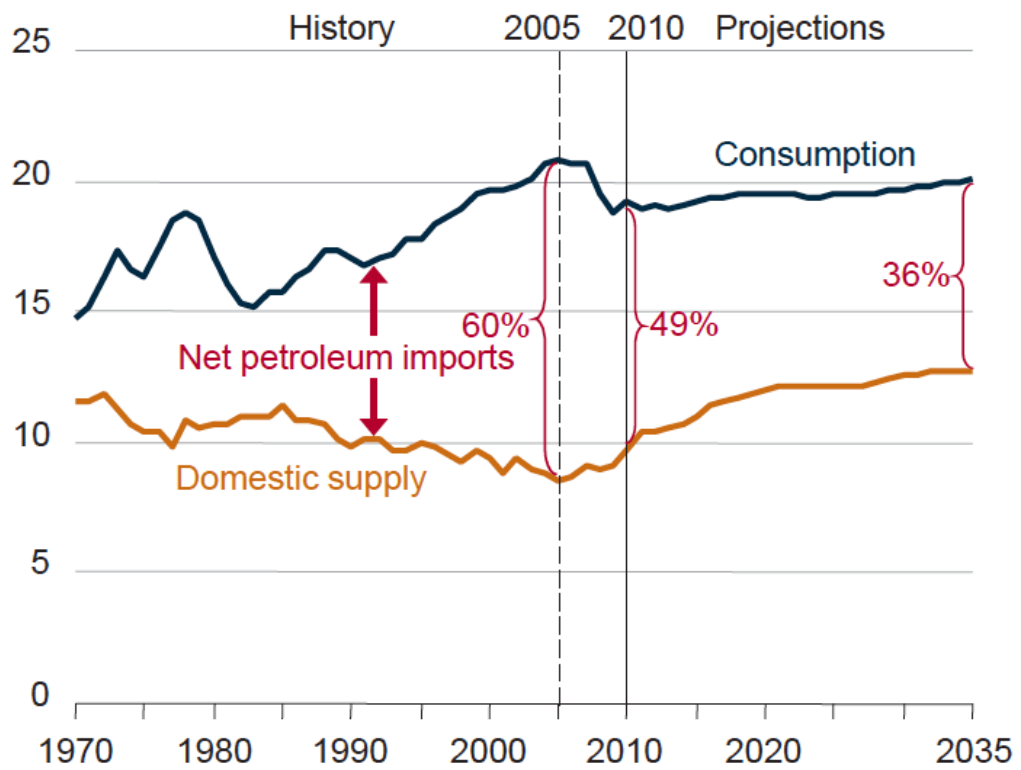


Figure 1.1: U.S. liquid fuels supply, 1970 - 2035 (million barrels per day), Reproduced from U.S. Energy Information Administration [1].

Transitioning to a Hydrogen Economy has been touted as a means to bring about energy independence, however much has been misunderstood by policymakers, the media and the general public about hydrogens place as an energy carrier and not an energy source. This misunderstanding, combined with a lack of long-term energy policy has led to a reduced interest in the use of hydrogen as a future energy carrier. Although research toward a hydrogen economy has decreased, much progress in electrochemical energy conversion technology has been made. Significant research has gone into fuel cell systems, with the goal of converting chemical energy into electrical energy at higher efficiencies than can be obtained through traditional means of combustion engines and turbines. Fuel cells have continued to mature as a technology, and while a hydrogen infrastructure never materialized due to a myriad of challenges including the challenge of storing compressed hydrogen, they still may play a part in transitioning off of fossil fuels.

Part of the long-term transition away from oil involves reducing overall demand and allowing flexibility in the use of resources. Interoperability of feedstocks, processes and products could allow producers to more easily use the feedstock that is the least expensive at the time or produce the product with the most value. Figure 1.2 is one example of using catalytic technology to create a flexible system with a common synthesis gas intermediate. Synthesis gas, also referred to as syngas, is a mixture of CO and H₂ that can be used as the building blocks for numerous chemical synthesis routes as well as for power generation using fuel cells [3]. Systems have been proposed combining biomass gasification/reforming and solid oxide fuel cells (SOFC) with predicted thermal efficiencies of over 58% [4, 5]. Combining a reformer and SOFC for electricity generation in an electric vehicle would constitute a truly fuel flexible system, capable of using regionally available fuels as well as H₂ generated by renewable sources [6]. Small scale systems may be developed for flexible-feedstock chemical or electricity production. Units for these purposes will need to be robust

and able to operate under conditions outside of those experienced by current large scale steam reforming facilities. This work focuses on the reformer component, and a novel means of altering its operation under less-than-ideal operating conditions with the goal of producing a more robust system for portable applications.

1.2 Literature Review

1.2.1 Introduction to Catalytic Hydrocarbon Reforming

Chemical transformations are governed by the laws of thermodynamics, establishing bounds on conversion that constitute equilibrium within a system. Thermodynamics alone however does not describe the world as we see it; the rate at which equilibrium is established also plays a significant role. Many reactions exhibit kinetics that are too slow to be practical at reasonable conditions, or produce undesirable intermediate byproducts. It is the goal of catalysis to lower the energy barriers for reactions, allowing them to be carried out at reasonable temperatures under controlled conditions to obtain products that would not otherwise be available. Catalysts are ubiquitous in the processing of fossil fuels and subsequent transformation into higher value products such as plastics and paints.

Fuels such as diesel can be converted into syngas by catalytic reforming processes. Presently syngas is produced by large-scale steam reforming plants operating mostly on natural gas. To scale the production of syngas down and reduce the external heat transfer load requires transitioning to an autothermal operating regime. Reaction (1.1) is a simplification of the overall reactions occurring during reforming in which the exothermic partial oxidation (POX) of a fuel, Reaction (1.2), is used to drive endothermic steam reforming (SR), Reaction (1.3), for additional production of H_2 . The term autothermal reforming (ATR) is applied as the feed stoichiometry may be balanced to generate a thermally neutral process, simplifying system design and

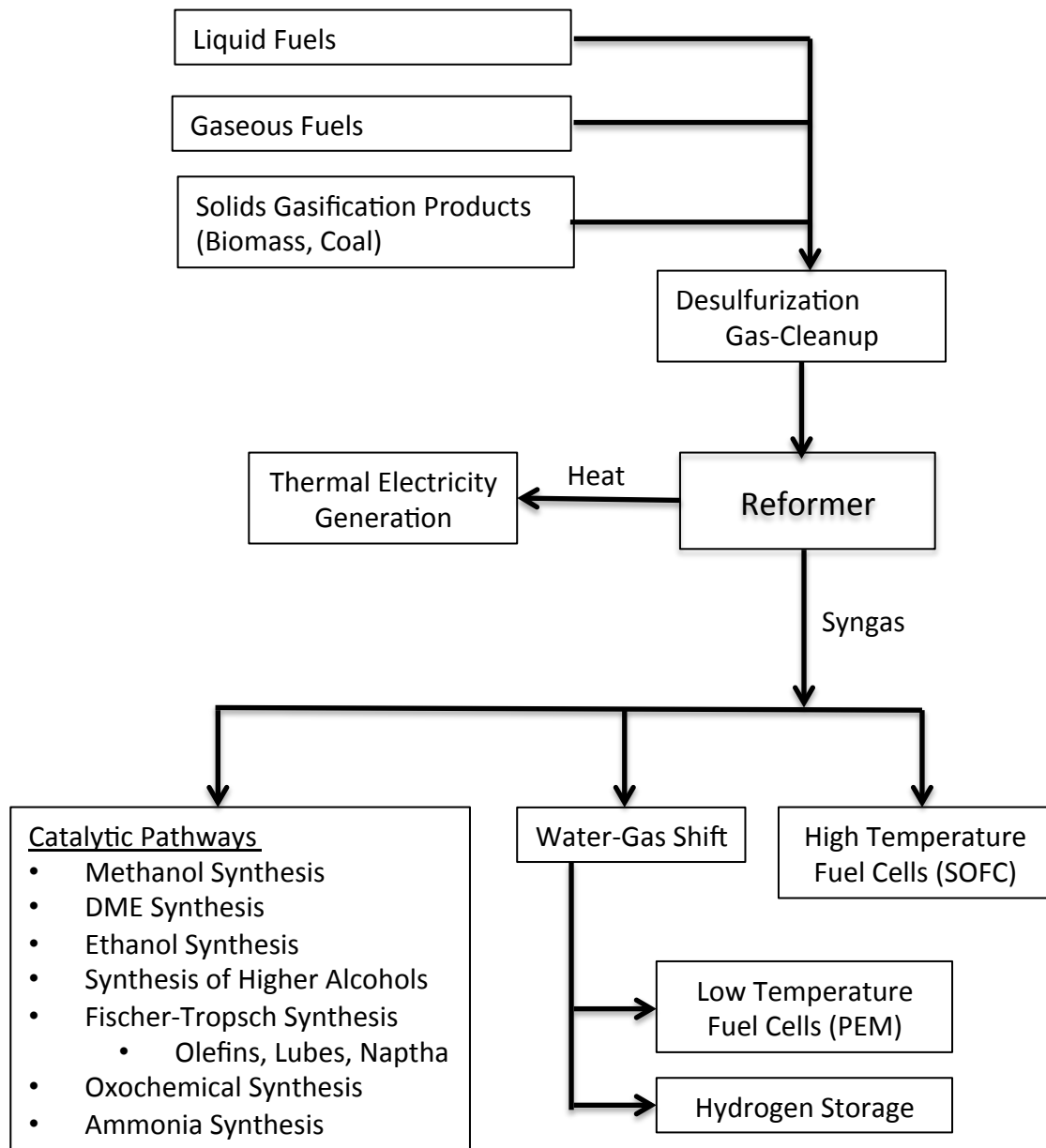
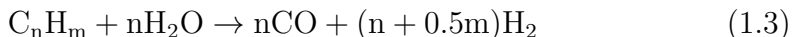
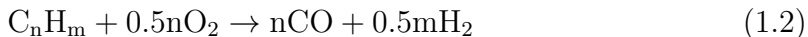


Figure 1.2: Flexible process for the production of chemicals and power using a mixed feed of liquid, gaseous and solid feeds with a common synthesis gas (syngas) intermediate.

eliminating the need to carry water in portable applications. The water-gas-shift Reaction (1.4), is generally considered to be in equilibrium at reaction temperatures [7].



The majority of the heterogeneous and homogeneous oxidation of hydrocarbons occurs within the entrance region of the catalyst leading to high temperatures along the front face of the catalyst. When stoichiometrically limited in O_2 , a significant amount of H_2 , CO and H_2O are generated along with CH_4 and other cracking and dehydrogenation products [8, 9]. Thermal cracking can be quite problematic industrially as non-uniform coke deposition hinders heat transfer, requiring the shutdown of units to regenerate [10]. Oxydehydrogenation of propane has been shown to produce C_3H_6 , with yields decreasing as more O_2 is introduced, leading to greater CO_2 production [9]. Little carbon is deposited within the entrance region as the presence of O_2 and high temperatures lead to oxidation of any deposits. As the concentration of O_2 decreases, thermal cracking occurs within the entrance region where temperatures above $700\text{ }^\circ\text{C}$ favor the endothermic cracking reactions [11]. Thermal cracking of C_3H_8 has been shown to produce CH_4 , C_2H_4 and C_2H_6 with small amounts of C_3H_6 decreasing with temperature [11, 12, 13]. Past the entrance region, when all O_2 has been consumed, the steam reforming (1.3) and water-gas shift reactions (1.4) are dominant. This region of the catalyst is generally much cooler than the entrance region due to the endothermic energy demand of steam reforming. Spatially resolved partial oxidation experiments using CH_4 and C_2H_6 show the reaction of H_2O pro-

duced in the entrance region with CO to produce additional H₂ via the water-gas shift reaction [8, 14]. The down-stream region of the catalyst is prone to carbon deposition, particularly at the low H₂O/C ratios used in this study [15]. Cracking products produced within the high temperatures of the entrance region are significant coke precursors.

Reforming of hydrocarbons is plagued by several methods of catalyst deactivation, most notably carbon and coke deposition and the poisoning of active sites by sulfur [16, 17, 18, 19, 20, 21]. It is well known that sulfur in a variety of forms will poison many commercially available reforming catalysts at concentrations in the parts per-million (ppm) range [16, 22, 18]. Since current petroleum supplies are increasingly sulfur rich, sulfur tolerance is a necessity for future hydrocarbon processing. Numerous studies have examined the effect of steam and oxygen concentrations on the hydrocarbon reforming products of noble and non-noble metal catalysts. Broad differences have been identified in the activity of different catalyst systems, however, common to all is the propensity toward carbon deposition and sulfur poisoning under non-ideal reaction conditions [16]. Industrial steam reforming operations closely manage carbon deposition and catalyst deactivation through such practices as introduction of oxygen in the feed, product recycle, high steam-to-carbon ratios, and careful thermal management among others [23]. Within portable applications such deactivation counter-measures may not be feasible.

Carbon deposition is a common cause of deactivation in a variety of hydrocarbon processing reactions (Cracking, Reforming, Dehydrogenation, Fisher-Tropsch). Carbon and coke deposition (i.e. coking) are significant issues in reforming reactions when insufficient oxygen in the form of O₂ or H₂O is available for the oxidation of carbon to CO. Coke deposition results from the cyclization and polymerization of cracked and partially dehydrogenated hydrocarbons resulting in their condensation as an encapsulating coke [23]. Carbon could be considered as fully dehydrogenated

coke, however it forms via alternate mechanisms. Helveg et al. show the formation of carbon nanofibers to be the result of changing nickel morphology and carbon diffusion across the surface, with nickel step sites being particularly active [24]. Many morphologies of carbon are observed on autothermal reforming catalysts including carbon nanotubes, fibers, and sheets, any of which may have embedded metal particles [25]. The overall effect of coking is to decrease the effectiveness of the catalyst through encapsulation, coating, or by lifting the catalyst particle off of the surface resulting in loss of the catalyst from the reactor. Coking results in diffusion limitations and if left unaddressed can fully clog a reactor or cause the disintegration of supports due to mechanical stresses from the growing carbon filaments [21].

Coking and sulfur poisoning may both be addressed on-stream through altering the reactor temperature and gas composition [26, 27]. To remove carbonaceous deposits, the reactor is fed O_2 to oxidize the carbon. Similarly H_2 is supplied to sulfur poisoned samples under high temperatures to reduce sulfur and drive it from the surface. Both techniques may be effective, however coke oxidation is limited by poor heat and mass transfer and the reduction of sulfur requires significant quantities of reductant at high temperatures. Ideally one would like to quickly and selectively heat the catalyst surface to oxidize carbon and to provide an increased thermodynamic driving force for sulfur desorption. A novel regeneration system is also needed for portable applications wherein a reformer must be capable of rapid self-regeneration while maintaining functionality. The issues described herein could all benefit from the ability to volumetrically heat a catalytic system quickly. This work will explore whether microwave radiation will selectively interact with a catalyst to affect the operation of carbon and sulfur poisoned samples.

Microwaves were chosen for exploration based on their specific location within the electromagnetic spectrum. Photocatalysts are a popular area of research as the photon energy of ultraviolet light is on the order of bond energies (3.1+ eV). Unfor-

tunately, the penetration depth of ultraviolet light in most materials is only a few microns, eliminating the possibility for volumetric effects. Microwaves have far less energetic photon energies on the order of 10^{-3} eV, however they are able to provide a volumetric effect not attainable at other frequencies, excluding high frequency ionizing radiation.

The use of microwaves to influence reforming catalysis holds particular promise due to the differing interaction of microwaves with the solid phases present [28, 29]. At reforming temperatures microwaves have no effect on the gas or absorbed species present. Microwaves interact with and dissipate energy within the solids according to their dielectric properties, specifically their dielectric loss factor. The bulk of a catalyst is generally a ceramic support with low dielectric loss, rendering it effectively transparent to the microwave field [30, 31, 32, 33]. The catalytic phase consists of small metallic particles that have a much higher dielectric loss and therefore absorb microwave energy very strongly [34, 35, 36, 37]. Many forms of carbon deposited during reaction are conductive and are strong absorbers of microwave frequency energy, with a high dielectric loss factor [38, 39, 40]. Microwaves are able to influence the system by introducing energy at the catalytic sites and within the growing carbon structures in order to effect chemical transformations.

Within the body of this work, nickel (Ni) is used as a model reforming catalyst to study the effects of microwave band irradiation on the reforming of C_3H_8 and C_2H_4 under conditions of low O_2 and H_2O that favor carbon deposition and reduced syngas yield. Much research has focused on the use of precious metal (Pt, Ru, Rh) catalysts due to their often superior catalytic properties, however those metals are over three orders of magnitude more expensive than Ni, and in far shorter supply [21].

Previous work has investigated the catalyst-free plasma based reforming of hydrocarbons [41, 42, 43, 44, 45, 46, 47, 48]. The present study focuses on coupling the microwave field to the solid phases present, supplying energy to specific structures

within the catalyst and avoiding plasma formation. Primary goals of this research include:

- Furthering the understanding of carbon deposition under harsh reforming conditions
- Examining the effects of microwaves on catalyst morphology and activity
- Exploring the use of microwaves to remove carbon from operating reforming catalysts
- Exploring the interaction of microwaves with a sulfur poisoned system

In the course of this work an emphasis is placed on observed changes in product distributions and carbon deposition under microwave irradiation. Where possible, experiments are conducted to determine those effects that are unique to the microwave heating environment and those that can be attributed to more traditional modes of heating within a furnace. A substantial amount of knowledge was also gained regarding the design and construction of reforming reactors, catalyst washcoating techniques, high temperature kinetic measurements and various means of estimating temperature within electromagnetic fields. In collaboration with Ford Motor Company a project was undertaken to study high temperature CO oxidation kinetics in washcoated monolith catalysts. This work is included in Appendix A, complimenting the work in this thesis by exploring the possibility of obtaining kinetic and washcoat diffusion data in monolith based samples at high space velocities.

1.2.2 Background of Microwave Heating

Microwaves are electromagnetic waves 1 mm to 1 m in length corresponding to frequencies of 30 GHz to 300 MHz. The most common frequency for microwave heating is 2.45 GHz used in household microwave ovens, however many industrial processes

also operate at 915 MHz. When an electromagnetic wave comes into contact with a material the electric field component may be reflected, absorbed or transmitted. Reflective materials tend to be bulk metals with many free electrons, however it has been widely shown that micron and sub-micron metal particles are strong absorbers of microwaves [49, 40, 50]. Microwave transparent materials tend to have low conductivities associated with members of the glass and ceramics family [34]. Microwave absorbing materials consist of all those with properties between an ideal conductor and an ideal insulator.

Microwaves are widely applied in industrial processes where they can result in both improved processing times and reduced power use [34]. Microwaves can be generated at 85 - 94% electrical efficiency and then directed and applied in very specific and efficient ways [51]. Several advantages of microwave processing including rapid heat transfer, volumetric and selective heating, uniformity of heating, fast switching on and off, compact equipment, high power densities, as well as low maintenance and service costs [52, 53, 54, 55]. These advantages are contrasted with the poor heat transfer characteristics of traditional heating techniques amplified by the low thermal conductivity of gases and many catalyst supports. Because of the many advantages of microwave heating, there have been over 4,000 publications looking at the application of microwaves to organic synthesis [56].

An understanding of microwave-material interactions begins with the complex permittivity, also known as the complex dielectric, $\epsilon^* = \epsilon' - j\epsilon''$, in which ϵ' represents the storage of energy in the form of a reactive response or displacement currents and ϵ'' the ability for the material to dissipate energy. Heat generation by microwave irradiation is a result of the material storing energy in the form of heat, ϵ'' is thus frequently called the dielectric loss factor. A more complete picture regarding the heating characteristics of any material is obtained from the ratio of these two param-

eters termed the loss tangent.

$$\tan \delta = \frac{\epsilon''}{\epsilon'} \quad (1.5)$$

Dielectric loss is a function of frequency, temperature, chemical composition, size and geometry as well as adsorbed surface species. Obtaining the average electric field strength, E_{rms} within a microwave cavity from Maxwell's equations, the power dissipated in a model material may then be obtained by Equation (1.6) where f is the operating frequency [34]. Further information on solutions to the Maxwell equations for microwave applications may be found elsewhere [29, 52, 57]. If the material of interest is a strong conductor, Equation (1.6) may be approximated by Equation (1.7), where σ is the electrical conductivity.

$$P_E = 2\pi f \epsilon_0 \epsilon'' E_{rms}^2 \quad (1.6)$$

$$P_E = \sigma E_{rms}^2 \quad (1.7)$$

Microwave heating occurs due to two primary physical phenomena, dipolar re-orientation and conductive heating. Heating of liquids generally results from the polarization and phase lag between dipolar molecules (e.g. water) and the applied electrical field. Conversely, in highly constrained polymer or solid systems, where molecules are not free to rotate, dipolar heating is generally not of consequence. Ionic solids heat due to the motion of electrons moving with the electric field. Materials with many free electrons heat well, as do many ceramics at high temperatures, leading to thermal runaway in some systems [57]. When heating nm sized metal particles there is also the issue of quantum mechanical effects altering thermal and electrical properties from the bulk phase values.

In addition to the above mentioned microwave heating phenomena, there are many other processes occurring. The complex permeability may be significant when dealing

with magnetic metals such as Ni. Maxwell-Wagner interfacial heating, possible surface plasma formation and penetration depth effects resulting in attenuation of the electric field must all be considered in a thorough analysis of microwave effects. Additional information on these phenomena may be found elsewhere [52, 59, 51, 34, 60].

1.2.3 Microwave-Material Interactions

While bulk metals reflect most microwave energy, it has been known for some time that metal powders heat well under microwave irradiation [61, 37, 49]. Heating rates of Ni powders have been reported in excess of $3,000\text{ }^{\circ}\text{C s}^{-1}$, leading to their use in sintering operations [49, 28, 50]. Viau et al. show that 60 - 250 nm Ni particles interact with the magnetic component of an electromagnetic wave significantly at 2.45 GHz with only a weak dependence on particle size [35, 36]. Small metallic particles have been shown to interact more strongly with the applied electromagnetic field at higher frequencies, however the relative transparency of other materials also decreases with increasing frequency [62]. As a result, a frequency of 2.45 GHz was chosen for study based on the availability of inexpensive and efficient generation and transmission equipment necessary in any future industrial implementation of the technology.

Carbon has long been known to be strong absorber of microwave radiation and is used on the exterior of stealth planes to reduce their radar signature. A composite of Ni and carbon has even been proposed as a microwave absorbing material [38]. When working to purify carbon nanotubes of Ni-Y catalyst impurities, Harutyunyan et al. observed that under high microwave power levels most of the carbon was oxidized [40]. When the power was reduced, they were able to heat the nm catalyst particles so that carbon adjacent to the surface was oxidized with the carbon nanotubes remaining intact. Temperature programmed oxidation peaks show a shift to higher temperatures after microwave treatment, consistent with the carbon adjacent to the surface being removed. Research into the regeneration of diesel soot traps by microwave irradiation

shows that the removal of carbon by microwaves takes less time than with conventional heating methods [63, 39, 64]. Furthermore, the addition of Fe/V/K and Cu/V/K catalysts to the soot traps resulted in improved heating and lower energy requirements compared with their un-catalyzed results [65]. Further work has examined the design of microwave susceptible oxidation catalysts for diesel soot control finding reduced deactivation under microwave irradiation when compared with conventional heating [66]. Microwave frequency dielectric measurements have been used to measure carbon content on diesel soot filters and it is suspected that this work may lead to similar capabilities of measuring carbon present on reforming catalysts [67, 68].

In a microwave regenerated reforming system the desorption of sulfur is highly desirable to maintain catalyst activity in sulfur laden fuels. Ibe et al. examined the effects of microwave radiation on sulfur adsorbed to a Pt-Ba NO_x storage reduction catalyst [26]. Under microwave irradiation, desorption of sulfur was found to occur at temperatures below 200 °C while it is reported that desorption normally occurs at temperatures above 600 °C. Such a drastic difference in temperatures is likely the result of selective heating of sulfur adsorbing sites and inaccurate temperature measurement in an unevenly heated sample. Similarly Zhang et al. observed increased conversions in the catalytic reforming of methane with carbon dioxide over Pt, consistent with the formation of hot-spots on the catalyst and the inconsistencies of temperature measurement [69]. Difficulty in measuring temperature and the resulting improper reporting of results is common in literature. Thermodynamics will dictate the lightoff temperature of a reaction on a surface, therefore when studies report lightoff at reduced temperatures under microwave irradiation it is indicative of local hotspots within the sample [70, 71, 66]. These hotspots have been shown to be less prone to poisoning by SO₂ on La_{0.8}Ce_{0.2}MnO₃ perovskite, methane oxidation systems [72].

Apart from bulk heating properties, adsorbed species also exhibit heating char-

acteristics proportional to their liquid phase permittivity [73]. In multi-component systems, differences in dielectric loss of adsorbed species can alter adsorption equilibria and can be used to preferentially adsorb/desorb selected components [74, 70]. Microwave removal of sulfur may be enhanced by the modification of surface groups or by the addition of secondary components among other variables including particle size, gas phase composition and microwave field intensity [75]. Absorption of microwave energy by adsorbed species and any resulting changes in adsorption equilibrium would be most visible at lower temperatures than are generally observed in this study.

It is expected that microwave heating will have a similar effect on dispersion as observed in conventional sintering processes [76]. Several studies have alleged improved catalyst performance after microwave calcination [77, 78, 79]. Some papers have reported permanent changes in catalytic behavior, however little explanation has been provided for such effects [80, 81]. Studies showing both greater activity and reduced coking in the isomerization of 2-methylpentane do not offer detailed analysis of why these phenomena occur, but agree that the exposure to microwaves generates a, "different structure and reactivity" with little analysis of the catalyst surface itself [82].

CHAPTER II

Microwave Effects on Carbon Deposition and Product Distributions

2.1 Introduction

Portable reforming technology for the production of synthesis gas (CO & H₂) from hydrocarbons has the potential to be used in conjunction with fuel-cells, distributed chemical manufacturing, emissions control and engine cold-start technology [83, 3, 6, 84]. Presently, syngas is produced by large-scale steam reforming plants operating on natural gas. To scale the production of syngas down and reduce the external heat transfer load requires transitioning to an autothermal operating regime wherein the exothermic partial oxidation of the hydrocarbon (1.2), is paired with the endothermic steam reforming reaction (1.3). Pairing of these two reaction pathways into autothermal reforming (1.1) simplifies system design and eliminates the need to carry water in portable applications.

Carbon deposition in industrial steam reforming is managed by the introduction of small amounts (vol.%) of oxygen in the feed. In a similar manner, the catalyst is kept in a reduced (active) state by either introducing a small amount of H₂ in the feed or recycling some of the product. When considering the use of a reformer within a portable application, it may not be possible to adjust the feed gas composition,

and thus alternate methods of altering the system performance are presented in this work. Photocatalysis has received much attention as photon energies are on the order of bond energies, however a major disadvantage are the geometries required to get a significant flux of photons to the catalytic surface. A reformer operating at high temperature is typically within a tin-can configuration, not conducive to photocatalysis. Microwaves provide an alternate means to volumetrically introduce energy given the proper catalyst design. The major disadvantage of microwaves as compared with photocatalysts are the relatively low photon energies on the order of 0.001 eV, requiring heating effects to play a major role in coupling of microwave irradiation to chemical reactions rather than direct electron exchange mechanisms.

To investigate the high temperature reforming of hydrocarbons in the presence of microwave frequency radiation, a novel high temperature microwave reaction system and corresponding catalysts were developed. Reactor development was based on the design of a flexible system capable of handling liquid and gas feeds with fast switching for reliable startup and shutdown. Operation of a catalyst system under irradiation necessitated the use of a high temperature microwave applicator paired with a furnace to pre-heat the feed. Positioning of the furnace also allowed for operation of the system in the conventional furnace heated mode.

Catalyst formulation was based on the constraints of operating under high temperature irradiating conditions, where extreme coking and high temperature ($T > 700\text{ }^{\circ}\text{C}$) excursions may occur. The support material must have a lower dielectric loss than the catalyst so that the majority of the microwave energy is coupled to the catalytic phase. In order to minimize EM field attenuation across the catalyst as well as to reduce back pressure due to coking, a cordierite monolith support was utilized [85]. Cordierite monoliths are used heavily in automotive and environmental applications where high thermal stability is required [86, 87]. Use of a system similar to those used industrially is insightful as microwave-material interactions can be highly

influenced by the geometries of a sample. For a catalytic phase, nickel (Ni) supported on a mixed ceria-zirconia oxide ($\text{Ce}_{0.75}\text{Zr}_{0.25}\text{O}_2$) was chosen based on previous fuel reforming work with Ni as a catalyst combined with the oxygen storage ability of $\text{Ce}_{0.75}\text{Zr}_{0.25}\text{O}_2$. Past work has examined catalysts consisting of Ni and $\text{Ce}_{0.75}\text{Zr}_{0.25}\text{O}_2$ impregnated on cordierite monoliths [21, 20, 88, 89]. A major drawback with this technique is the presence of nickel within the cordierite pore structures leading to coking and disintegration of the monolith. In the interest of a stable catalytic system in which the initial spatial relationship of nickel with regards to cordierite and CZO is well controlled, washcoating was pursued.

Washcoating is a well-developed industrial practice, however each system is unique, requiring procedural development and testing. A procedure for ball milling of catalysts consisting of Ni impregnated on $\text{Ce}_{0.75}\text{Zr}_{0.25}\text{O}_2$, and subsequent washcoating onto cordierite monoliths was established based on work in similar systems [90, 86, 91]. Within the washcoat slurry, a variety of binders, temporary binders and dispersants were used to alter the adherence of the washcoat to the monolith [90, 92, 76, 91, 93]. Tests were conducted to determine the effect of various additives on washcoat adhesion as measured by weight loss after 1 hr of submersion in a sonicated acetone bath [91]. In order to produce a washcoat with good adhesion properties the Ni/ $\text{Ce}_{0.75}\text{Zr}_{0.25}\text{O}_2$ is milled to 2-10 μm . Particle sizes were examined by zetasizer (Malvern Instruments Zetasizer Nano) and scanning electron micrograph (Philips XL30 ESEM) to determine optimal ballmilling time.

2.2 Experimental

2.2.1 Preliminary Experiments in Microwave Cavity Operation

Preliminary investigations into the use of microwaves to influence catalytic reforming systems involved the use of a consumer grade multi-mode microwave cavity to

carry out carbon removal experiments. A brief attempt was made at the construction of a single mode chamber, however both the multi-mode and single mode cavities were unable to provide the reliability and repeatability desired, nor could they operate in the temperature regime required.

Lack of experimental precedence for the regeneration of catalytic reforming systems by microwave irradiation led to the performance of several proof of concept experiments for the removal of carbonaceous deposits. Samples of coke covered catalysts were exposed to microwaves in the presence of air using a modified consumer microwave oven (Sharp Model #R-202EW, 2.45 GHz) containing a water load to reduce magnetron heating. The catalysts tested consisted of 4 - 16 wt.% Ni impregnated on cordierite monoliths, some samples of which also contained 23 wt.% CZO. Carbon deposition was performed previously by autothermal reforming of dodecane [21]. Heating rates in excess of $100\text{ }^{\circ}\text{C s}^{-1}$ were observed in the microwave, with temperature programmed oxidation revealing 50 wt.% less carbon present after microwave treatment. Using a household microwave oven was moderately effective at the proof of concept stage, however the multi-mode cavity results in an unstable electric field intensity that changes with loading and time [94].

In the interest of generating a consistent and reproducible microwave field for experimentation, a short foray into the construction of a single mode microwave cavity was attempted. A resonant cavity was designed based on the work of Metaxas et al. resulting in the magnetically coupled twin cavity design shown in Figure 2.1 [94]. Although functional, it lacked the ability to tune the cavity and thus impedance mismatches resulted in poor energy transfer to the sample and overheating of the magnetron. Subsequently an industrial microwave system was purchased as described in section 2.2.3.

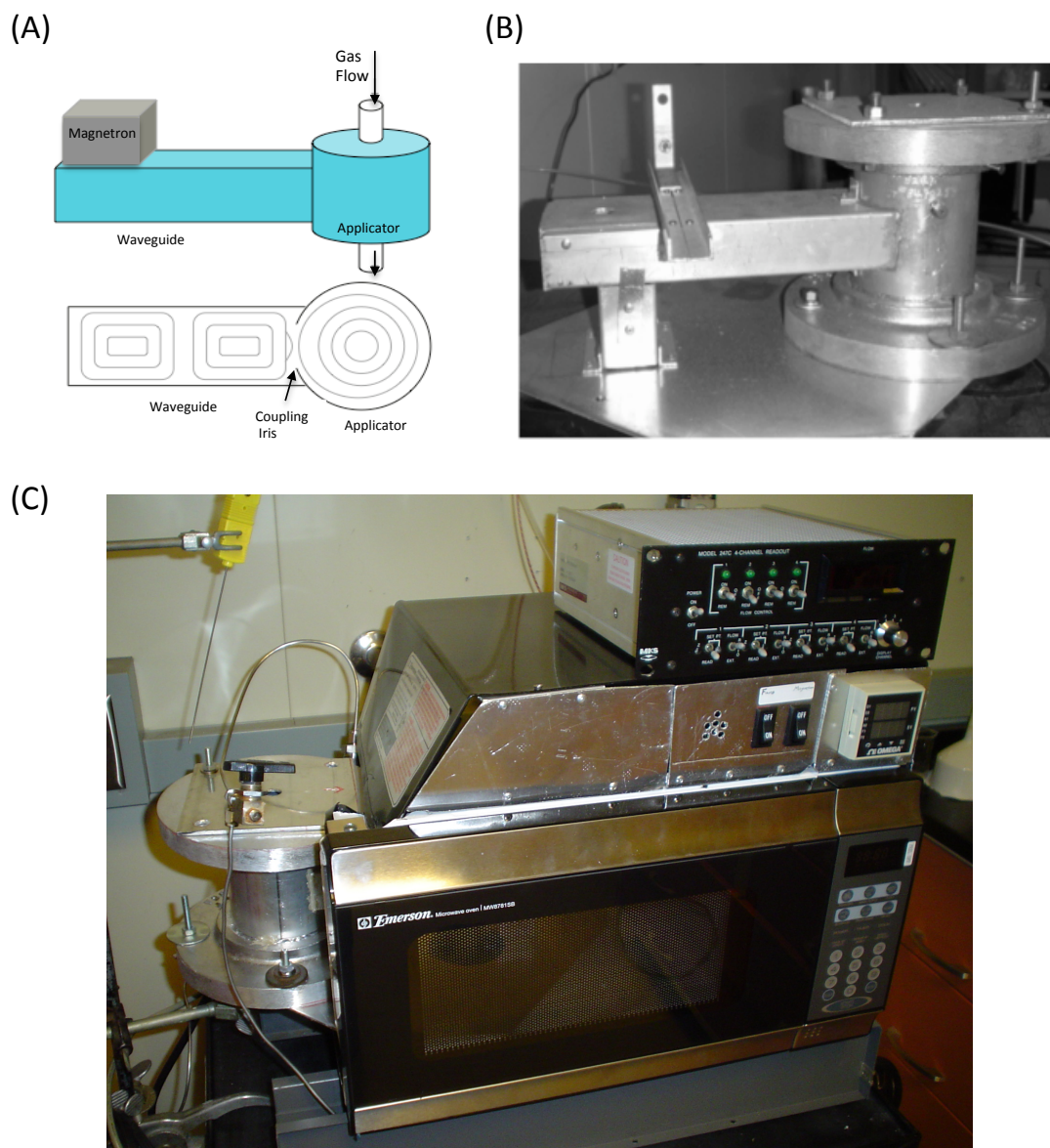


Figure 2.1: Magnetically coupled twin cavity TE mode microwave cavity design. (A) External view and internal field distribution. Sizing of the cavity and iris are dependent upon loading characteristics which dictate the waveguide wavelength. (B) Completed cavity made of aluminum with magnetron removed from left side of waveguide. (C) Completed system installed using a consumer microwave power supply.

2.2.2 Catalyst Preparation

Catalysts used in this study consist of cordierite honeycomb monoliths (Dow Corning 400 cpsi 6 mil) washcoated with material consisting of 10 wt.% Ni supported on $\text{Ce}_{0.75}\text{Zr}_{0.25}\text{O}_2$ (Ni/CZO) to a final washcoat loading of 20 ± 2.4 wt.%. Monoliths minimize pressure drop during high coking experiments, and disperse the catalyst spatially, reducing electromagnetic field inhomogeneity due to conduction losses and runaway heating of the catalyst. High nickel loading was deliberately used to increase the propensity toward carbon formation. $\text{Ce}_{0.75}\text{Zr}_{0.25}\text{O}_2$ is prepared by the co-precipitation of $\text{Ce}(\text{NO}_3)_3 - 6 \text{H}_2\text{O}$ and $\text{ZrOCl}_2 - 8\text{H}_2\text{O}$ in de-ionized (DI) water using a 4 M solution of NH_4OH . Subsequently the slurry is filtered, washed with DI water and calcined at 900 °C in air for 2 hours. Nickel was added via incipient wetness impregnation with $\text{Ni}(\text{NO}_3)_2 - 6\text{H}_2\text{O}$ in DI water to achieve 10 wt.% Ni on CZO. The Ni/CZO was then calcined in air at 900 °C for 2 hours.

Washcoat preparation consisted of crushing Ni/CZO to less than 120 mesh and adding to DI water for a final concentration of 37.75 wt.% Ni/CZO, 0.5 wt.% Hydroxyethylcellulose (temporary binder, to increase viscosity and aide in suspension of solids), 1.25 wt.% 30 - 60 nm Yttria Stabilized Zirconia, Inframat Advanced Materials (binder) and 0.5 wt.% Duramax D-3005 Dispersant, Rohm and Haas. The mixture was milled with 300 5 mm diameter Zirconia balls at 58 rpm for 4 h. Cordierite monoliths were cut into pieces 1 cm in diameter and 2 cm in length followed by calcination at 900 °C in air for 4 h. The washcoating slurry was prepared by adding DI water to the previously ballmilled media, reducing the solids concentration to 20 wt.%. Monoliths are washcoated by briefly immersing a monolith into stirring washcoat slurry and blowing out excess liquid with compressed air. Monoliths are then dried at 110 °C for 2 h before calcination in air at 500 °C for 2 h. Washcoating was repeated until the sample has reached a washcoat concentration of 20 wt.%. Before use, coated monoliths were calcined in air at 900 °C for 2 h followed by reduction in H_2 at 600

°C for 1 h. Acetone sonication was used to verify washcoat stability. Calcination temperatures were chosen to exceed temperatures experienced during operation, to ensure that catalysts were thermally stabilized prior to use.

2.2.3 Flow Reactor Description

Reforming experiments were carried out using a custom single-mode microwave reactor. The system consists of a vertically mounted Carbolyte clamshell furnace mounted above the sample chamber of a microwave waveguide (Gerling Applied Engineering Inc. 2.45 GHz 1.8 kW Continuous-wave). The microwave system is equipped with a 3-stub tuner, sliding short circuit, forward and reverse power meters and circulators to control forward and reverse power transmission while maintaining a stable magnetron frequency. The system was operated in a down-flow configuration to pre-heat the feed and catalyst by forcing hot-air from the furnace into the microwave chamber. The catalyst was loaded onto a constriction within a 1/2" O.D. quartz tube. To ensure that pre-combustion does not occur within the furnace, an 1/8" O.D. quartz tube is inserted into the 1/2" tube to carry the reductants through the heated zone, separate from the oxidizer. Once through the furnace, the two streams meet on a bed of 1/8" quartz rod fragments to ensure thorough mixing, followed by a bed of quartz wool directly on top of the catalyst, ensuring an even flow of gas through all channels. Reactor pressure was maintained at 3.5 ± 0.5 psig.

Requirements for a tunable and reliable microwave system led to the design of the aforementioned system. Schematics of the system as constructed are shown in Figure 2.2A. Major features include the capability to feed both gases and liquids, fast switching via a 4-way valve to ensure consistent startup and shutdown, heated vaporization lines as well as reaction zones within the furnace and microwave cavity. Figure 2.2B is a more detailed schematic of the microwave system with a photograph of the system shown in Figure 2.3. The microwave delivery system consists of a 1.8 kW

continuous-wave power supply, magnetron head, forward and reverse circulators with variable forward attenuation, power monitor, tuning stubs, custom copper applicator port with water cooling and a sliding short circuit to terminate the chamber. All of these components are used to generate and control the delivery of microwaves while monitoring power delivered to the sample. Water cooling is provided for several of the microwave components with air cooling supplied to the optical pyrometer. To pre-heat the microwave sample chamber, air is injected into the furnace and forced downward around the sample tube.

With multiple users in lab, the reactor system was designed to be flexible for use on multiple projects. To ensure user-friendly operation and repeatability, automation was used in the form of a Programmable Logic Controller (Eaton ELC-PLC). The use of a PLC allowed the incorporation of safety protocols within the Ladder Logic to ensure safe operation in the event of communication failure with the computer or power outage, as well as the incorporation of low-level safety interlocks. Experimental Procedures may be entered into the computer to produce consistent results and automate routine tasks such as catalyst reduction.

Use of a PLC allowed for more analog outputs than data acquisition boards from National Instruments generally supply, allowing for the complete automation of gas and liquid flow controllers as well as control over the furnace set points and microwave power settings. Digital inputs are used for an emergency stop button as well as a flow sensor to ensure that cooling water is flowing before the microwave can be enabled along with microwave status detection. A hard-wired control box positioned outside the hood has a master power switch as well as indicator lights and a user-specified warning alarm. With an Internet connection the system may be monitored and operated remotely. I/O available in this system include 8 Thermocouple channels, 10 analog outputs, 10 analog inputs, 12 digital inputs and 12 digital outputs. Custom serial device drivers were written to communicate between Matlab and the PLC over

modbus protocol and have been published online [95].

2.2.3.1 Microwave Operation

Completion of the microwave reactor and data logging systems allowed for the measurement of forward (transmitted) and reverse (reflected) power within the microwave cavity, the difference of which is adsorbed by the sample and sample chamber. The cavity is tuned using tuning stubs and a sliding short circuit to maximize absorption while minimizing reflection, effectively coupling the maximum of the electromagnetic field with the sample.

Several catalysts consisting of Ni impregnated on cordierite monoliths were fabricated to verify operation of the microwave cavity in accordance with expected trends in material properties. Ni impregnated in cordierite is extremely prone to coking. Figure 2.4A displays a fresh monolith, unused catalyst, as well as catalysts after 5, 20 and 60 minutes of propane partial oxidation at a gas hourly space velocity (GHSV) of 30,000, O/C of 1.0 and furnace temperature of 500 °C. Carbon growth within the cordierite pore structure quickly compromises the structural integrity, leading to monolith disintegration. Figure 2.4C shows the relative adsorbed power of a 4 wt.% Ni impregnated on Cordierite sample pre- and post-POX (5 minutes Propane/Air GHSV = 30,000, O/C = 1.0). Carbon deposited on the catalyst has a high dielectric loss and is easily measured, providing a possible means of measuring carbon content on-stream. Using this method of measurement the dependence of absorbed power on Ni weight loading was examined in Figure 2.4B. Beyond very low loadings the relationship is essentially linear, consistent with a weak dependence on particle size at frequencies of 2.45 GHz [62]. At a Ni loading of 2 wt.%, absorbed power readings were below the limit of detection for the system. Low power absorption suggests that microwave heating of the catalyst may prove difficult as heat transfer away from the metallic Ni particles may prevent a substantial temperature rise. Several experiments

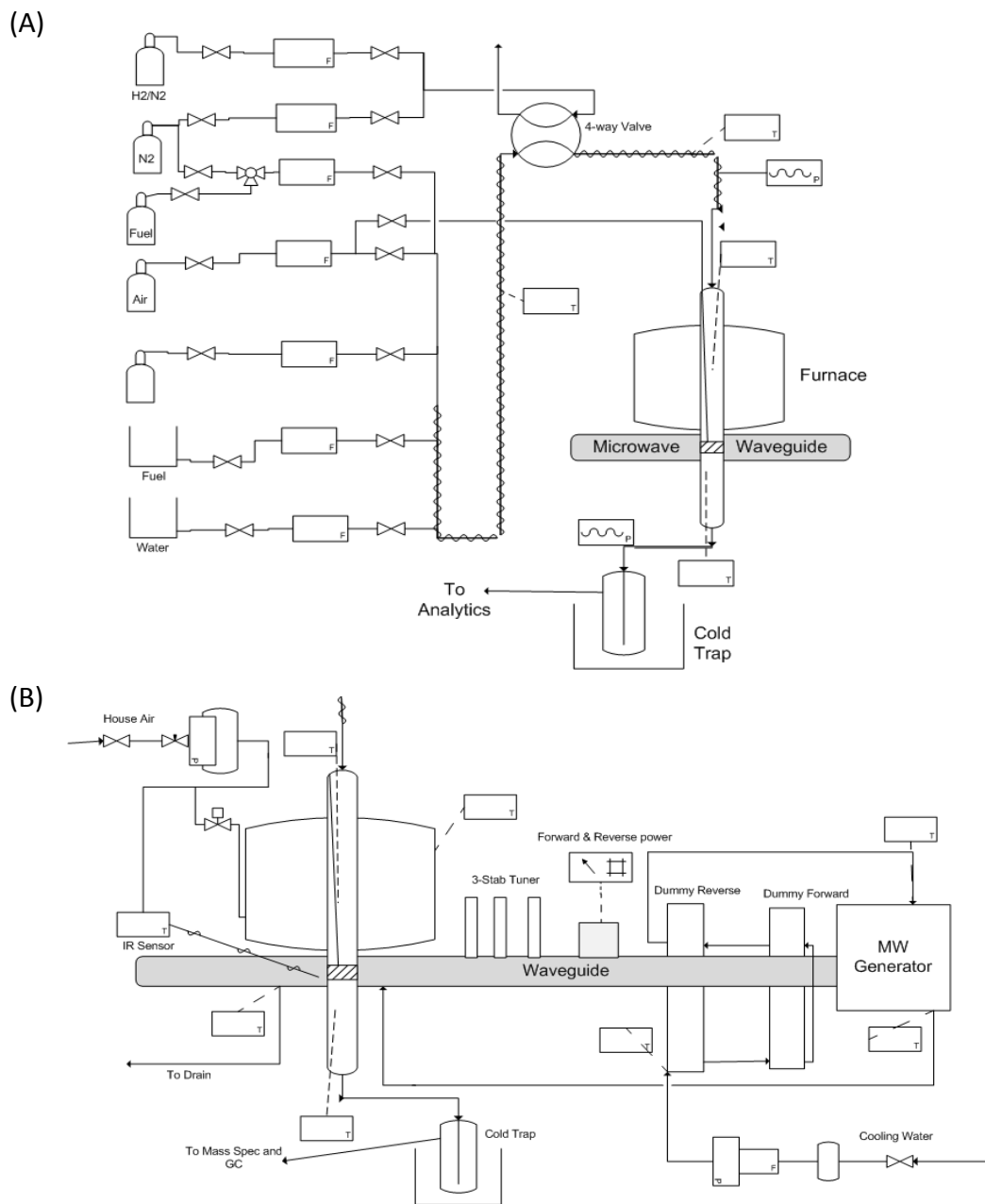


Figure 2.2: (A) Overall gas flow diagram for hybrid microwave-thermal reactor including gas and liquid feeds, 4-way valve, heated lines and furnace. (B) Diagram of microwave system with water cooling and instrumentation.

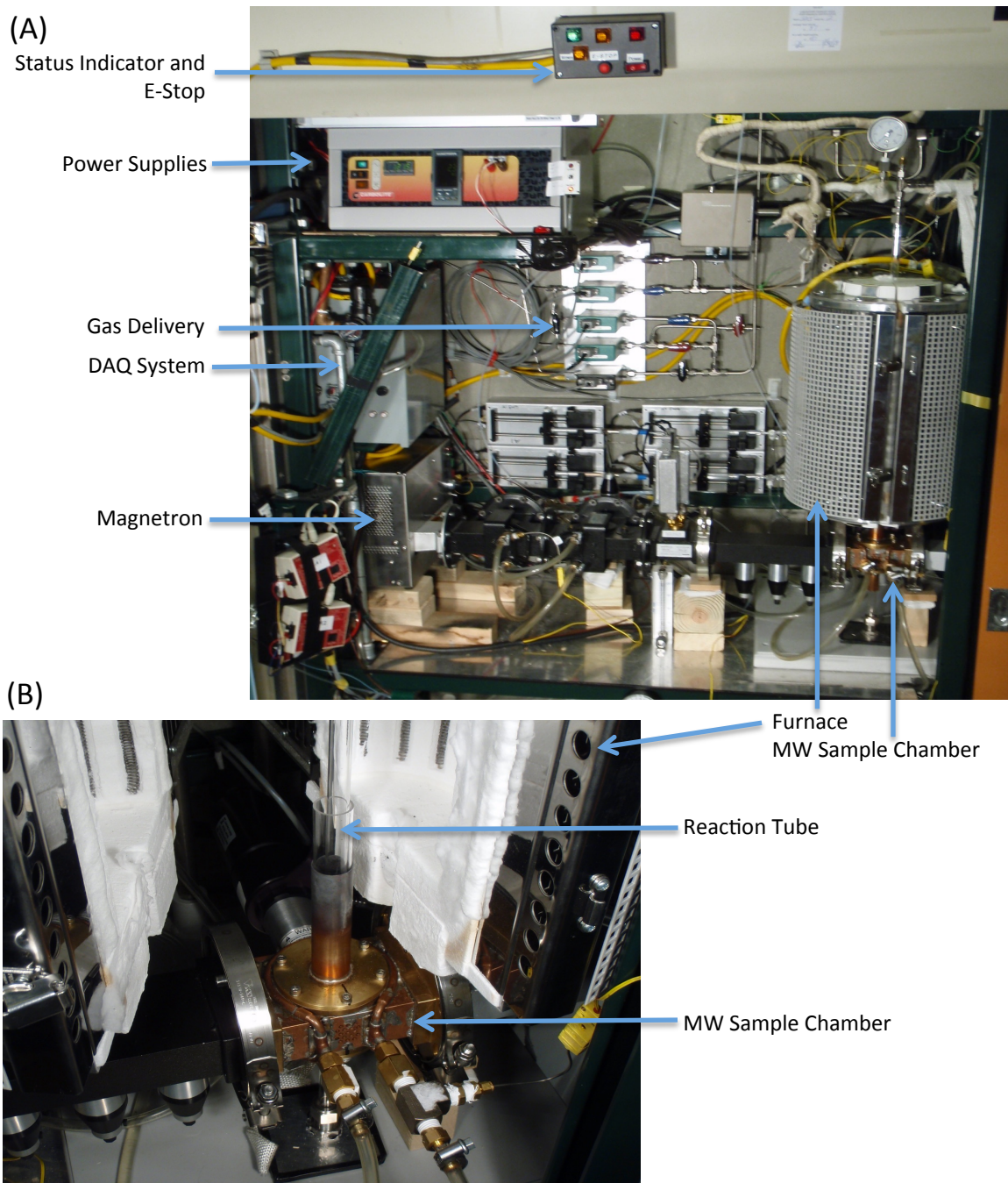


Figure 2.3: (A) Overview of the reactor system situated within a walk in hood. (B) Closeup view of the Microwave applicator.

were carried out to determine if samples experienced sufficient absorbance at low temperatures to overcome heat losses and initiate lightoff. It was found that 9 wt.% Ni on cordierite was required to induce lightoff by microwaves alone. The ability to quickly initiate reactions by microwave irradiation could potentially benefit some industries. Within automotive emissions control, shaving seconds off of lightoff can result in significant emissions reductions. Other experimenters using adiabatic reactors often use methane, hydrogen, or an external blowtorch to start their systems, though this information rarely makes it into the literature. In addition to quickly initiating reactions, experiments have shown the ability for oxidized catalysts to be reduced using microwave heating without additional thermal input. Oxidized catalysts absorb far less power than a reduced sample, making it more difficult to heat and limiting the procedure to high metal loadings or particularly high dielectric loss materials.

Experimental runs using cordierite blanks confirm no blank activity with a furnace pre-heat of 600 °C, corresponding to a sample pre-heat temperature of 250 °C. Gas flow was controlled by MKS flow controllers with DI water fed via syringe pump and vaporized in heat-traced lines prior to entering the furnace. Gases were routed through a 4-way valve for fast startup and shutdowns in the desired atmosphere. Temperature measurements were taken using type-K thermocouples when possible, however use of a thermocouple in the presence of a microwave field was not possible. An optical infrared (IR) temperature sensor (Raytek TX) was employed to measure the external temperature of the catalyst and was calibrated to the sample emissivity before use. The system is controlled via a Programmable Logic Controller (Eaton ELC-PLC) slaved to a computer using a graphical user interface within Matlab[®] to handle data acquisition and control [95].

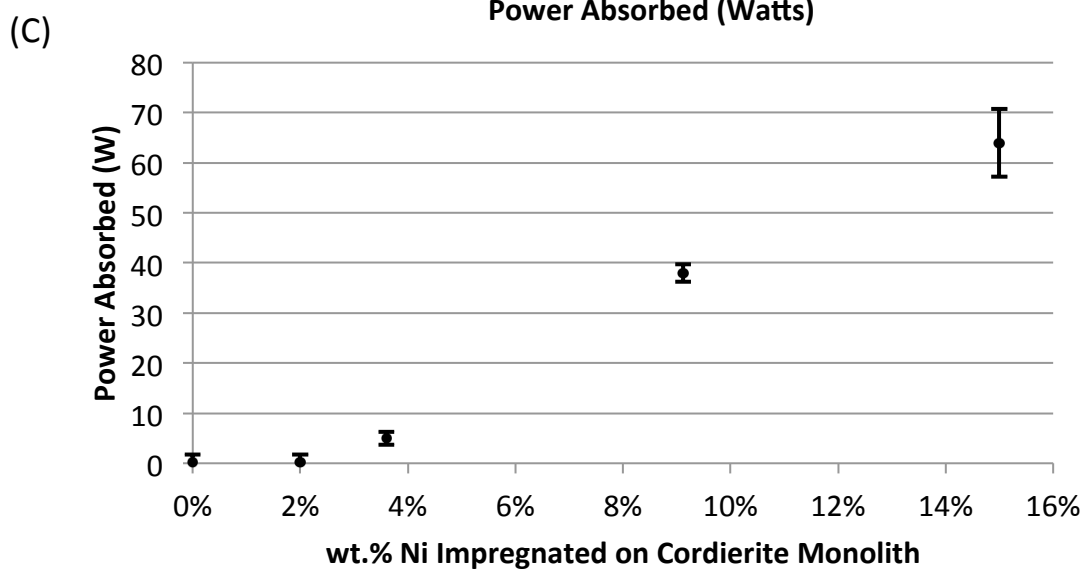
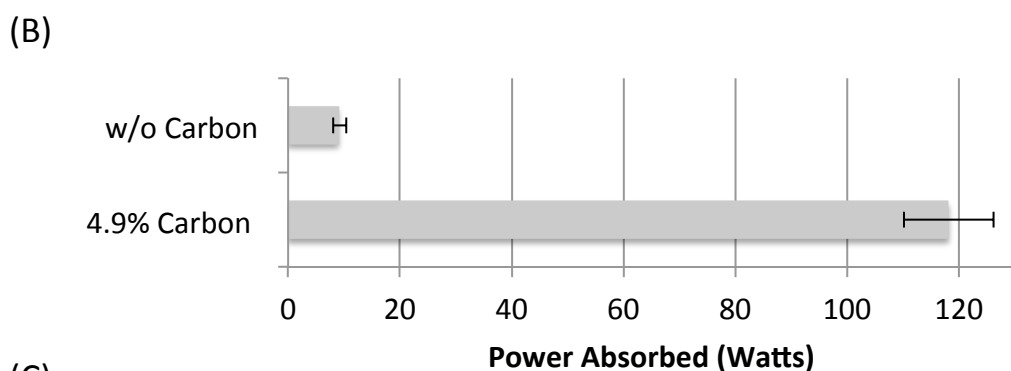
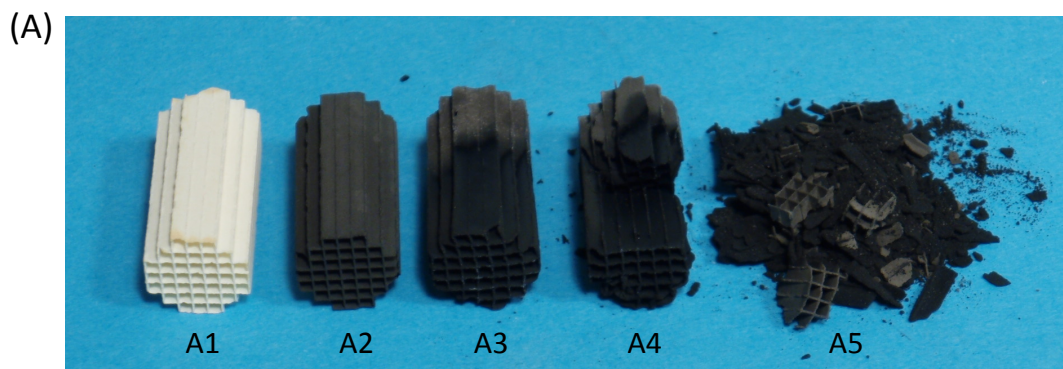


Figure 2.4: (A) Catalysts with varying levels of coke deposition from propane partial oxidation (GHSV = 30,000, O/C = 1.0 Furnace = 500°C). (A1) fresh cordierite monolith, (A2) fresh reduced catalyst, (A3) 5 minutes POX, (A4) 20 minutes POX, (A5) 60 minutes POX. (B) Absorbed power of a 4 wt% Ni impregnated on Cordierite sample pre and post partial oxidation (5 minutes Propane/Air GHSV = 30,000, O/C = 1.0). (C) Absorbed microwave power as a function of impregnated Ni loading on Cordierite monoliths.

Table 2.1: Operating conditions for POX and ATR experiments.

	POX Conditions	ATR Conditions
GHSV	65,000	86,762
O/C	0.47	0.47
H ₂ O/C	0.0	0.50
Air Flow, mmol min ⁻¹	56.4	56.4
Propane, mmol min ⁻¹	10.1	10.1
Ethylene, mmol min ⁻¹	10.1	10.1
Water, mmol min ⁻¹	0.0	25.6

2.2.4 Reaction Conditions

The prepared catalysts were tested for activity in the reforming of a propane-ethylene mixture under varying levels of irradiation. Two significant metrics employed in describing the feed of a reforming system include the atomic oxygen-to-carbon ratio, O/C, and the water to atomic carbon ratio, H₂O/C. From these ratios one can compute the respective quantities of O₂, H₂O, and fuel present. Experimental conditions were chosen to examine catalytic performance and carbon deposition under harsh operating conditions. A mixture of 50 mol.% Propane and 50 mol.% Ethylene was used as the fuel to simulate a high coking feed. Using these metrics and air as the source of O₂, the equilibrium product compositions were determined via an adiabatic Gibbs free energy minimization within ASPEN Plus[®]. Figure 2.5 shows the equilibrium production of Hydrogen as a function of the O/C and H₂O/C ratios. The two marked points represent experimental conditions used in this study with their respective adiabatic operating temperatures. Experimental conditions are well outside those of optimal yield, containing far less total oxygen than previous studies [96, 14]. Table 2.1 describes the experimental conditions studied of partial oxidation and autothermal reforming, henceforth referred to as the POX and ATR conditions. As all experiments were carried out adiabatically, the quantity of O₂ and fuel was kept constant while performing experiments with and without steam to provide a sufficient exotherm as to not extinguish the reaction.

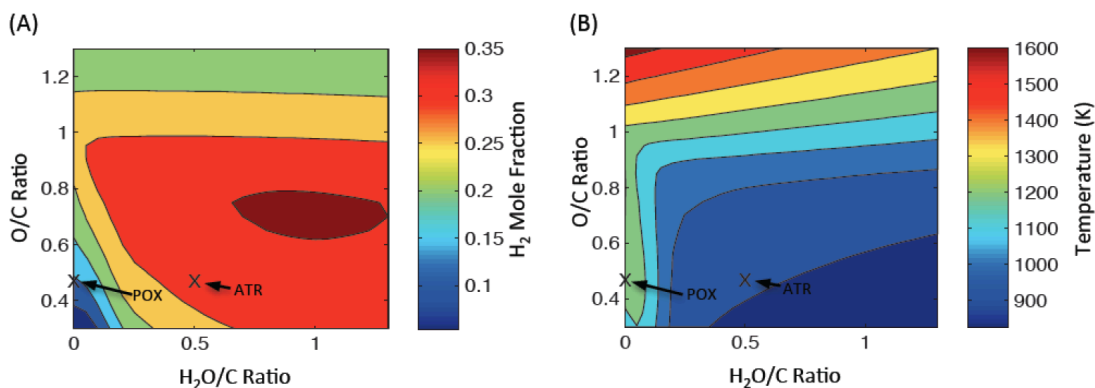


Figure 2.5: Hydrogen mole fractions (A) and adiabatic reactor temperatures (B) as a function of the atomic oxygen to carbon and water to carbon ratios at a feed temperature of 250 °C as calculated by ASPEN. Species considered in the Gibbs free energy minimization include: H_2 , H_2O , O_2 , N_2 , CH_4 , C_2H_2 , C_2H_4 , C_2H_6 , C_3H_6 , C_3H_8 , CO and CO_2 .

For each experiment a single monolith 0.76 ± 0.025 g (1.57 cm³) was loaded into the flow reactor capable of exposing samples to controlled levels of microwave radiation (0 - 900 watts). All tests were performed a minimum of three times with fresh catalysts over reaction periods of 15 minutes. This length of time was chosen based on the coking characteristics of the POX system as shown in Figure 2.6. Carbon mass increases quickly at first, followed by a slower growth of carbon on the sample. Experiments of longer duration and/or of greater microwave power are possible, however complicating factors arise from the onset of plasma formation at high microwave power settings and long times. Carbons conductive nature is beneficial in assisting its removal by microwave, however it also leads to the formation of conduction paths that generate localized high voltage gradients leading to dielectric breakdown of the surrounding gas. In addition to conducting forms of carbon, carbon black is also a strong microwave absorber. Protruding geometries downstream of the catalyst such as ‘dimple’ supports in a quartz tube were found to be particularly effective at inducing plasma formation under high coking conditions.

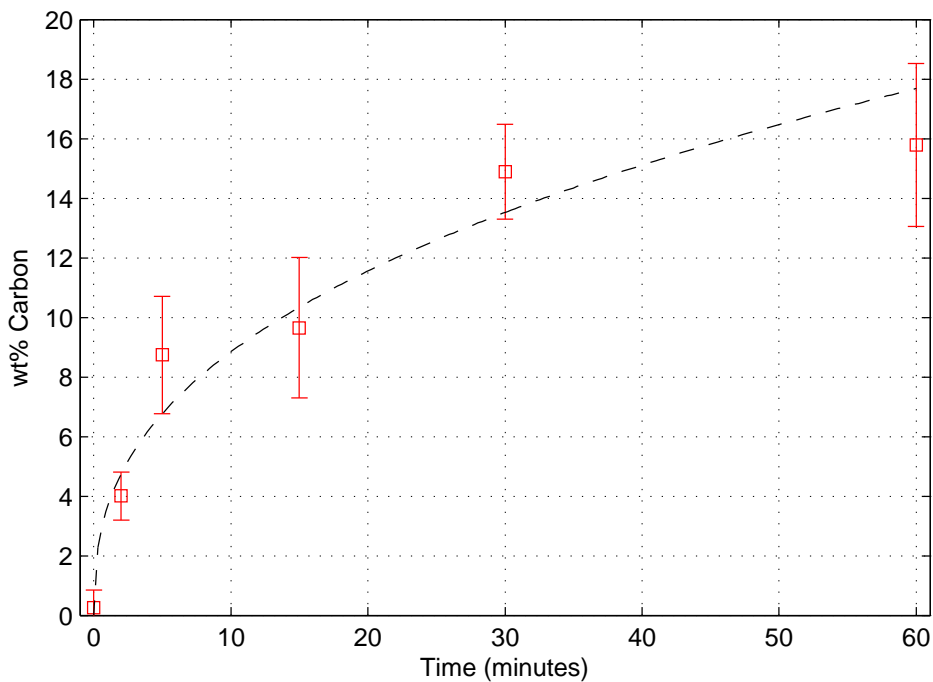


Figure 2.6: Coking behavior of Ni/CZO/Cordierite catalyst under POX conditions. Mean values with standard deviations, exponential trend line.

2.2.5 Reactor Startup and Shutdown

Pre-reduced monoliths were loaded into the reactor, blanketed by N_2 , and the furnace ramped to $600\text{ }^\circ\text{C}$ to achieve a catalyst pre-heat temperature of $250\text{ }^\circ\text{C}$ within the microwave cavity. Light-off is initiated using a three stage process to simultaneously raise the catalyst temperature while maintaining a rich mixture outside of the upper flammability limit. First, H_2 ($53.6\text{ mmol min}^{-1}$) is combusted with air ($14.3\text{ mmol min}^{-1}$) for 4 minutes, raising the catalyst temperature to $\sim 460\text{ }^\circ\text{C}$. Secondly, C_3H_8 ($19.9\text{ mmol min}^{-1}$) is reacted with air ($132.1\text{ mmol min}^{-1}$) for 1 minute to further pre-heat the catalyst above $700\text{ }^\circ\text{C}$. It has been verified that no carbon is deposited during the startup phase of propane partial oxidation by TPO analysis. Finally the experimental mixture described in Table 2.1 is fed to the catalyst. Startup under net-reducing conditions ensures that the nickel is reduced when experiments begin. At the end of an experiment, reactions are extinguished under N_2 to preserve the

state of the catalyst and cooled to room temperature before removal. Monoliths are bisected for observation, crushed and mixed for analysis to ensure uniform sampling. Blank runs were performed with no conversion observed.

2.2.6 Analysis of Reforming Behavior

Reactions were monitored for selectivity and activity under the prescribed conditions, simulating short-term deleterious operation. Pseudo steady state conditions are established within the first few minutes with the subsequent concentration information used for analysis. The reactor effluent passes through a 0 °C trap to remove water before sampling by a Mass Spectrometer (MS, Ametek Dycor Proline) scanning an m/z range of 1 - 50. Calibration was performed using multiple calibration gas standards to determine relative ionization intensities around the concentrations of interest. Calibration data was combined with electron ionization data from the NIST Chemistry Database [97] in an adaptive mass spectrum deconvolution program to track the concentrations of: H_2 , H_2O , O_2 , N_2 , CH_4 , C_2H_2 , C_2H_4 , C_2H_6 , C_3H_6 , C_3H_8 , CO , CO_2 , and Ar . Additional information on the MS calibration is available in Appendix C. Due to the removal of water from the effluent, quantification of water produced or consumed in the reaction was not possible. Total effluent flow is calculated using N_2 as an internal standard. Yields and conversions are calculated on a molar basis according to Equations (2.1) to (2.12). Maximum synthesis gas yield, Y_{sg} , is frequently used as a metric of system performance. Within this study, conversion of the fuel is kept low and thus synthesis gas yield alone is not a sufficient performance metric. Due to the low amount of O_2 supplied, reactions 1.1 to 1.4 are severely stoichiometrically limited leading to the formation of many intermediate cracking and dehydrogenation products. Equilibrium calculations such as those shown in Figure 2.5 were obtained for adiabatic and isothermal reactor operation for comparison with experimental results. The system under consideration operates adiabatically above

the pre-heat temperature, however incomplete conversion and substantial heat loss leads to a lower than expected exit temperature and decreased yields compared with equilibrium predictions.

$$Y_{H_2} = \frac{F_{H_2,out}}{4 \times F_{C_3H_8,in} + 2 \times F_{C_2H_4,in}} \quad (2.1)$$

$$Y_{CO} = \frac{F_{CO,out}}{3 \times F_{C_3H_8,in} + 2 \times F_{C_2H_4,in}} \quad (2.2)$$

$$Y_{sg} = \frac{F_{H_2,out} + F_{CO,out}}{7 \times F_{C_3H_8,in} + 4 \times F_{C_2H_4,in}} \quad (2.3)$$

$$Y_{CO_2} = \frac{F_{CO_2,out}}{3 \times F_{C_3H_8,in} + 2 \times F_{C_2H_4,in}} \quad (2.4)$$

$$Y_{CH_4} = \frac{F_{CH_4,out}}{3 \times F_{C_3H_8,in} + 2 \times F_{C_2H_4,in}} \quad (2.5)$$

$$Y_{C_2H_2} = \frac{2 \times F_{C_2H_2,out}}{3 \times F_{C_3H_8,in} + 2 \times F_{C_2H_4,in}} \quad (2.6)$$

$$Y_{C_2H_4} = \frac{2 \times F_{C_2H_4,out}}{3 \times F_{C_3H_8,in} + 2 \times F_{C_2H_4,in}} \quad (2.7)$$

$$Y_{C_2H_6} = \frac{2 \times F_{C_2H_6,out}}{3 \times F_{C_3H_8,in} + 2 \times F_{C_2H_4,in}} \quad (2.8)$$

$$Y_{C_3H_6} = \frac{3 \times F_{C_3H_6,out}}{3 \times F_{C_3H_8,in} + 2 \times F_{C_2H_4,in}} \quad (2.9)$$

$$Y_{C_3H_8} = \frac{3 \times F_{C_3H_8,out}}{3 \times F_{C_3H_8,in} + 2 \times F_{C_2H_4,in}} \quad (2.10)$$

$$X_{C_2H_4} = 1 - \frac{F_{C_2H_4,out}}{F_{C_2H_4,in}} \quad (2.11)$$

$$X_{C_3H_8} = 1 - \frac{F_{C_3H_8,out}}{F_{C_3H_8,in}} \quad (2.12)$$

2.2.7 Catalyst Characterization

Samples were characterized by single-point BET N₂ physisorption on a Quantachrome ChemBET instrument to obtain measurements of physical surface area. Samples were degassed at 300 °C for 3 h before N₂ physisorption at 77 K. Metallic surface area and dispersion measurements were performed by H₂ chemisorption using a Micromeritics ASAP 2020 instrument. Samples were degassed under vacuum at 300

°C, followed by reduction in flowing H₂ at 600 °C. Measurements were taken at 35 °C, obtaining two complete isotherms to determine the quantity of strongly adsorbed hydrogen, thereby calculating the number of exposed metallic sites.

Temperature programmed oxidation (TPO) and reduction (TPR) experiments were performed gravimetrically using a TA instruments Q500. Samples were initially heated to 120 °C to remove any adsorbed water before ramping at 7.5 °C min⁻¹ to 850 °C in 60 sccm of air or 20 vol.% H₂ in N₂ with a balance purge of 40 sccm N₂. TPO is used as a means to observe and quantify carbon deposits, with TPO and TPR used to observe the oxidation-reduction behavior of Nickel and the CZO support.

X-ray diffraction (XRD) was performed on powdered samples using a Rigaku 12-kW high intensity rotary anode generator with a Cu K α source. A graphite-diffracted beam monochromator removed K β radiation. XRD patterns for the various components of the catalyst system are shown in Figure 2.7. The use of cordierite as a support introduces many peaks to the XRD spectrum making analysis of peaks associated with graphitic structures difficult to identify. Nickel particle size determination by XRD yielded large errors due to overlapping peaks.

Scanning electron microscopy (SEM) was employed to observe carbon morphologies using a Philips XL30FEG SEM instrument.

Raman analysis was performed to observe changes in carbon morphology by monitoring the peaks attributed to more and less crystalline carbon around 1590 and 1380 cm⁻¹ respectively. Peaks were integrated and their respective ratios reported to gauge changes in the morphology of carbon present. Analysis was performed on a Lambda Solutions, Dimension P1 Raman system.

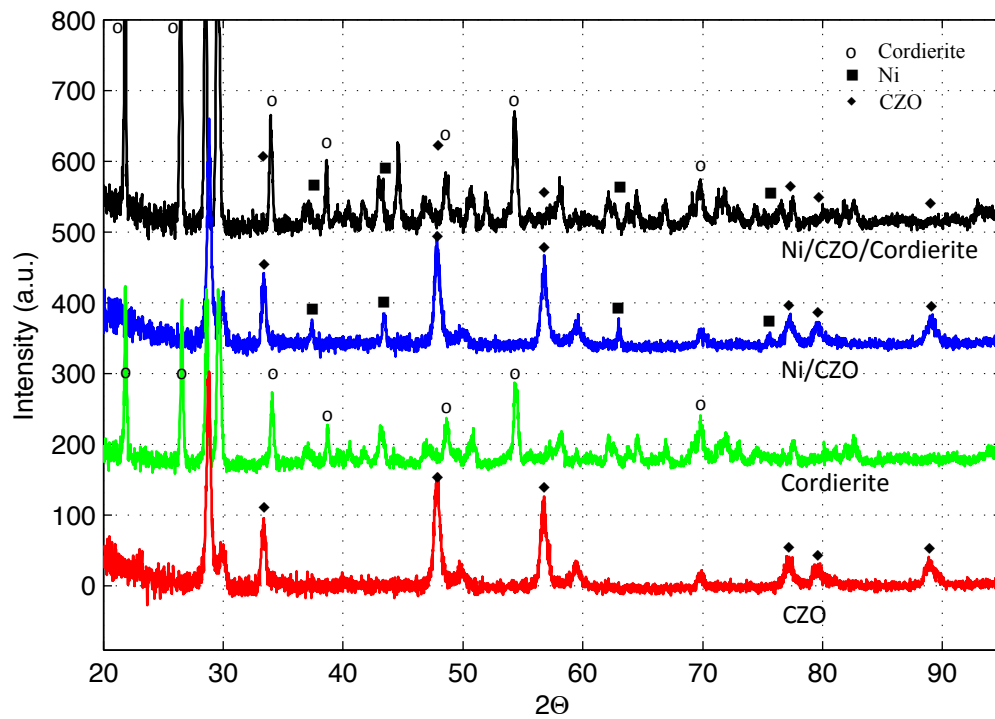


Figure 2.7: XRD patterns of $\text{Ce}_{0.75}\text{Zr}_{0.25}\text{O}_2$, blank cordierite, 10 wt.% Ni on $\text{Ce}_{0.75}\text{Zr}_{0.25}\text{O}_2$ and cordierite loaded with 20 wt.% of washcoat [10 wt.% Ni on $\text{Ce}_{0.75}\text{Zr}_{0.25}\text{O}_2$].

2.3 Results

2.3.1 Partial Oxidation Experiments

Figure 2.8 shows the results for the partial oxidation of a mixed feed of propane and ethylene over monolith supported Ni/CZO catalysts with an O/C ratio of 0.47 and H₂O/C ratio of 0. Data presented are average values of multiple trials with error bars representing the greater of the standard deviation between trials and the propagation of error within the system as described in Appendix D. Steady state concentrations were taken between 4 and 15 minutes of operation for each individual run. Conversions and yields are plotted with respect to the measured transmitted (forward) power in the microwave cavity with 0 W indicating that the microwave source was not used. Microwave power is used as a proxy for the electric field strength (V m⁻¹), as the former is a measurable system parameter and the latter changes based on the catalyst dielectric properties over time but is more descriptive of the local electromagnetic field. Within all experiments reflected power remained high, resulting in a standing wave pattern in the microwave applicator with high electric field strength. Conversion of the feed hydrocarbons, Figure 2.8A, exhibits an increase in the conversion of propane and a corresponding decrease in ethylene conversion with increasing microwave power. Product yields, Figure 2.8B-C, exhibit trends of increasing CH₄, C₃H₆, and H₂ with increasing microwave irradiation. CO also increases, however only after an initial drop, while CO₂ yields steadily decrease. The majority of shifts in product compositions occur below 400 W, with little change observed beyond that level of power input. Power absorption by the sample is provided in Figure 2.8D. Only forward and reflected power is measured, requiring calibrations to determine the power absorption by the cavity walls and sliding short circuit leading to the reported uncertainty.

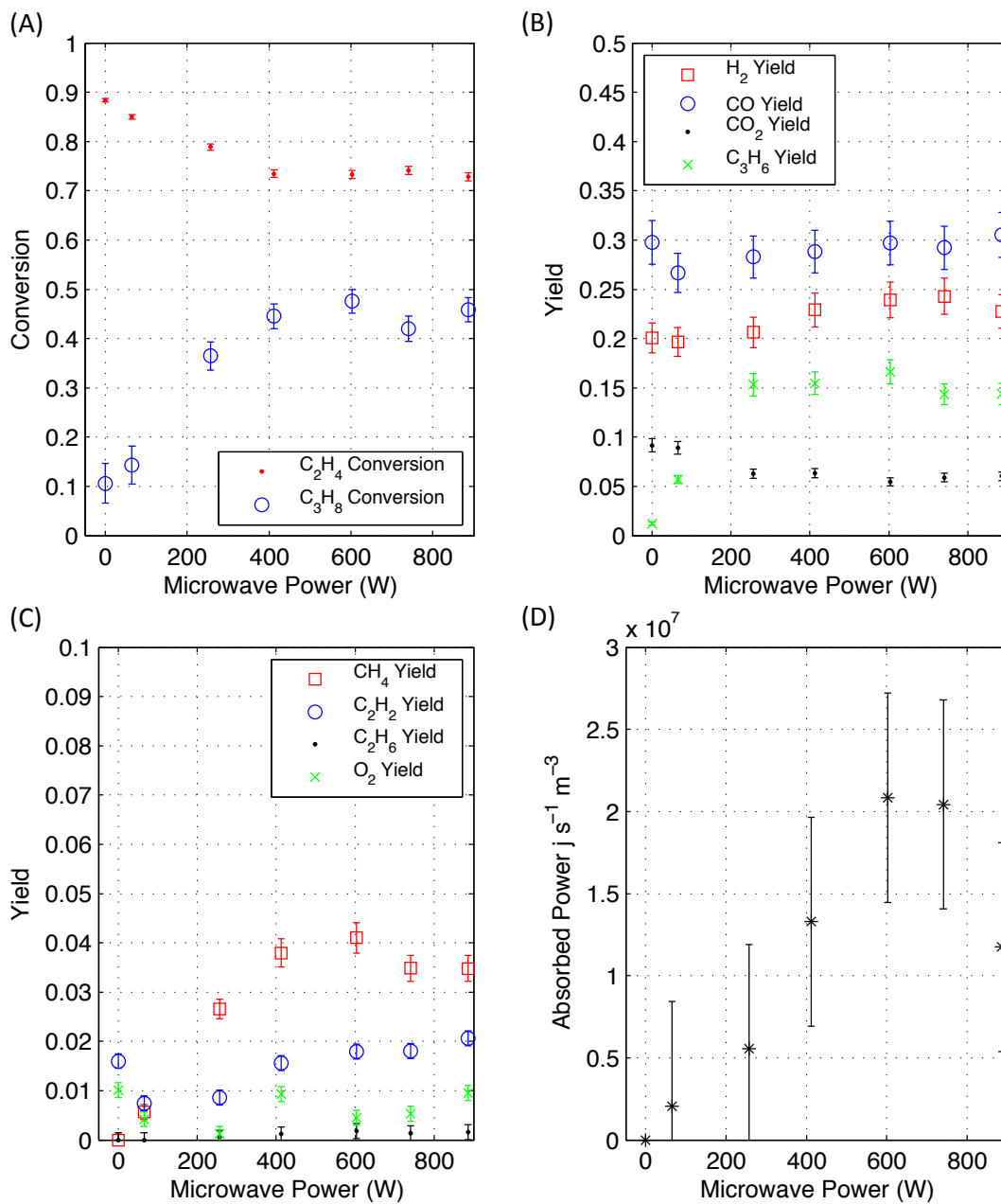


Figure 2.8: POX Results: (A) Conversions, (B-C) Yields and (D) Power absorbed by the catalyst as a function of the applied forward power.

2.3.2 Autothermal Reforming Experiments

Results from experiments involving the ATR of a mixed feed of propane and ethylene with an O/C ratio of 0.47 and H₂O/C ratio of 0.5 are shown in Figure 2.9. In contrast with the POX results presented above, changes in product distributions continue to occur at irradiation levels greater than 400 W. Conversion of C₂H₄ remains near unity while conversion of C₃H₈ increases from 0.15 to 0.62. H₂ and CO yields shown in Figure 2.9B increase with increasing levels of irradiation while CO₂ decreases. Yields of CH₄ and C₃H₆, Figure 2.9C, remain low with only a small amount of propylene detected. Absorbed power is provided in Figure 2.9D.

2.3.3 Temperature Programmed Oxidation and Reduction

Representative TPO peaks for samples having undergone POX operation are shown in Figure 2.10A. Of note is the shift in peak position with increasing irradiation along with the decrease in carbon present on the sample demonstrated by Figure 2.11. POX conditions resulted in the deposition of over 8 wt.% carbon within the 15 minute experimental period, a value that was reduced to 4 wt.% on irradiated samples. ATR TPO peak positions, Figure 2.10B, exhibit a similar shift to higher temperatures under ATR conditions as observed in POX cases. Shifts in TPO peak position indicate a change in carbon morphology, however under ATR conditions there is little change in the quantity of carbon present. The addition of water to the feed increases total available oxygen for the removal of carbon, resulting in the base case condition of 0 W accumulating less than 1.5 wt.% of carbon.

TPR was utilized in conjunction with TPO to observe changes in the catalyst post reaction. Figure 2.12 displays representative TPR data for catalyst having undergone reaction in POX and ATR conditions before and after oxidation to remove carbon and increase the clarity of the TPR features. Post reaction TPR features of POX and ATR systems Figure 2.12A-B, exhibit a similar trend of slightly increasing peak

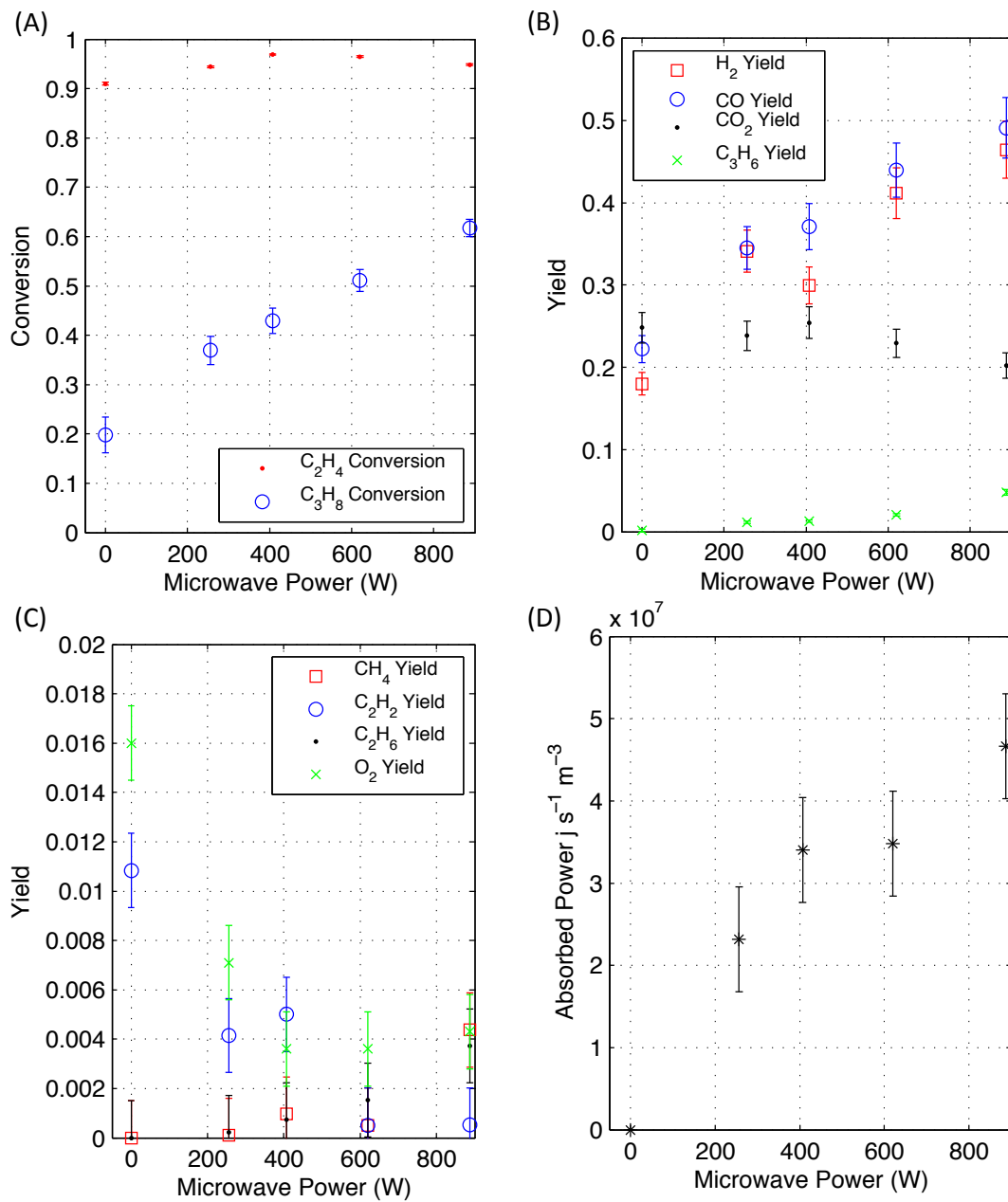


Figure 2.9: ATR Results: (A) Conversions, (B-C) Yields and (D) Power absorbed by the catalyst as a function of the applied forward power.

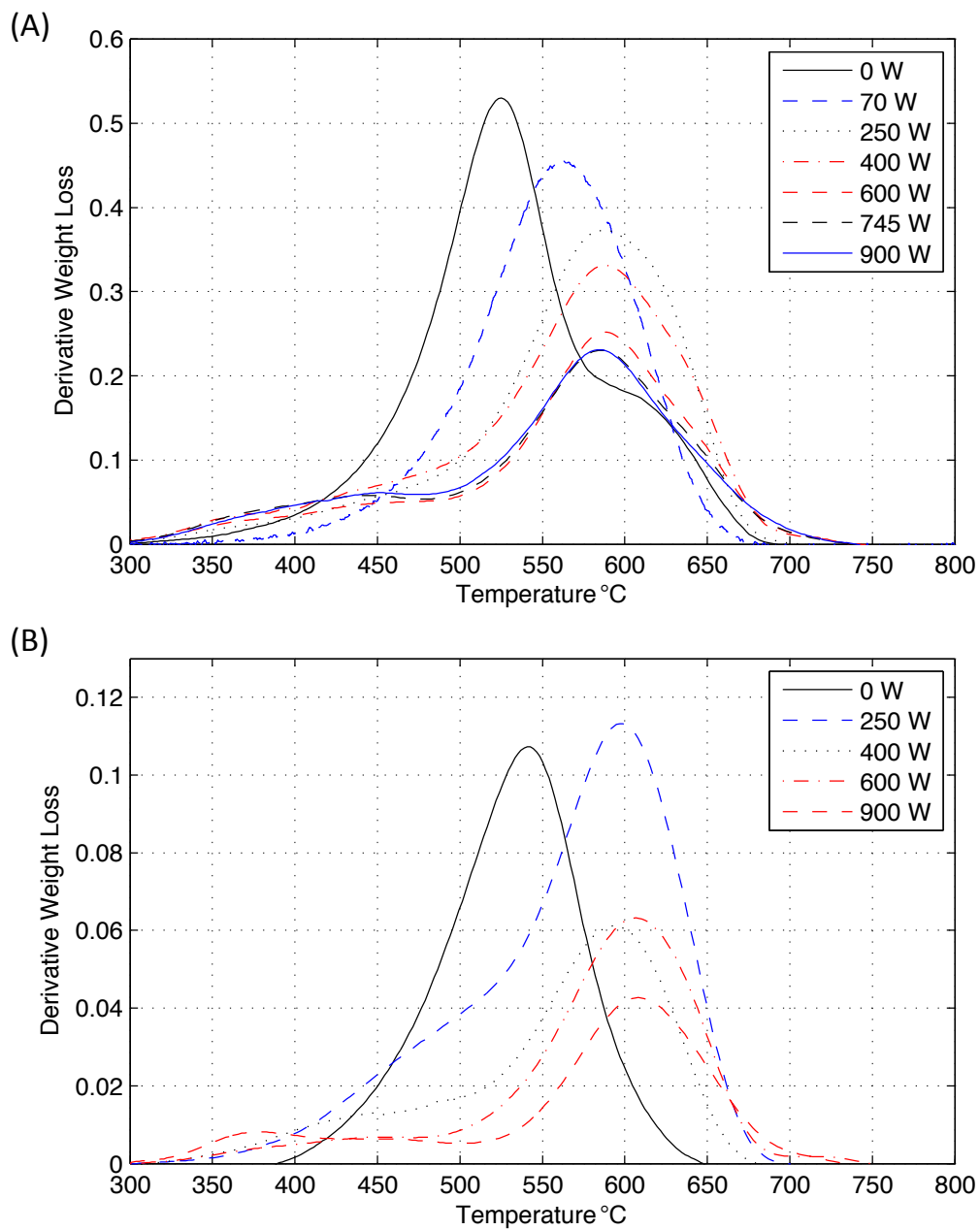


Figure 2.10: Temperature Programmed Oxidation of carbon deposits on catalyst samples after POX (A) and ATR (B) reaction conditions.

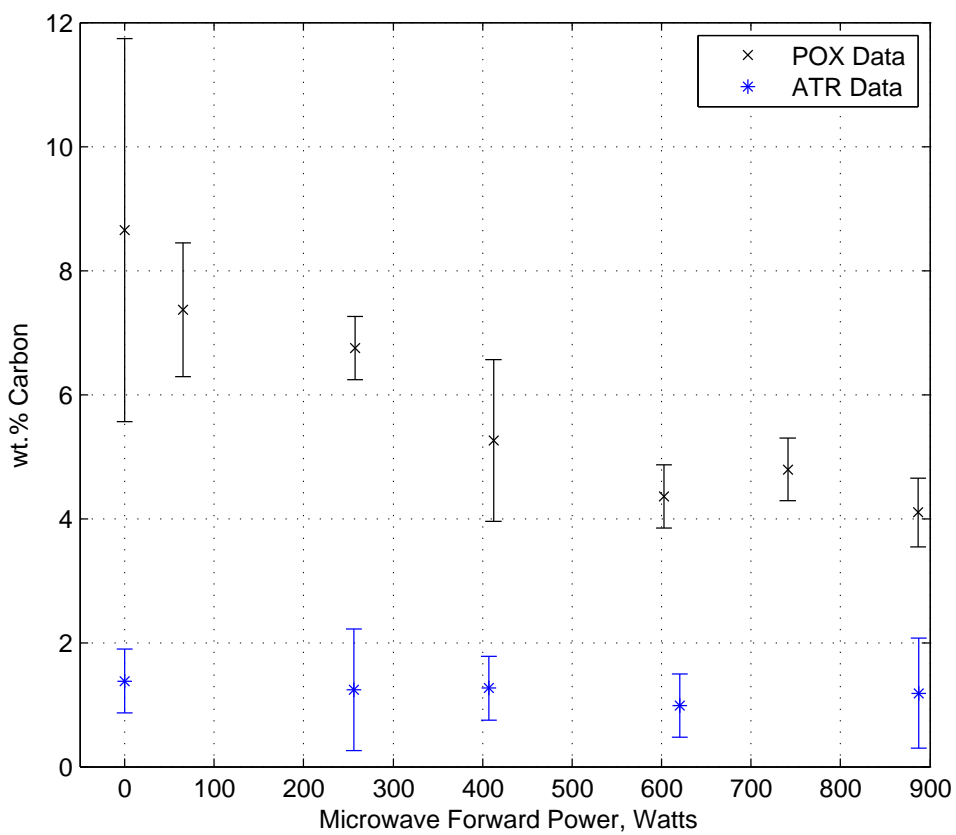


Figure 2.11: Carbon present on catalyst samples after reforming as a function of the applied microwave power.

Table 2.2: Raman carbon analysis: Peak area ratios and standard deviation on measured values.

MW Power (W)	POX D/G Ratio	ATR D/G Ratio
0	1.84 ± 0.55	1.53 ± 0.11
250	1.31 ± 0.05	1.41 ± 0.06
400	1.20 ± 0.07	1.36 ± 0.21
900	1.23 ± 0.20	1.18 ± 0.07

position with increasing levels of irradiation, however above 400 W the POX TPR feature is no longer present, indicating that during reaction the catalyst remains fully reduced. Under ATR conditions, with additional oxygen available, the catalyst remains slightly oxidized. TPR of POX samples after TPO, Figure 2.12C, exhibit a shift in metallic feature reduction at 275 °C to higher temperatures with increasing irradiation levels consistent with the metallic phase being slightly sintered. The same trend was not observed in samples exposed to ATR conditions, Figure 2.12D, likely due to the lower overall temperature of operation reducing the degree of sintering. Increasing levels of radiation exposure also correspond to less O₂ storage by CZO as indicated by the reduction in the CZO peak around 600 °C generally associated with surface oxygen.

2.3.4 Raman Analysis

Raman spectra of crushed catalysts were analyzed for features at 1590 cm⁻¹ associated with graphitic carbon structures (G band), as well as at 1380 cm⁻¹ associated with amorphous carbon (D band). Taking the ratio of the D/G bands provides a description of the level of crystallinity within the sample. Both POX and ATR samples indicate an increase in carbon crystallinity with increasing microwave irradiation as shown in Table 2.2.

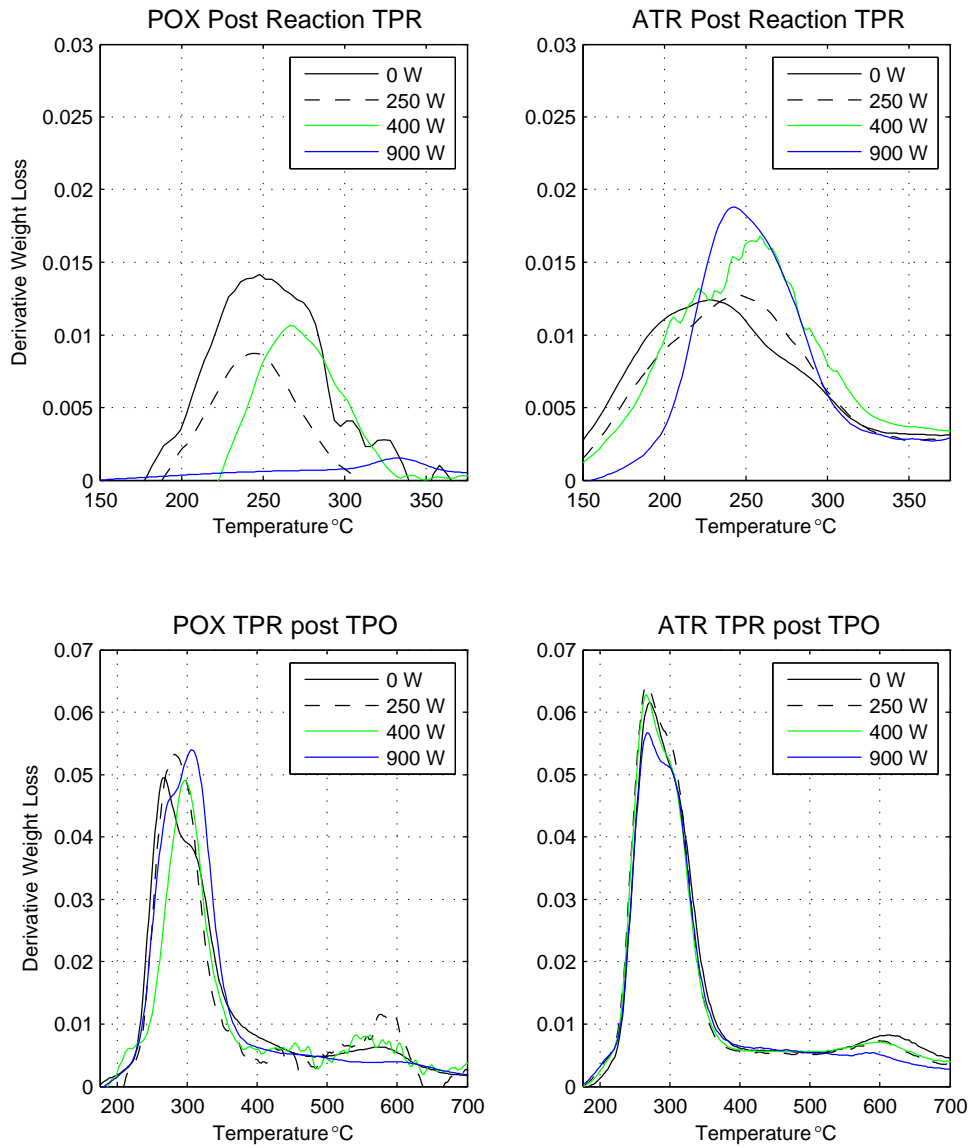


Figure 2.12: TPR derivative weight loss curves for POX catalysts post reaction (A) and post TPO (C) and ATR catalysts post reaction (B) and post TPO (D).

Table 2.3: Chemisorption Results: Dispersion, Metallic surface area and Crystallite size for selected conditions.

	Dispersion %	Crystallite diameter nm
Fresh catalyst	0.56 ± 0.06	182 ± 22
Post reaction POX	0.40 ± 0.12	262 ± 80
Post reaction POX 400W	0.46 ± 0.20	274 ± 178
Post reaction POX 900W	0.36 ± 0.06	278 ± 47
Post reaction ATR	0.25 ± 0.01	406 ± 4
Post reaction ATR 400W	0.41 ± 0.02	249 ± 11
Post reaction ATR 900W	0.50 ± 0.05	203 ± 3

2.3.5 Surface Area Measurements

Single-point BET N₂ physisorption measurements determined the physical surface area of blank cordierite monolith and CZO supports to be $0.26 \pm 0.02 \text{ m}^2 \text{ g}^{-1}$ and $11.8 \pm 0.2 \text{ m}^2 \text{ g}^{-1}$ respectively. Addition of 10 wt.% Ni to CZO decreased the accessible surface area to $6.8 \pm 0.1 \text{ m}^2 \text{ g}^{-1}$. Coated catalysts have a final surface area of $1.19 \pm 0.04 \text{ m}^2 \text{ g}^{-1}$. Post reaction physical surface area measurements show no significant change with reaction conditions. Metallic surface area measurements were performed using H₂ chemisorption on reduced Ni/CZO samples to determine the availability and size of nickel particles. Table 2.3 summarizes the findings with only a small difference between fresh catalyst and those exposed to POX conditions. Under ATR conditions the presence of microwave radiation maintains the nickel dispersion of the catalyst much better than under zero-irradiation conditions, where nickel particle sizes increase considerably. Irradiation appears to retard the effects of sintering in the ATR system. Alternatively, the change in dispersion may be the result of loss of Ni nano particles from the reactor due to carbon filament and nanotube growth under non-irradiated conditions.

2.4 Discussion

Observed changes in product distributions and coking behavior of POX and ATR systems exhibit trends that do not follow simple expectations for a system approaching equilibrium. A significant challenge in catalytic microwave work is the lack of direct temperature measurement by thermocouple. Incomplete conversion, and the inability to directly measure temperature stymie interpretation. Numerous studies have proposed unique abilities of microwaves to influence reactions in ways not reproducible within traditional heating environments. To gain insight into the elevated temperature experienced by a reforming system operating under microwave irradiation, product distributions were compared with those obtained by increasing the system temperature within the heated zone of a furnace. Performing furnace temperature comparisons allows for the determination of what observed trends may be attributed to furnace reproducible thermal effects and what effects are unique to microwave irradiated environments.

2.4.1 Elevated Sample Temperature Composition Comparison

Sample temperatures were increased by placing catalysts within the furnace and increasing the set-point temperature above the standard pre-heat temperature of 250 °C within the microwave waveguide. Within the furnace the catalyst containing section of quartz tubing was wrapped in quartz-wool to prevent the formation of hot spots due to radiation from the furnace heating coils. Catalysts are subsequently run under standard POX or ATR conditions while monitoring the effluent concentrations and temperature, from which a comparison can be made with compositions obtained under microwave conditions. The maximum furnace set-point was 550 °C. Higher temperatures were not attainable within the furnace due to pre-combustion of the feed. Figure 2.13 is an example of the method used to fit microwave data to furnace obtained values in POX and ATR experiments. Furnace conversions or

yields are plotted as a function of exit temperature as measured by a thermocouple placed within a thermowell directly below the catalyst in the center of the reaction tube. Table 2.4.1 contains the exit temperatures observed under each condition, with “Waveguide” indicating that the reaction was carried out in the microwave chamber without irradiation. An extrapolation of the trend observed in the furnace data is then used to match with microwave data. In certain instances the microwave data fits the trends observed under traditional heating quite well; this behavior may be considered traditional thermal effects.

By matching the furnace and microwave yields for each component as demonstrated in Figure 2.13, Figure 2.14 is the effective temperature experienced by each component in a microwave field as compared with a furnace heating environment. Species used in the comparison to obtain average values indicated include H_2 , CO_2 , CH_4 , C_2H_4 , C_2H_6 , C_3H_6 and C_3H_8 for POX conditions and H_2 , CO , C_2H_2 , C_2H_4 and C_3H_8 for ATR experiments. Other species are present at too low of concentrations to be used in this comparison, or the trends in microwave and furnace data differ, preventing a direct comparison. From Figure 2.14A, the relative temperatures experienced by reaction pathways leading to each product can be inferred. For example, it would appear that the dehydrogenation pathway to produce C_3H_6 appears to be at a higher effective temperature at any given power level than the production of H_2 . The low effective temperature of H_2 may be the result of promoted methanation reactions leading to the higher than average effective temperature for CH_4 which increases in concentration with temperature. Under ATR conditions with water present a wider range of effective component temperatures are observed as shown in Figure 2.14B. Similar comparisons may be made between component effective temperatures under ATR conditions. Pathways producing CO and consuming C_3H_8 are promoted under microwave heating while the effective temperature of CO_2 decreases, indicating differences between microwave and furnace heating. CO_2 's effective temperature decreases

Table 2.4: Catalyst exit temperatures recorded under each operating condition. Uncertainty on values is $\pm 12 - 21$ °C.

Condition	POX °C	ATR °C
Waveguide	550	573
Furnace 350 °C	647	606
Furnace 450 °C	684	632
Furnace 550 °C	726	678

as a result of CO₂ yields declining with increasing microwave power while within the furnace environment CO₂ yield increases with temperature. Greater disagreement among ATR component effective temperatures compared with POX conditions indicate that the microwave heating environment is having a unique effect upon the system.

Within each reaction system an average value of the component effective temperatures was used for subsequent comparison of data. Despite excluding species whose trends with temperature do not match, variance across the species examined led to significant uncertainty in the reported value.

Carbon deposition during reaction under elevated furnace temperature conditions was analyzed for comparison with irradiated samples as shown in Figure 2.15. Irradiated samples are plotted against the estimated effluent temperature shown in Figure 2.14. Carbon deposited under POX conditions displays similar trends between modes of operation, with irradiated samples containing slightly more carbon on average. ATR conditions show a divergence of trends, with furnace samples increasing in carbon content with increasing temperature, while irradiated samples maintain a low quantity of carbon. This would suggest that under ATR conditions the mechanism for maintaining low quantities of carbon is not a bulk thermal, but rather a microwave specific effect.

SEM analysis shows significant nanotube growth under 0 W conditions as shown for ATR experiments in Figure 2.16A. Carbon nanotube quantity visibly decreased with increasing microwave irradiation under POX and ATR. Even under ATR condi-

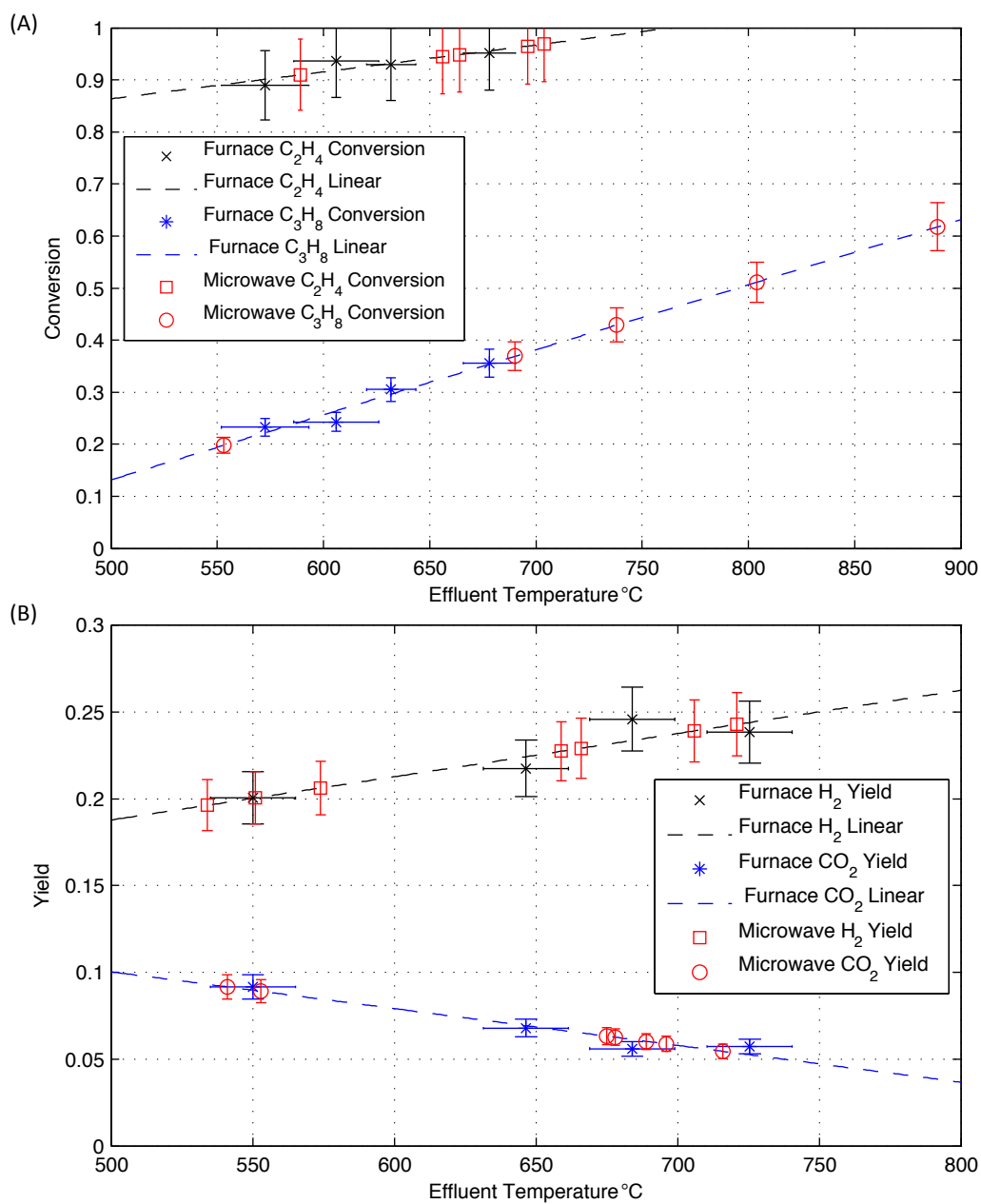


Figure 2.13: Comparison of selected yields and conversions between samples run under microwave conditions and those run under elevated temperatures within a furnace for ATR (A) and POX (B) conditions.

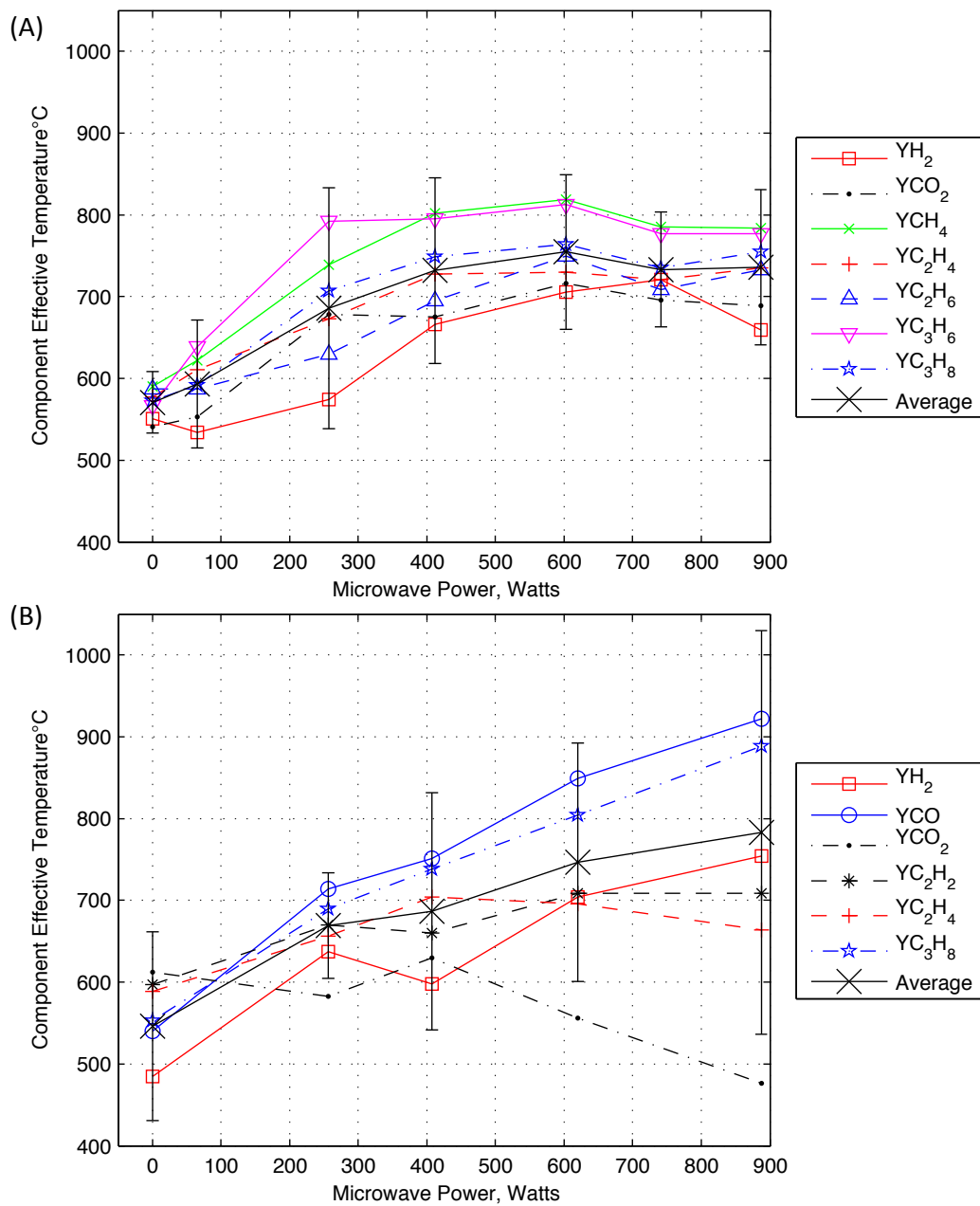


Figure 2.14: Effective component temperatures and average values with 95% confidence intervals for POX (A) and ATR (B) conditions.

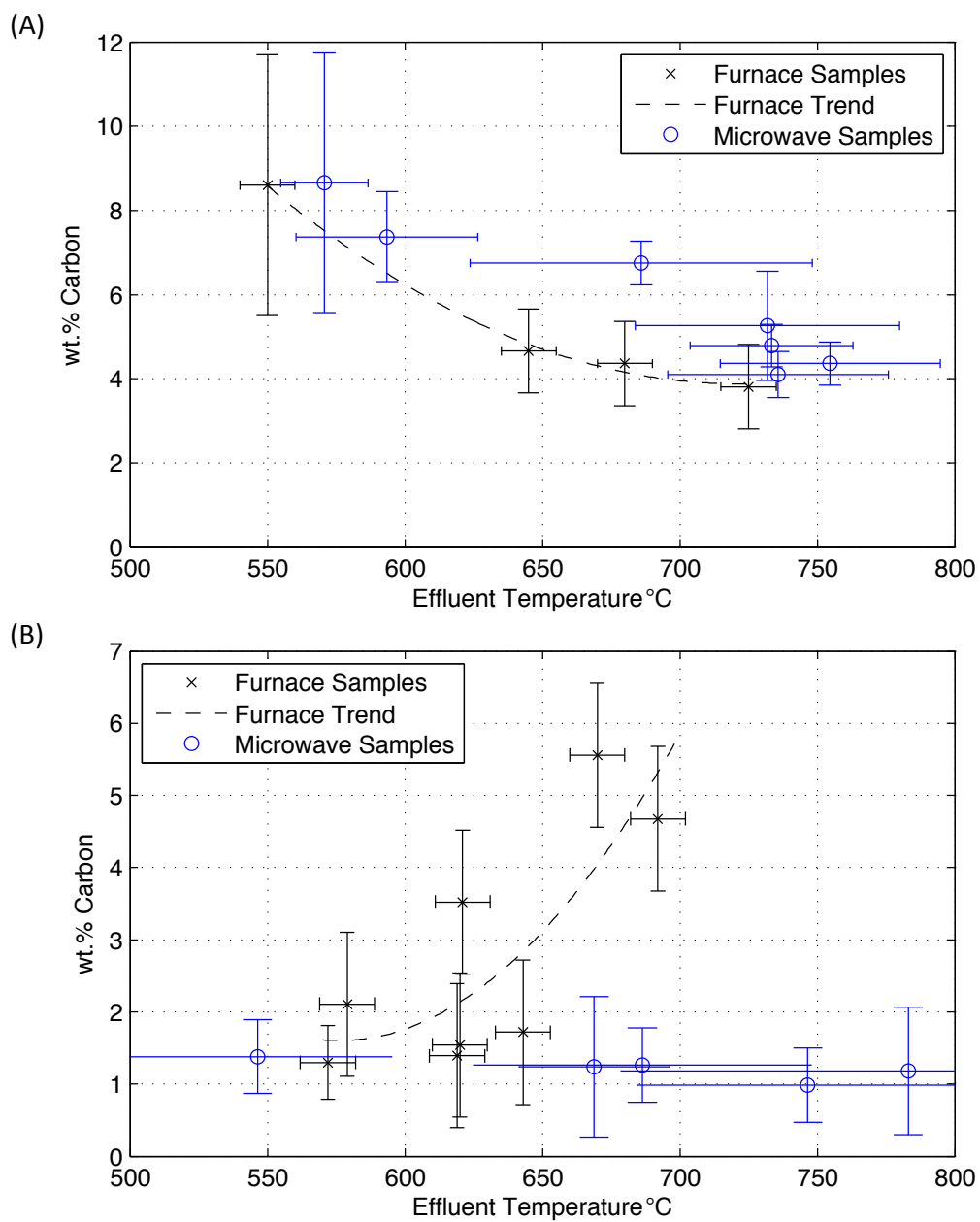


Figure 2.15: Comparison of coking under microwave and furnace heating environments as a function of the estimated and measured effluent temperature for POX (A) and ATR (B) conditions.

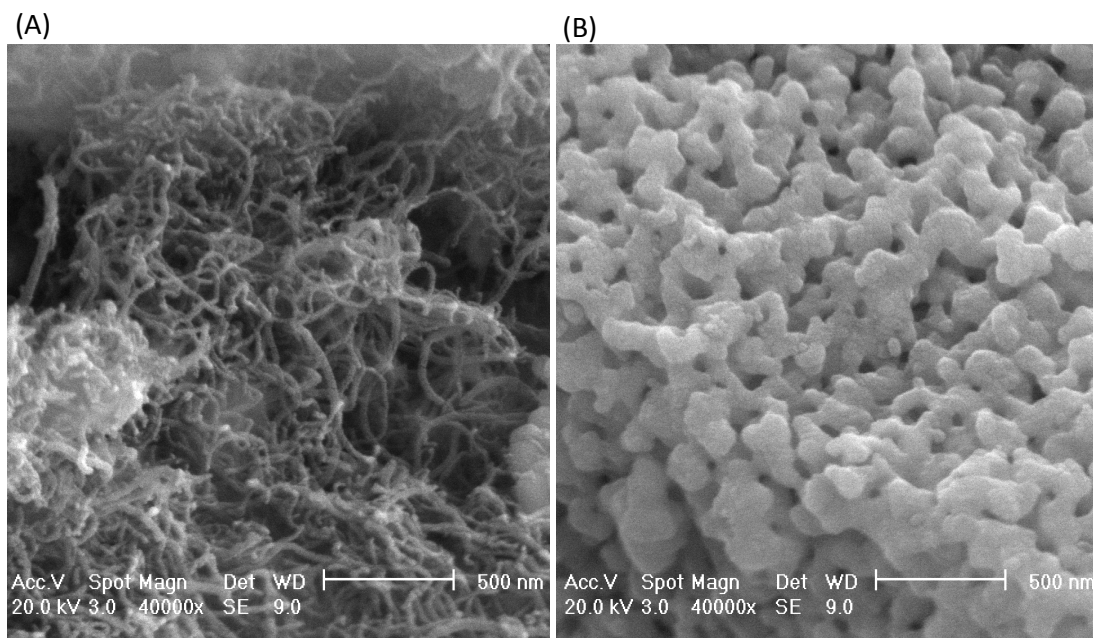


Figure 2.16: SEM micrographs of samples having undergone ATR reaction exposed to 0 W (A) and 900 W (B) of microwave irradiation.

tions where the total quantity of carbon is unchanged, nanotubes were not visible after irradiation, Figure 2.16B. This finding would suggest that microwaves act to prevent of remove bulk carbon nanotubes, but leave behind other forms of coating carbon less apparent in SEM analysis. Samples subject to furnace heating were found to contain significant quantities of carbon nanotubes, highlighting the ability for microwaves to transfer energy into carbon structures leading to their preferential oxidation.

2.4.2 Microwave Specific Effects

Reactions carried out within the furnace have been used as a means to artificially increase the sample temperature for comparison with irradiated samples. Certain species exhibit similar trends under traditional heating and microwave heating. In other instances trends in measured compositions under microwave irradiation depart significantly from trends observed in the furnace, leading to what may be considered

more microwave specific effects. It is significant to note that those species departing furnace trends differ between POX and ATR conditions.

Under POX conditions only CO and C₂H₂ exhibit differing trends between microwave and furnace heating. CO production under microwave irradiation, Figure 2.17A, remains low compared with furnace results. C₂H₂, Figure 2.17B, shows an initial decrease under irradiation before increasing above furnace levels, possibly due to greater thermal cracking within the differentially heated catalyst. The magnitude of variation in these species is small and likely the result of changes in catalyst temperature profile.

ATR irradiated conditions resulted in CO₂, CH₄, C₂H₆ and C₃H₆ departing furnace trends with CO₂ and C₃H₆ shown in Figure 2.17C-D. No CH₄ or C₂H₆ was observed in furnace ATR experiments, however under increasing levels of irradiation, increased cracking led to small levels of each product with peak yields of 0.003. CO₂ yields decreased substantially consistent with the WGS equilibrium at higher temperatures. C₃H₆ yields increase, presumably due to greater dehydrogenation of propane constant with an increase in the downstream catalyst temperature.

In all cases where trends do not match it does not appear that further increases in the furnace temperature would result in the observed microwave yields. As noted, experiments were not able to probe higher temperatures due to pre-combustion. This demonstrates the ability of microwave heating to add energy into the catalyst and not the gas phase, reducing homogeneous combustion. Using microwaves we are able to force the operation of the reformer into regimes not accessible by traditional resistive heating.

Power dissipation within the microwave cavity was monitored by forward and reverse directional couplers to obtain the rate of energy absorption by the sample shown in Figures 2.8D and 2.9D. Power dissipation ranged from 2 - 47 MW m⁻³ with absorption generally increasing with the applied forward power. Samples exposed

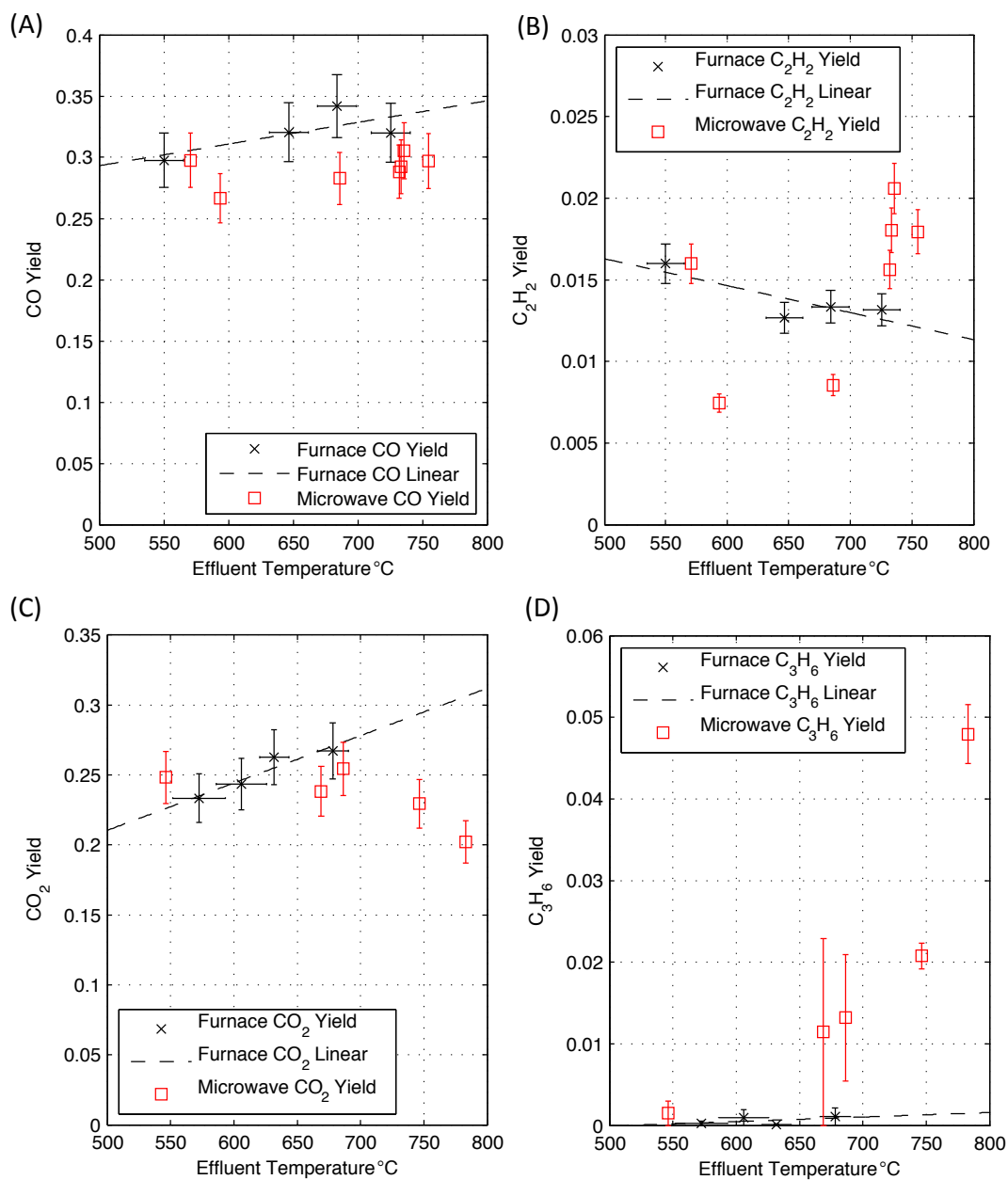


Figure 2.17: Incidences where yields obtained under microwave irradiation do not match those obtained by elevating the sample temperature within a furnace for CO (A) and C₂H₂ (B) under POX conditions and CO₂ (C) and C₃H₆ (D) under ATR conditions. Microwave data is plotted against temperatures determined in yield comparisons.

to POX conditions exhibit a high initial slope in absorbed power before plateauing above 400 W, consistent with product yields and temperature estimations showing a plateau in temperature at high power levels. The POX cases reach a point at which the energy input is balanced by heat removal from the system leading to flat power absorption and no further change in product distributions. ATR cases exhibit a general increase in absorbed power with increasing microwave field that does not trail off. Changes in product distributions are observed across all power levels tested and product based temperature estimation points to a linear increase in temperature with forward power. Within ATR there is the additional energy sink of endothermic steam reforming that allows for additional energy to be dissipated within the catalyst and gives the appearance of higher temperatures when compared with traditionally heated samples.

There exist certain operational constraints that limit the maximum furnace temperature and microwave field strength (applied power) that a catalyst can be exposed to. In the case of furnace experiments, operation at temperatures greater than 550 °C lead to pre-combustion of the feed. Microwave heating of the catalyst is limited by the onset of plasma formation at power levels above 900 W of transmitted power. These two conditions represent the upper limit of operation within this system. Comparison of the effluents at each of these extremes provides insight into the extremes to which the system can be forced under traditional heating and microwave heating environments as well as the differences between these two modes of operation. Rates of product formation and fuel utilization for POX and ATR conditions at the upper limits of furnace temperature and microwave irradiation are shown in Figure 2.18 along with the base-case 0 W rates. A slightly increased rate of H₂ and CO production is observed in the furnace heated POX experiments with little overall variation in the observed rates at each extreme. When compared with the 0 W case a shift is observed from CO₂ to CO production along with additional H₂ formation, with

furnace heating resulting in the greatest syngas production. Operation under ATR conditions demonstrate the potential gains of providing energy by microwaves into a system where the endothermic steam reforming reaction is not fully utilizing the feed components. Comparing the 0 W case to the upper limits of furnace and microwave operation there is a stark increase in H₂ and CO production along with a greater utilization of C₃H₈. Microwave heating in particular is able to increase H₂ and CO production above what is viable in the furnace while decreasing CO₂ production.

2.5 Conclusions

Exposure of reforming catalysts to microwave irradiation during operation under non-ideal operating conditions has been demonstrated as a means to reduce coking and alter product distributions. Experiments under conditions of partial-oxidation and autothermal reforming of a mixed propane/ethylene feed have been used to probe microwave interactions in a plasma-free operating regime. Subsequent experiments were performed with catalysts run at elevated temperature within a furnace to determine which effects can be accounted for by a simple increase in the reaction temperature and those that are microwave heating specific. Early work led to the generation of several University of Michigan technology disclosures and a pending patent described in Appendix B.

POX experiments show little change in total syngas production with increasing levels of irradiation, consistent with the limited availability of oxygen. A substantial increase in cracking and dehydrogenation results in a net increase in ethylene as well as additional propylene and methane formation. Some of the additional methane produced may be the result of methanation of carbon deposits heated by microwaves. Physical and metallic surface area measurements indicate no significant sintering of the support or catalytic materials under POX conditions. Changes in post reaction carbon TPO profiles indicate that microwave radiation is interacting with the carbon

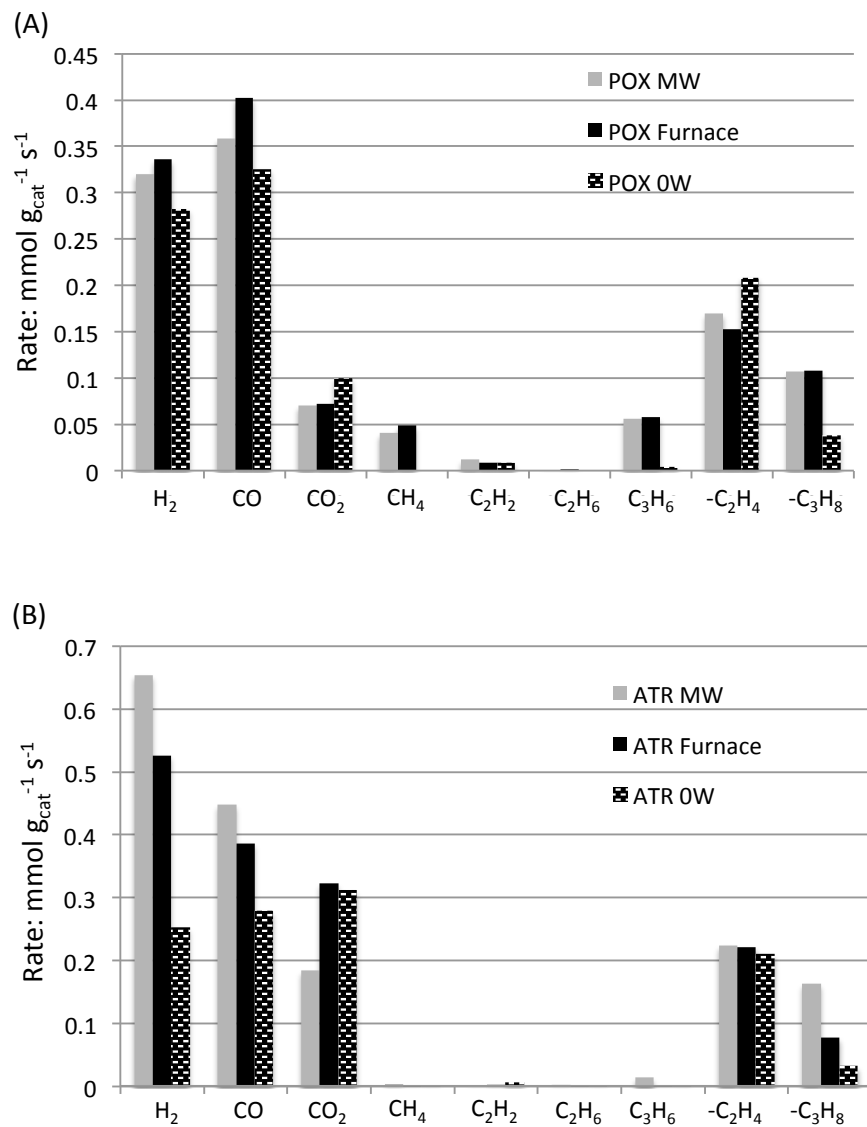


Figure 2.18: Comparison of rates of product formation and fuel consumption obtained under conditions of maximum furnace temperature before pre-combustion [550 °C (Furnace)] and maximum microwave irradiation before onset of plasma formation [900 W (MW)]. Also shown is the base case non irradiated samples run within the microwave waveguide (0W) for POX (A) and ATR (B) systems.

present in such a way as to favor its reaction with the gas phase and subsequently reduce the quantity remaining on the catalyst despite limited supplies of O₂ in the feed. Shifts in TPO peak positions are typical of exposure to higher temperatures and a change to more graphitic or crystalline carbon as confirmed by Raman analysis. Further, the observed decrease in CO₂ may result from its reduction over carbon at high temperatures in addition to increased WGS activity. Based on TPO peak position, power measurement and temperature estimation within the system, it appears that increasing the microwave field above 250 - 400 W does not have a significant benefit to the system. The maximum increase in catalyst temperature was estimated as 170 °C under irradiation.

Introduction of water in ATR experiments demonstrate the capacity of microwaves to introduce energy and drive endothermic reactions, substantially increasing syngas yield. Yields of cracking and dehydrogenation products, small under normal operation, further decrease when irradiated. Physical surface area measurements show no change in the support surface area. The introduction of microwave radiation maintained metallic surface area near initial values while the non-irradiated case saw a 50% decrease in dispersion. Carbon deposition remained low under ATR conditions but was not significantly affected by the introduction of microwaves. All samples contained the same amount of carbon, suggesting that an equilibrium amount of carbon forms under ATR conditions that is not influenced by changes in microwave field strength. Similar to POX conditions, a shift in TPO peak position is observed with little change above 250 W. Temperature within the ATR system appears to increase linearly with applied microwave power up to 900 W. Higher microwave power levels were not used due to the propensity for plasma formation at higher field strengths. The maximum increase in irradiated catalyst temperature was estimated as 220 °C.

Much of the microwave utilization literature attempts to determine the origin of observed changes in the system as being microwave specific or explainable by tradi-

tional heating methods. Trends in carbon deposition and product yields under POX conditions can generally be accounted for by elevated furnace temperature experiments, with the slight exception of CO and C₂H₂. The limited availability of O₂ greatly constrains operation and the absence of H₂O limits the endothermic energy demand in the downstream portion of the catalyst. Increasing the system temperature by microwave or furnace thus have very similar results. Comparison of ATR yields with those obtained under elevated furnace temperature conditions demonstrate a departure of the system from a traditional thermal behavior. Carbon deposition increases substantially with temperature in the furnace while remaining constant on the irradiated catalyst. Conversion of C₃H₈ indicates a much greater use of the feed and increased steam reforming activity when irradiated. CO₂ yield decreases with microwave power, consistent with the WGS equilibrium at high temperatures and possibly due to the CO₂ oxidation of carbon deposits to produce additional CO. C₃H₆ also increases, consistent with increased oxydehydrogenation activity. Volumetric introduction of energy acts to raise the temperature of the downstream end of the catalyst, driving the steam reforming and water-gas shift reactions.

This work has confirmed that microwave frequency radiation can be used to selectively and volumetrically interact with a catalytic reforming system. Carbon was shown to interact in a favorable way, reducing coking under some conditions. Further, the activity of the system was altered to produce effects not observed in traditional thermal cases. The greatest beneficial effects of microwave heating are observed with the introduction of steam, increasing the endothermic energy demand and leading to greater syngas production than achievable by traditional furnace heating.

CHAPTER III

Microwave Effects on Sulfur Poisoned Catalysts

3.1 Introduction

Portable reforming technology for the production of synthesis gas (CO & H₂) from hydrocarbons has the potential to be used in conjunction with fuel-cells, distributed chemical manufacturing, emissions control and engine cold-start technology. In particular, reforming technology has received much attention for its role in the processing of liquid hydrocarbons for portable power generation units. Catalytic reforming of hydrocarbon fuels is frequently plagued by deactivation via carbon deposition and sulfur poisoning. Performance further degrades when catalysts are supplied with non-ideal feed gas compositions.

Previous work has demonstrated the ability of microwave radiation to effect changes in active fuel reforming systems. Chapter II describes the results of studies examining irradiation of partial-oxidation and autothermal reforming systems under conditions of low total oxygen leading to incomplete conversion and coke deposition. Microwave irradiation was found to reduce coking and improve syngas yield when water was present in the system, corresponding to an endothermic energy demand. When only the exothermic partial-oxidation reactions were studied there appeared to be little difference between microwave and furnace heating. The present study seeks to expand the analysis performed in Chapter II to a sulfur poisoned autothermal reforming

system.

Sulfur poisoning is one of the most pervasive modes of heterogeneous catalyst deactivation due to its strong chemisorption to metallic sites. Sulfur is plentiful in many molecular forms within distillate products and can have significant detrimental effects at sub-ppm levels [16]. Catalytic activity is modified by the physical blocking of active sites and diffusion of surface species by adsorbed sulfur as well as the longer range electronic effects that can extend up to 5 a.u. away from the sulfur atom [98, 99, 100, 101, 102]. At high concentrations sulfur can completely poison a catalyst. At low (ppm) sulfur concentrations an equilibrium coverage of sulfur can be established, partially diminishing activity [23, 96].

Several studies have examined the effects of microwave irradiation on sulfur poisoning. Ibe et al. and Fanson et al. have examined the effects of microwave radiation on sulfur adsorbed to a Pt-Ba NO_x storage reduction catalyst [26, 103]. Under microwave irradiation, desorption of sulfur was found to occur at temperatures below 200 °C while it is reported that desorption normally occurs at temperatures above 600 °C. Such a drastic difference in temperatures is likely the result of selective heating of sulfur adsorbing sites and inaccurate temperature measurement in an unevenly heated sample. Similarly, Zhang et al. observed increased conversions in the catalytic reforming of methane with carbon dioxide over Pt, consistent with the formation of hot-spots on the catalyst and the inconsistencies of temperature measurement [69]. Difficulty in measuring temperature and the resulting improper reporting of results is common in literature. Thermodynamics will dictate the lightoff temperature of a reaction on a surface, therefore when studies report lightoff at reduced temperatures under microwave irradiation it is indicative of local hotspots within the sample [70, 71, 66]. These hotspots have been shown to be less prone to poisoning by SO₂ on La_{0.8}Ce_{0.2}MnO₃ perovskite, methane oxidation systems [72].

The present study seeks to determine if microwave heating can be used to influence

sulfur poisoning in active reforming catalysts. Conditions of low total oxygen and high space velocity are used to promote carbon deposition and reduce conversion. Comparisons are drawn between irradiated experiments and experiments run within a traditional furnace heating environment to determine those effects attributable to the microwave heating environment.

3.2 Experimental

3.2.1 Catalyst Preparation

Catalysts used in this study are identical to those described in section 2.2.2 consisting of 10 wt.% Ni supported on $\text{Ce}_{0.75}\text{Zr}_{0.25}\text{O}_2$ (Ni/CZO) with a final washcoat loading of 20 ± 2.4 wt.% on cordierite monolith supports.

3.2.2 Flow Reactor Description

Reforming experiments were carried out using the custom single-mode microwave reactor described in section 2.2.3.

3.2.3 Reaction Conditions

The prepared catalyst was tested for activity in the autothermal reforming of propane under varying levels of irradiation. Sulfur was introduced in the form of thiophene within the water feed to the equivalent of 200 ppmw atomic sulfur in the fuel. Reaction conditions were set such that adiabatic operation would be stable over the time span of experiments with minimal carbon deposition under no-sulfur conditions. Table 3.1 provides relevant information on the experimental conditions used. For each experiment a single monolith, 0.76 ± 0.025 g (1.57 cm³) was loaded into the flow reactor capable of exposing samples to controlled levels of microwave radiation. All tests were repeated with fresh catalysts over reaction periods of 60

Table 3.1: Autothermal reforming with sulfur operating conditions.

GHSV, $\text{cm}^3 \text{cm}^{-3} \text{h}^{-1}$	120,000
GHSV, $\text{cm}^3 \text{g}_{\text{Ni/CZO}}^{-1} \text{h}^{-1}$	1,178,000
O/C	0.75
H ₂ O/C	0.25
Air Flow, mmol min^{-1}	103.9
Propane, mmol min^{-1}	20.7
Water, mmol min^{-1}	15.6
Thiophene (when present) mmol min^{-1}	0.077

minutes during which steady state was achieved. Data shown is the average of multiple trials.

3.2.4 Reactor Startup and Shutdown

Pre-reduced monoliths were loaded into the reactor, blanketed by N₂, and the furnace ramped to 600 °C to achieve a catalyst pre-heat temperature of 300 °C within the microwave cavity. Lightoff is initiated using a two stage process to simultaneously raise the catalyst temperature while maintaining a rich mixture outside of the upper flammability limit. First, H₂ (53.6 mmol min^{-1}) is combusted with air (14.3 mmol min^{-1}) for 2 minutes, raising the catalyst temperature to ~ 480 °C. C₃H₈ (20.7 mmol min^{-1}), is brought on stream and several seconds later the flow rate of air is increased to the reaction conditions (103.9 mmol min^{-1}) and the flow of hydrogen ceased. Water flow is initiated with or without thiophene dissolved according to the needs of the experiment. Startup under net-reducing conditions ensures that the catalyst is reduced at experiment initiation. Reactions are extinguished under N₂ to preserve the state of the catalyst and are cooled to room temperature before removal. Monoliths are bisected for observation, crushed and mixed for analysis to ensure uniform sampling.

3.2.5 Analysis of Reforming Behavior

Reactions were monitored for selectivity and activity under the prescribed conditions. Reactor effluent passes through a 0 °C trap to remove water before sampling by a Mass Spectrometer (Ametek Dycor Proline) scanning an m/z range of 1 - 50. Calibration was performed using multiple calibration gas standards to determine relative ionization intensities around the concentrations of interest. Calibration data was combined with electron ionization data from the NIST Chemistry Database in an adaptive mass spectrum deconvolution program in order to track the concentrations of: H₂, H₂O, O₂, N₂, CH₄, C₂H₂, C₂H₄, C₂H₆, C₃H₆, C₃H₈, CO, CO₂, and Ar. Due to the removal of water from the effluent, quantification of water produced or consumed in the reaction was not possible. Total effluent flow is calculated using N₂ as an internal standard. Yields and conversions are calculated on a molar basis according to Equations (3.1) to (3.11). Due to the low amount of O₂ and H₂O supplied, reactions 1.1 to 1.3 are severely stoichiometrically limited leading to the formation of

many intermediate cracking and dehydrogenation products.

$$Y_{H_2} = \frac{F_{H_2,out}}{4 \times F_{C_3H_8,in} + 2 \times F_{C_2H_4,in}} \quad (3.1)$$

$$Y_{CO} = \frac{F_{CO,out}}{3 \times F_{C_3H_8,in} + 2 \times F_{C_2H_4,in}} \quad (3.2)$$

$$Y_{sg} = \frac{F_{H_2,out} + F_{CO,out}}{7 \times F_{C_3H_8,in} + 4 \times F_{C_2H_4,in}} \quad (3.3)$$

$$Y_{CO_2} = \frac{F_{CO_2,out}}{3 \times F_{C_3H_8,in} + 2 \times F_{C_2H_4,in}} \quad (3.4)$$

$$Y_{CH_4} = \frac{F_{CH_4,out}}{3 \times F_{C_3H_8,in} + 2 \times F_{C_2H_4,in}} \quad (3.5)$$

$$Y_{C_2H_2} = \frac{2 \times F_{C_2H_2,out}}{3 \times F_{C_3H_8,in} + 2 \times F_{C_2H_4,in}} \quad (3.6)$$

$$Y_{C_2H_4} = \frac{2 \times F_{C_2H_4,out}}{3 \times F_{C_3H_8,in} + 2 \times F_{C_2H_4,in}} \quad (3.7)$$

$$Y_{C_2H_6} = \frac{2 \times F_{C_2H_6,out}}{3 \times F_{C_3H_8,in} + 2 \times F_{C_2H_4,in}} \quad (3.8)$$

$$Y_{C_3H_6} = \frac{3 \times F_{C_3H_6,out}}{3 \times F_{C_3H_8,in} + 2 \times F_{C_2H_4,in}} \quad (3.9)$$

$$Y_{C_3H_8} = \frac{3 \times F_{C_3H_8,out}}{3 \times F_{C_3H_8,in} + 2 \times F_{C_2H_4,in}} \quad (3.10)$$

$$X_{C_3H_8} = 1 - \frac{F_{C_3H_8,out}}{F_{C_3H_8,in}} \quad (3.11)$$

3.2.6 Catalyst Characterization

Samples were characterized by single-point BET N₂ physisorption on a Quantachrome ChemBET instrument to obtain measurements of physical surface area. Metallic surface area and dispersion measurements were performed by H₂ chemisorption using a Micromeritics ASAP 2020 instrument. Samples were degassed under vacuum at 300 °C, followed by reduction in flowing H₂ at 600 °C. Measurements were taken at 35 °C, obtaining two complete isotherms to determine the quantity of strongly adsorbed hydrogen, thereby calculating the number of exposed metallic sites.

Temperature programmed oxidation (TPO) was performed gravimetrically using

a TA instruments Q500. Samples were initially heated to 120 °C to remove adsorbed water before ramping at 7.5 °C min⁻¹ to 850 °C in 60 sccm of air with a balance purge of 40 sccm N₂. TPO is used as a means to observe and quantify carbon deposits.

Scanning electron microscopy (SEM) was employed to observe carbon morphologies using a Philips XL30FEG SEM instrument.

3.3 Results

Syngas yield as a function of time for samples exposed to varying levels of microwave irradiation are plotted in Figure 3.1. Experiments are initiated under excess H₂ resulting in initial yields greater than unity. Introduction of sulfur in the form of thiophene was found to immediately decrease syngas yield by more than 45%, providing steady operation consistent with reaching an equilibrium coverage of sulfur and the transformation of thiophene into H₂S [104]. Each condition tested reached a steady state value within approximately 20 minutes of lightoff with only slight trending in yields. Data was averaged over the 20 - 60 minute period to provide steady state values. Introduction of thiophene coincided with a significant increase in exit gas temperature as measured by a thermocouple placed directly below the catalyst within a quartz thermowell. Steady state effluent temperatures increased from 640 °C (sulfur free) to 700 °C (with sulfur), consistent with blocking of steam reforming sites.

Introduction of microwave radiation to the catalyst improved syngas production substantially, however full recovery of syngas production is not achieved and there was little added benefit above 200 W of irradiation. Experiments in which the microwave power was turned on and off over several minute periods showed no lasting changes to the product distributions once the microwave system was turned off. Syngas yield immediately returns to the 0 W sulfur poisoned value suggesting that either any sulfur removed from the surface by microwave heating immediately re-adsorbs, or more likely, that sulfur poisoning is unchanged under microwave irradiation and the

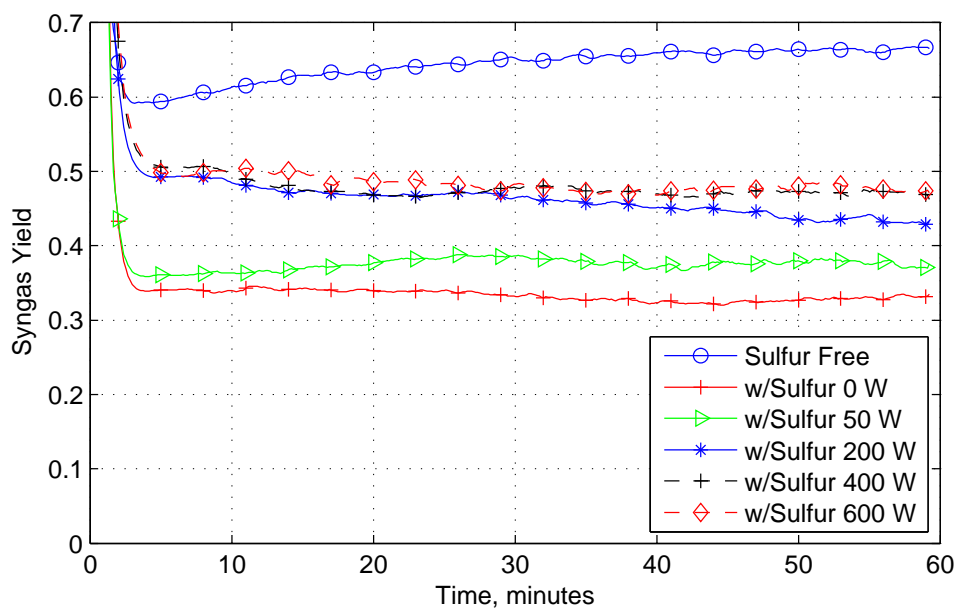


Figure 3.1: Syngas yield versus time for sulfur free and sulfur containing experiments exposed to 200 ppmw atomic sulfur in the form of thiophene while exposed to the specified intensities of microwave irradiation.

change in products is the result of volumetric catalyst heating.

In addition to a decrease in syngas yield, yields of most species are altered with the introduction of sulfur as shown in Figure 3.2. Circled data points are sulfur-free with the remainder of experiments having been carried out with thiophene present. Sulfur causes a drop in CO and H₂ yields while increasing production of CO₂, CH₄, C₂H₄ and C₃H₆. Poisoning of the active sites is sufficient to allow for O₂ slip. Introduction of microwave irradiation drives the system yields toward the no-sulfur case, decreasing dehydrogenation and cracking products, while increasing syngas production and water-gas shift activity. Power absorbed by the sample, Figure 3.2D, trends with syngas production with a high initial slope leading to a plateau above 200 W.

Due to the relatively long duration of the sulfur containing experiments there is an increased propensity for the formation of plasmas at high electric field strengths. Plasma formation was observed in several experiments of greater than 600 W forward power. The onset of plasma generation was preceded by a drop in the reflected power,

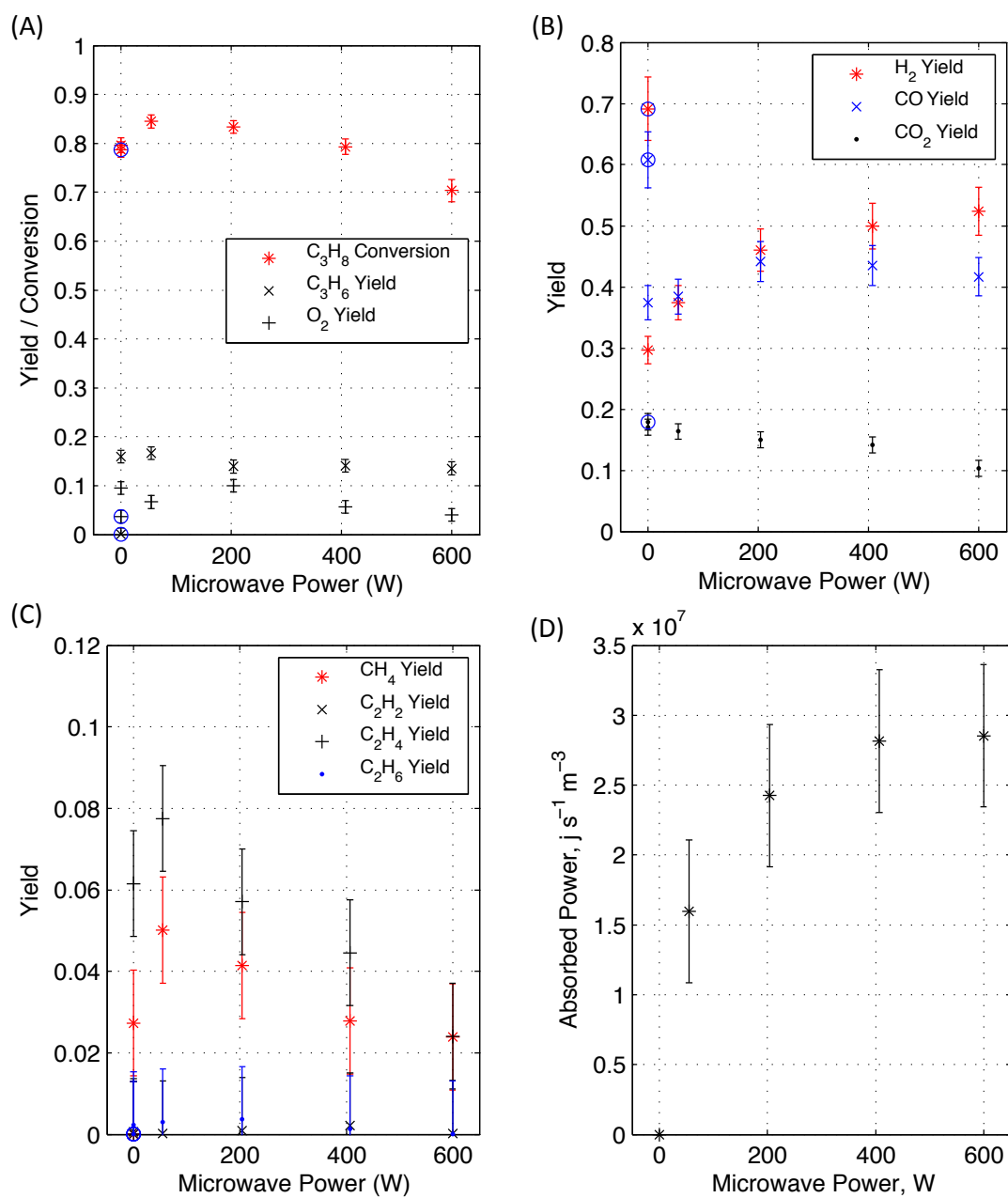


Figure 3.2: ATR w/S Results: Conversion & Yields (A-C), Power absorbed by the catalyst as a function of the applied forward power (D). Circled data points are sulfur free, all others are with sulfur present.

and a net increase in absorbed power. Once a plasma is established, there exists a continued elevation of energy dissipation within the reaction tube, coinciding with an increase in syngas yield. Any experimental case in which plasma generation was observed was excluded from this analysis.

3.4 Discussion

3.4.1 Furnace Temperature Comparison

To gain insight into the temperature environment experienced by a sulfur poisoned reforming system operating under microwave irradiation, product distributions were compared with those obtained by increasing the system temperature using a furnace. Furnace temperature comparisons allow for the determination of those observed trends attributable to furnace reproducible thermal effects and those effects unique to the microwave heating environment.

Sample temperatures are increased by placing catalysts within the furnace and increasing the set-point temperature above the standard pre-heat temperature of the microwave waveguide. Within the furnace, the catalyst containing section of quartz tubing is wrapped in quartz-wool to prevent the formation of hot spots due to radiation from the furnace heating coils. The catalysts are subsequently run under standard operating conditions while monitoring the effluent concentrations and temperature, from which a comparison can be made with compositions obtained under microwave conditions. Furnace yields are plotted as a function of exit temperature as measured by a thermocouple placed within a thermowell directly below the catalyst in the center of the reaction tube. An extrapolation of the trend observed in the furnace data is then used to match with microwave data as shown in Figure 3.3. In certain instances the microwave data fits the trends observed under traditional heating quite well, this behavior may be considered traditional thermal effects. Species

exhibiting similar microwave and furnace trends included H_2 , CO and CO_2 . Effective temperatures for H_2 , CO and CO_2 along with the mean effective effluent temperature are provided in Figure 3.3. Catalyst temperatures are estimated to increase by over $200\text{ }^\circ\text{C}$ under irradiation with yields of CO indicating a significant increase in the temperature associated with pathways leading to its production. Yield-estimated temperatures agree in trend with measured power absorption by the catalyst and obey the rank order expected of increasing temperature with irradiation level. Disagreement among H_2 , CO and CO_2 effective temperatures and the lack of matching hydrocarbon data suggests that irradiation of the catalyst results in very different temperature profiles than those observed in a furnace.

In some instances the measured compositions under microwave irradiation depart significantly from the expected trend observed in the furnace, leading to what may be considered microwave specific effects. CH_4 , C_2H_4 , C_3H_6 and C_3H_8 all exhibit behavior not consistent with furnace obtained yields as shown in Figure 3.4 when the microwave data is plotted using the average component effective temperature. Conversion of C_3H_8 decreases at higher effective temperatures (microwave power), while furnace heated samples display the opposite trend, increasing C_3H_8 conversion with temperature. Similarly, yields of CH_4 , C_2H_4 and C_3H_6 decline when irradiated, but increase with furnace heating.

Irradiation of a catalyst and increasing the external furnace temperature both transfer energy into the catalyst, however it appears that the way in which energy is introduced has a drastic influence on cracking and dehydrogenation products. Within a furnace heated environment, energy is transferred at high temperatures from the reaction tube to the gas before entering the catalyst, and it is the gas phase that heats the catalyst. Because the front face of the catalyst is already the hottest part of the system, introducing additional energy in this region results in additional cracking and dehydrogenation as demonstrated by the furnace data in Figure 3.4. While the front

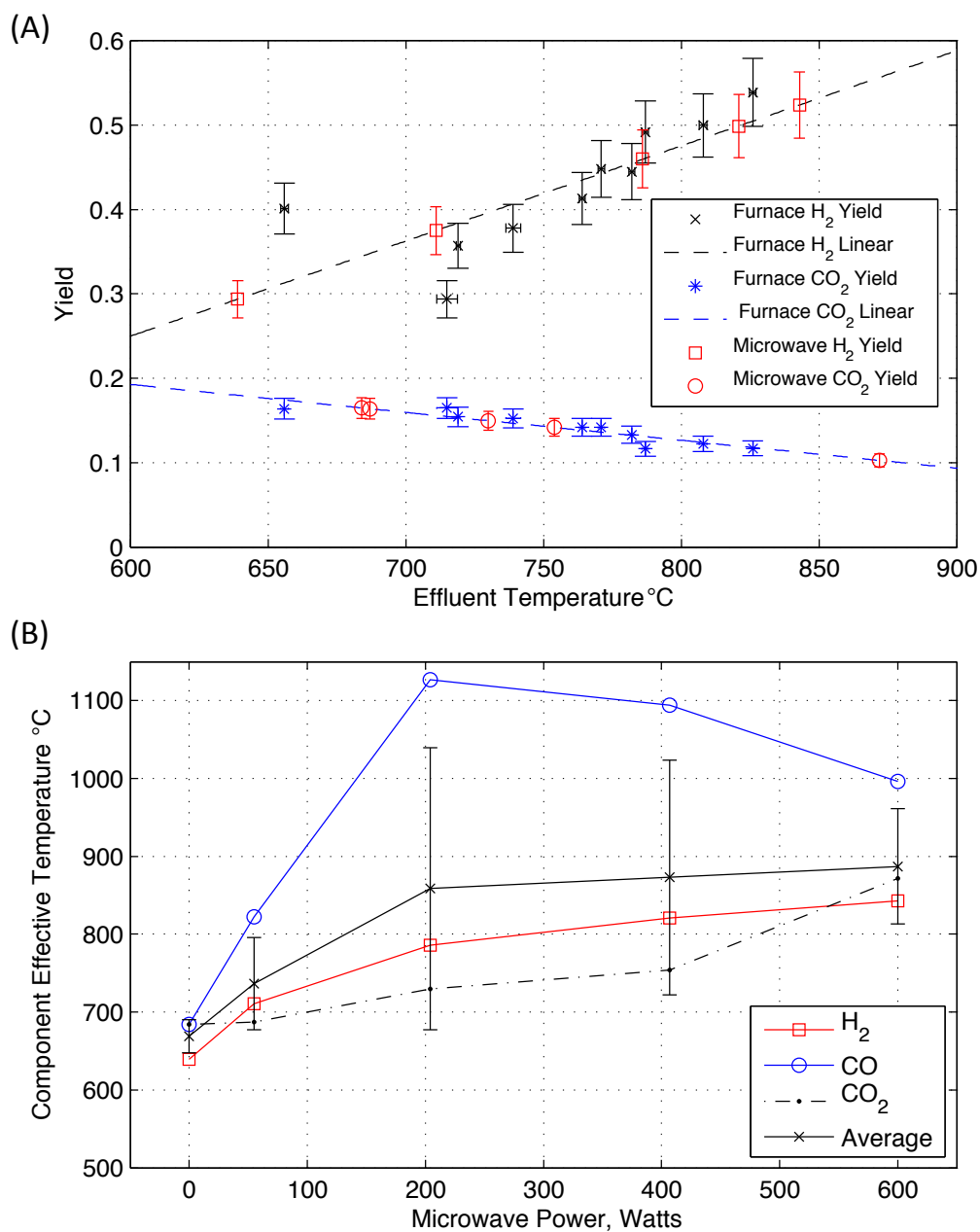


Figure 3.3: (A) Comparison of yields obtained by traditional furnace heating as a function of the catalyst exit temperature used to find effective temperatures for H₂ and CO₂. (B) Effective component temperature and average value with 95% confidence intervals.

face of the catalyst is heated by the incoming gas, the downstream portion of the catalyst is still heat transfer limited and the endothermic steam reforming reaction is limited by the supply of energy brought in by the gas phase. Microwave heating occurs volumetrically within the catalytic washcoat and thus the gas phase is not heated until entering the catalyst. The front face of the catalyst does not experience a significant temperature increase under microwave irradiation, however the combination of volumetric energy addition and convective heat transport down the length of the catalyst acts to raise the temperature of the downstream section of catalyst. By supplying energy to the rear of the catalyst, greater steam reforming activity is observed as evidenced by high H_2 coinciding with fewer cracking and dehydrogenation products exiting the reactor and a drop in C_3H_8 conversion as those sites not poisoned by sulfur preferentially react with the more reactive species present.

Visual inspection of the spent catalyst revealed a marked difference between the various conditions tested. Compared with samples exposed to a sulfur-free feed, those exposed to sulfur exhibited a lighter outer color typical of a more oxidized state as well as more carbon on the interior of the catalyst constant with coking due to the higher temperatures of operation. Catalysts exposed to microwaves retain the darker, more reduced look of the no-sulfur system along with no visible carbon deposition. Images of carbon on the spent catalyst post reduction are provided in Figure 3.5 highlighting the difference in carbon deposition with exposure to sulfur and microwave irradiation. Irradiated catalysts have an appearance more similar to the no-sulfur case than the non-irradiated sulfur samples.

Carbon deposition for irradiated and elevated furnace temperature systems are shown in Figure 3.6. The no-sulfur case is provided for reference with the increase in effluent temperature apparent as the 0 W temperature increases to 700 °C. Introduction of sulfur causes a significant increase in sample weight, attributable to carbon deposition. Irradiation at all power levels tested resulted in the complete removal of

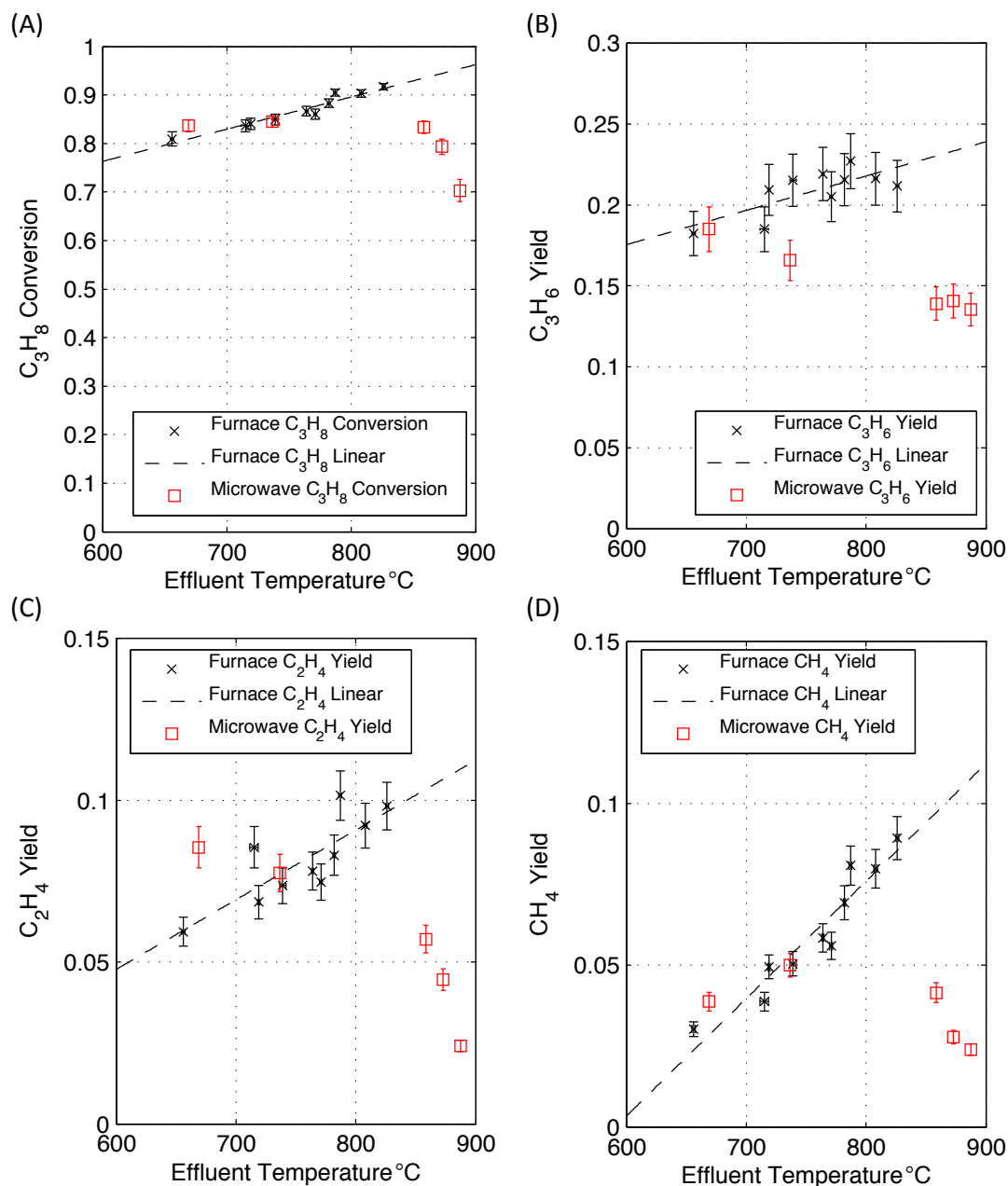


Figure 3.4: Comparison of trends in effluent concentrations within the elevated temperature environment of a furnace and irradiated samples within the microwave waveguide. Data is plotted as a function of the measured effluent temperature for furnace data and the average effective temperature for microwave data. Displayed are (A) C_3H_8 conversion, (B) C_3H_6 yield, (C) C_2H_4 yield, (D) CH_4 yield.

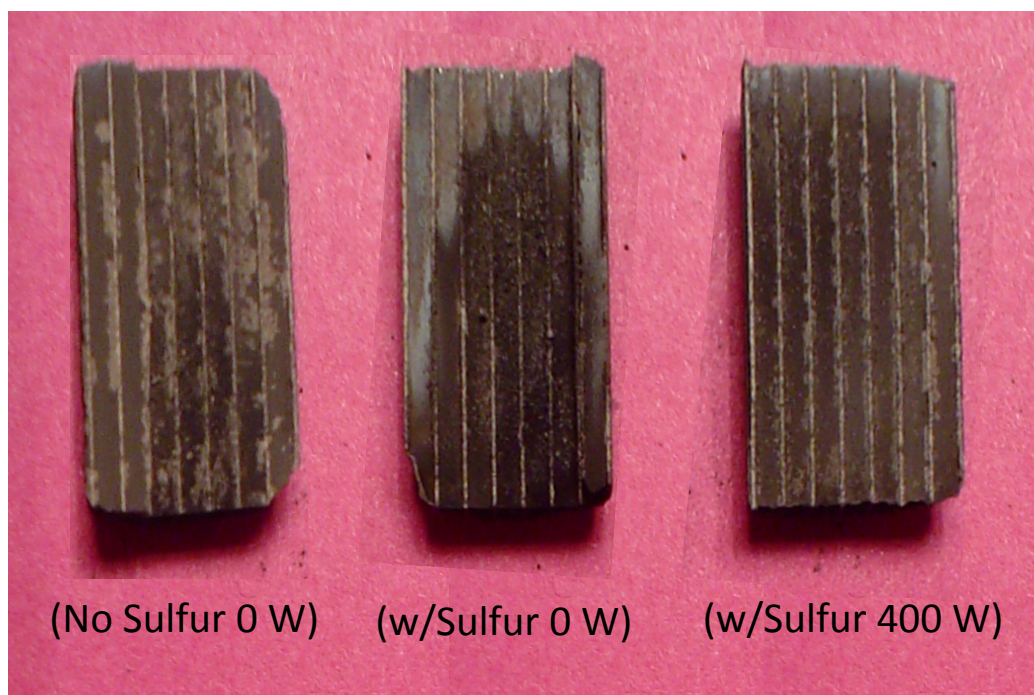


Figure 3.5: Bisected catalysts post reduction in H_2 at $600\text{ }^\circ\text{C}$.

carbon, confirmed by the absence of a carbon peak in TPO. Samples run within the furnace exhibit a significant degree of coking at high temperatures, consistent with an increased generation of carbon precursors within the upstream portion of the catalyst and subsequent coke deposition downstream.

Operational constraints limit the maximum furnace temperature and microwave field strength (applied power) that a catalyst can be exposed to. In the case of furnace experiments, operation of the furnace at temperatures greater than $550\text{ }^\circ\text{C}$ lead to pre-combustion of the feed. Microwave heating of the catalyst is limited by the onset of plasma formation at power levels above 600 W . These two conditions represent the upper limit of operation within this system. Comparison of the effluents at each of these extremes provides insight into the extremes to which the system can be forced under traditional heating and microwave heating environments as well as the differences between the two modes of operation. Rates of product formation and fuel utilization for sulfur poisoned systems at the upper limits of furnace temperature and

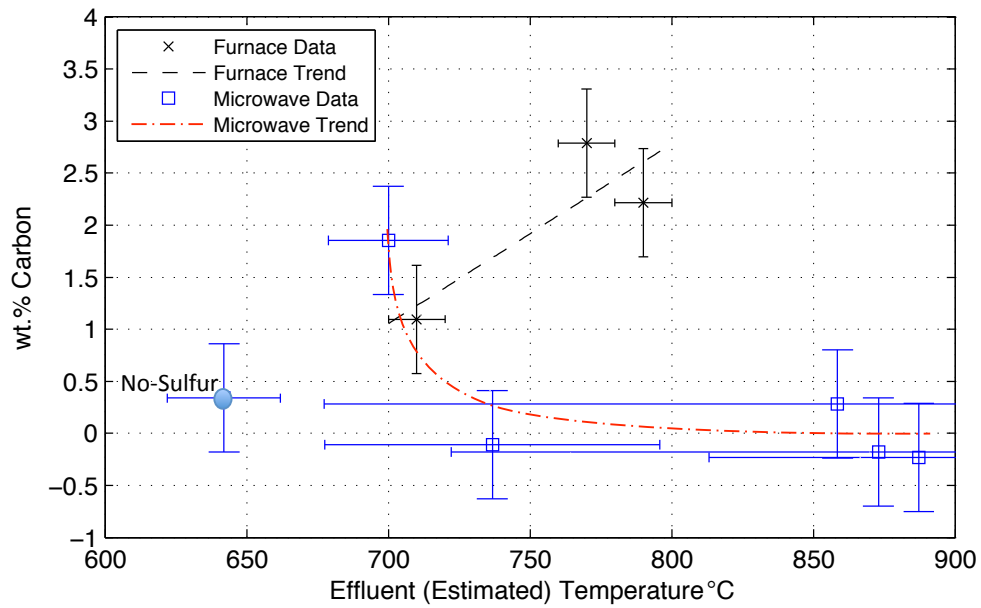


Figure 3.6: Carbon present on catalysts post 60 minutes of reaction as a function of the measured effluent temperature for furnace data and the average effective temperature for microwave data points.

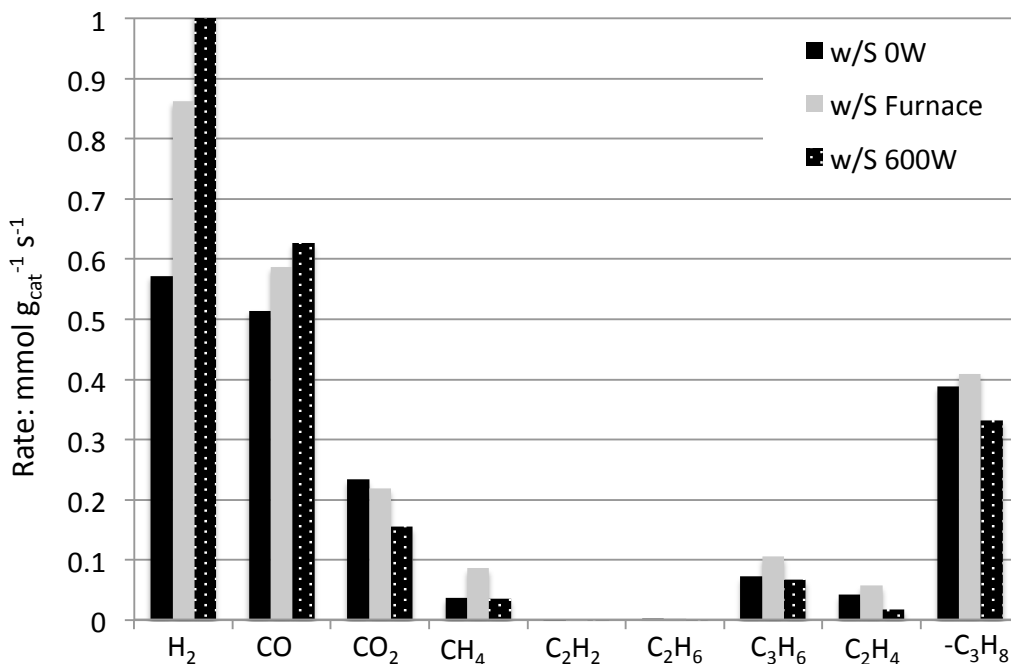


Figure 3.7: Comparison of rates of product formation and fuel consumption obtained under conditions of maximum furnace temperature, 550 °C (Furnace) before pre-combustion and maximum microwave irradiation, 600 W (Microwave) before onset of plasma formation along with base case non irradiated samples (0W).

microwave irradiation are shown in Figure 3.7 along with the base-case 0 W rates. Comparing the 0 W case to the upper limits of furnace and microwave operation shows there is a stark increase in H₂ and CO production along with a greater utilization of C₃H₈. Microwave heating, in particular, is able to increase H₂ and CO production above what is viable in the furnace while decreasing CO₂ production.

3.5 Conclusions

Autothermal reforming of C₃H₈ at an O/C ratio of 0.75 and H₂O/C ratio of 0.25 is highly susceptible to poisoning by 200 ppmw atomic sulfur in the form of thiophene. Introduction of thiophene greatly reduces steam reforming activity, allowing passage of cracking and dehydrogenation intermediates produced within the entrance

region of the catalyst and reducing syngas yield by over 45%. Performance does not further degrade over time indicating that an equilibrium coverage of sulfur is quickly established. Irradiation of a sulfur poisoned catalyst reduces the observed cracking and dehydrogenation products in the effluent while increasing syngas production. Exposure to microwave radiation does not appear to reverse poisoning, rather the volumetric introduction of energy into the downstream portion of the catalyst acts to promote the steam reforming and water-gas shift reactions.

Experiments were undertaken to expose reforming catalysts to elevated temperatures within a furnace heated environment for comparison with microwave irradiated systems. Comparison of furnace and microwave heating environments show significant differences between these two modes of operation. Within the furnace, yields of cracking and dehydrogenation products were observed to increase with temperature. When irradiated, yields of those same products decrease substantially at progressively higher microwave power levels. At the highest power levels tested, conversion of propane decreases, however H₂ production increases slightly, offsetting a decrease in CO production to maintain steady syngas yield. Results obtained from irradiation of active reforming catalysts point to an increase in steam reforming activity over furnace heated samples, with fewer cracking and dehydrogenation products observed.

Comparison of carbon deposited while reforming in microwave and furnace heated environments demonstrates a clear advantage of microwave heating. Carbon couples strongly to the electro-magnetic field, heating and leading to its preferential oxidation as it forms and reduced carbon deposition. Samples exposed to elevated furnace temperatures coke significantly more as the temperature is increased due to greater production of coke precursors in the catalyst entrance region.

Microwaves have been shown to favorably interact with an active hydrocarbon reforming catalyst experiencing reduced syngas production due to sulfur poisoning. Carbon and coke deposition is eliminated and significant gains in syngas production

are observed when irradiated. Volumetric heating of the catalyst increases steam reforming rates without additional coke precursor generation due to excessive entrance region temperatures experienced under elevated furnace temperature environments. Volumetric heating appears most suited to applications with large endothermic energy requirements in structured catalysts where heat transfer limitations in the cool downstream region of the catalyst result in slow kinetics. Microwave heating may be a viable alternative to inter-stage heating in a variety of endothermic reactions.

CHAPTER IV

Determination of Temperature Within an Active Reforming Catalyst Subject to Microwave Radiation

4.1 Introduction

Use of microwave band irradiation as a means to achieve faster and more efficient chemical transformation has received renewed attention in the literature [105, 56, 106]. Within many areas of polymer science and organic chemistry, significant enhancements in the rate of reaction and/or the quality of the final product have been observed. Metaxas outlines many of the advantages of microwave heating including rapid heat transfer, volumetric and selective heating, uniformity of heating, faster throughputs, superior moisture leveling compared with conventional heating, fast switching on and off, a clean environment free of combustion products, compact equipment, high power densities, low maintenance and service costs, as well as energy absorption enhancements by catalysts and agents [59, 52]. While many of these advantages are system specific, they are in contrast to the poor heat transfer in many traditional heating applications.

Numerous studies have proposed unique abilities of microwaves to influence chemical reactions in ways not easily explainable by simple heating models. A major chal-

lenge when comparing microwave heating with more traditional heat transfer modes (conduction, convection, thermal-radiation) is the lack of consistent temperature measurement in microwave fields. Understanding the temperature experienced by an irradiated sample is paramount to understanding the changes observed in the final product. In particular, the determination of temperature becomes very challenging when the sample of interest is at a high temperature and contains large temperature gradients. The challenge of fully understanding the temperature environment within a microwave reactor has contributed to its limited adoption in large scale chemical processes.

The most common modes of temperature measurement within a microwave field are the thermocouple, optical pyrometer and fiberoptic pyrometer. Past work has examined the benefits and drawbacks of each of these methods [107, 108]. The present work examines alternatives to these methods for estimating temperature within a high-temperature reacting system. The microwave assisted reforming of a hydrocarbon mixture will be used to demonstrate these alternate methods of tracking temperature within an electromagnetic field. Catalytic reforming is used in the production of synthesis gas (CO & H₂) from hydrocarbon fuels. Local reaction temperatures can exceed 800 °C with significant temperature gradients from the hot face of the catalyst to the cooler exit region. Irradiation of a catalyst can further alter the temperature profile, making the accuracy of any localized temperature measurement tenuous at best.

Within the body of this work, operation at high temperatures within a system of complex geometries prevented the accurate use of thermocouple or infrared temperature measurement devices. Information on the temperature of a catalytic system is essential to understand its operation and to correctly predict behavior. The following work was undertaken to gain an understanding of the magnitude to which catalyst samples heat under microwave irradiation. Topics addressed will include the

estimation of catalyst temperature change by:

- Thermocouple
- Infrared temperature measurement
- Comparison of effluent with equilibrium calculated compositions
- Comparison of irradiated samples to those run under elevated furnace temperatures
- Changes in carbon oxidation features
- Use of the water-gas shift equilibrium
- System modeling and model-data comparison

Finally, a summary of the methods used in determining the temperature rise experienced by an irradiated catalyst will be presented with suggestions for alternate strategies.

4.2 Materials and Methods

Hydrocarbon reforming experiments were carried out using a custom single-mode microwave reactor consisting of a vertical Carbolyte clamshell furnace mounted above the sample chamber of a microwave waveguide (Gerling Applied Engineering Inc. 2.45 GHz 1.8 kW Continuous-wave), as described in section 2.2.3. Temperature measurements were taken using type-K thermocouples positioned 3 mm below the center of the catalyst when the microwave was not in use. An optical IR temperature sensor (Raytek TX) is employed to measure the external temperature of the catalyst and was calibrated to the sample emissivity before use. The system is controlled via a Programmable Logic Controller (Eaton ELC-PLC) slaved to a computer using a graphical user interface within Matlab[®] to handle data acquisition and control.

Table 4.1: Operating Conditions for POX and ATR experiments.

	POX	ATR
GHSV	65,000	86,762
O/C	0.47	0.47
H ₂ O/C	0.0	0.5
Air Flow, mmol min ⁻¹	56.4	56.4
Propane, mmol min ⁻¹	10.1	10.1
Ethylene, mmol min ⁻¹	10.1	10.1
Water, mmol min ⁻¹	0.0	25.6

Catalysts used in this study consist of cordierite honeycomb monoliths (Dow Corning 400 cpsi 6 mil) washcoated with material consisting of 10 wt.% Ni supported on Ce_{0.75}Zr_{0.25}O₂ (Ni/CZO) to a final washcoat loading of 20 ± 2.4 wt.% as described in section 2.2.2. Prepared catalysts were tested under conditions of partial oxidation, and autothermal reforming, for activity in reforming of a propane-ethylene mixture under varying levels of irradiation. Table 4.1 describes the experimental conditions studied, henceforth referred to as the POX and ATR conditions. For each experiment, a single monolith 0.76 ± 0.025 g (1.57 cm³) was loaded into the flow reactor capable of exposing samples to controlled levels of microwave radiation (0 - 900 watts). All tests were performed a minimum of three times with fresh catalysts over reaction periods of 15 minutes.

Pre-reduced monoliths were loaded into the reactor, blanketed by N₂, and the furnace ramped to 600 °C to achieve a catalyst pre-heat temperature of 250 °C within the microwave waveguide. Light-off is initiated using a three stage process to simultaneously raise the catalyst temperature while maintaining a rich mixture outside of the upper flammability limit as described in section 2.2.5. Startup under net-reducing conditions ensures that the nickel is reduced when experiments begin. At the end of the reaction period, reactions are extinguished under N₂ to preserve the state of the catalyst. The catalyst is cooled to room temperature before removal. Monoliths are bisected for observation, crushed and mixed for analysis to ensure uniform sampling.

Reactions were monitored for selectivity and activity under the prescribed conditions, simulating short-term deleterious operation of a reformer. Pseudo steady state conditions are established within the first few minutes with the subsequent concentration information used for analysis. Species concentrations are determined by online mass spectrometer as described in section 2.2.6. Yields and conversions are calculated on a molar basis according to Equations (2.1) to (2.12).

4.3 Discussion

The following sections present various means that may be employed in temperature determination within an electromagnetic field and the benefits and drawbacks of each. Finally a summary of the temperature methods is presented with respective error analysis.

4.3.1 Thermocouples

Measurement of temperature within electromagnetic fields by thermocouple presents a particular challenge as the mere introduction of a metallic conductor alters the electric and magnetic field distributions and thus the local heating rates. Constraints upon the placement of thermocouples, including the need to have a conducting sheath that is grounded to the cavity wall, and orientation of the probe perpendicular to the electromagnetic field, make their use impractical in many settings. Within high E field environments, sheath heating may be observed and arcing can result between the sample and thermocouple leading to increased plasma formation at high temperatures where dielectric breakdown is more likely to occur. Within this system, placement of a thermocouple directly below the sample position in the microwave cavity was considered, however grounding to the cavity wall was impractical due to the geometries involved.

4.3.2 Infrared Emission

Alternatives to thermocouple temperature measurement include mostly non-contact variations on Infrared (IR) temperature measurement devices. In low temperature operation ($T < 200\text{ }^{\circ}\text{C}$), fiber optic probes with fluorescing coatings may be used. High temperature systems generally use lenses to focus IR light onto a sensor and observe specific wavelength intensities based on the desired temperature range. For high temperature reactions in electromagnetic fields, sapphire light pipes may be used for contact or near contact operations, however they are only able to measure external temperatures within monolith supported catalysts. In this application, a non-contact focused infrared pyrometer was used to observe the side of the catalyst with a focal area of 31 mm^2 . Prior to reaction, the IR system was calibrated to the emissivity of the sample. Use of an IR pyrometer permits observation of the external sample temperature, however this is not a representative measurement for the whole sample as heat losses and deactivation along the outer edge may lead to an erroneously low value. Variation of greater than $\pm 50\text{ }^{\circ}\text{C}$ in the measured IR value across repeats of some experiments led to its limited use as a temperature sensor. Figure 4.1 shows the measured temperatures for POX and ATR conditions as a function of the microwave forward power.

4.3.3 Overall Equilibrium Composition

In catalytic systems, the thermodynamically calculated equilibrium composition can be a useful tool to assist in the interpretation of experimental results. Direct comparisons of experimental data and equilibrium calculations require that the system approach equilibrium. In the case of a hydrocarbon system with large $-\Delta G_{rxn}$, complete conversion of the feed is expected with sufficient residence time. Equilibrium calculations for the system of interest were obtained using ASPEN Plus computational tools, minimizing the total Gibbs free energy of the system as shown in Figure 4.2.

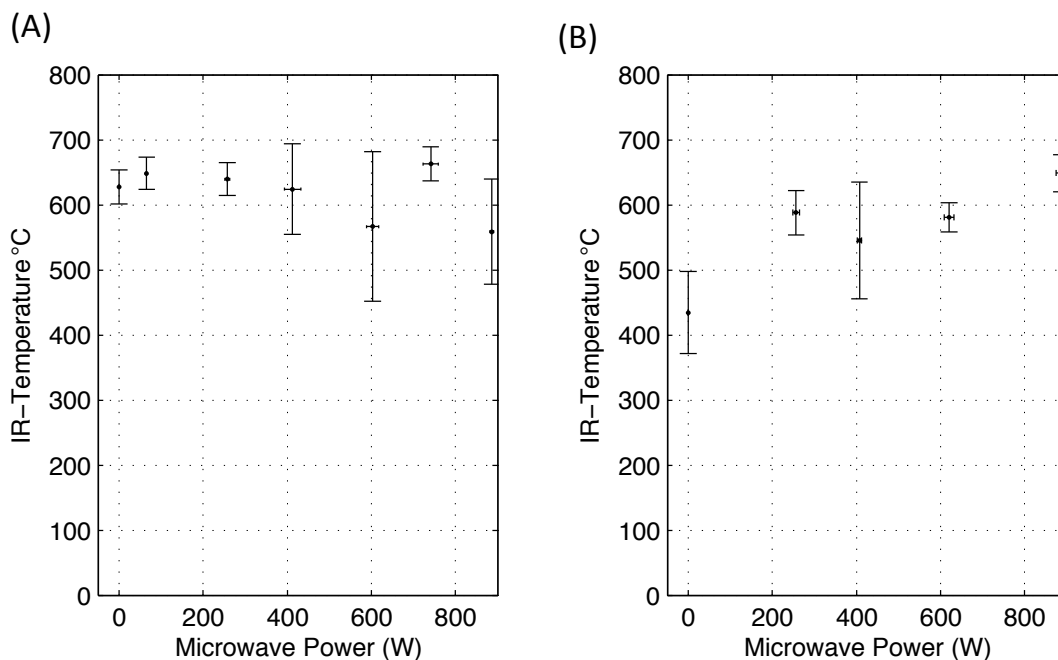


Figure 4.1: IR measured temperatures and standard deviations of measured values under POX (A) and ATR (B) conditions.

By tracking changes in experimental compositions, a thermodynamic temperature can theoretically be inferred. A direct comparison of compositions was not possible in this work as reaction conditions remained far from equilibrium. Operation under low total oxygen and high space velocities confounded attempts to make quantitative comparisons between thermodynamic calculated compositions and those obtained in experiments. Determination of the reformer operating temperature range based on compositional comparisons thus proved inconclusive.

4.3.4 Elevated Sample Temperature Composition Comparison

To gain insight into the elevated temperature experienced by a reforming system operating under microwave irradiation, product distributions were compared with those obtained by increasing the system temperature within the heated zone of a furnace. Trends in product distributions with increasing microwave power may be

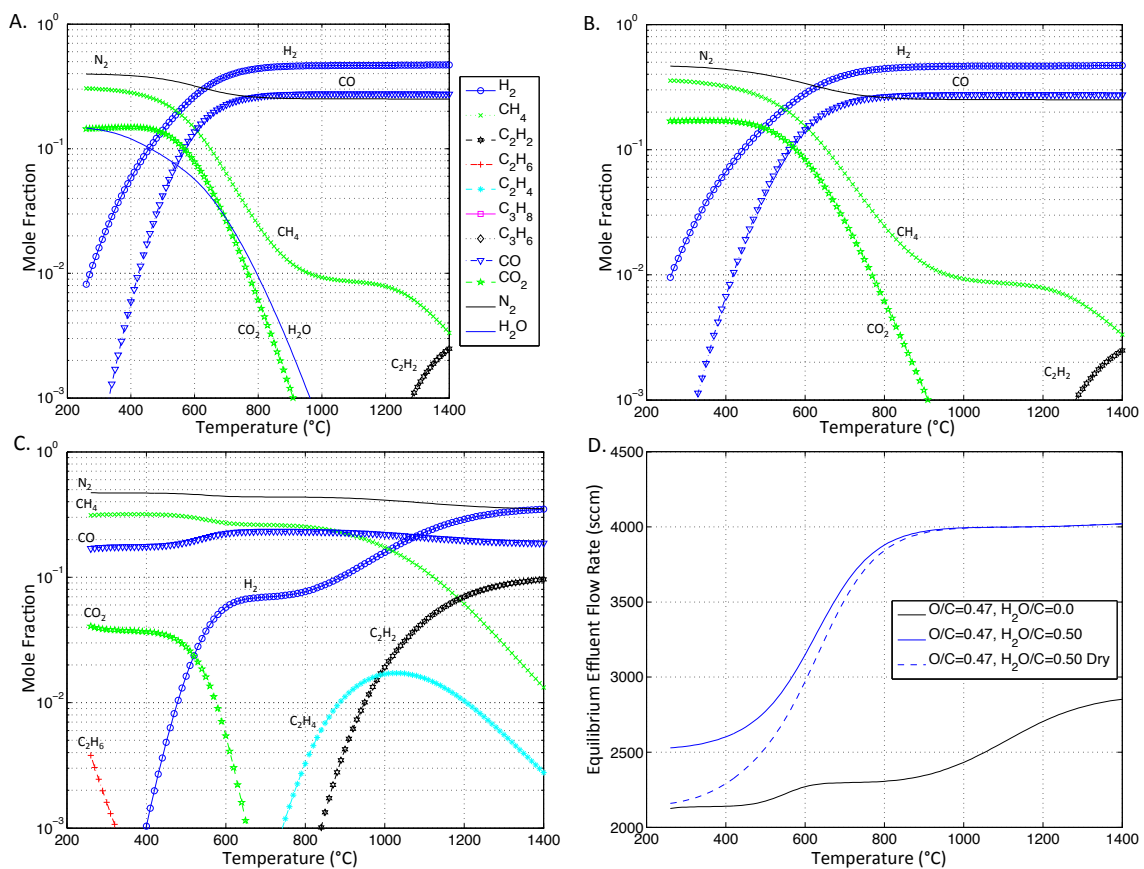


Figure 4.2: Thermodynamic equilibrium calculations for a mixture of H_2 , H_2O , O_2 , N_2 , CH_4 , C_2H_2 , C_2H_4 , C_2H_6 , C_3H_6 , C_3H_8 , CO and CO_2 . Mole fractions for feed conditions of: (A) ATR, (B) ATR dry effluent, (C) POX, (D) Calculated effluent flow rates.

compared with samples run under elevated temperature environments within a furnace to obtain effective temperature changes within the system.

Sample temperatures were increased by placing catalysts within the furnace and increasing the set-point temperature above the standard pre-heat temperature within the microwave waveguide. Within the furnace, the catalyst containing section of quartz tubing was wrapped in quartz-wool to prevent the formation of hot spots due to radiation from the furnace heating coils. Catalysts were subsequently run under standard POX or ATR conditions while monitoring the effluent concentrations and temperature, from which a comparison can be made with compositions obtained under microwave conditions. The maximum furnace set-point was 550 °C. Higher temperatures were not attainable within the furnace due to pre-combustion of the feed. Figure 4.3 is an example of the method used to fit microwave data to furnace obtained values in ATR and POX experiments. Furnace compositions or yields are plotted as a function of exit temperature as measured by a thermocouple placed within a thermowell directly below the catalyst at the center of the reaction tube. Table 4.2 contains the exit temperatures observed under each condition, with "Waveguide" indicating that the reaction was carried out in the microwave chamber without irradiation. An extrapolation of the trend observed in the furnace data is then used to match with microwave data. In certain instances, the microwave data fits the trends observed under traditional heating quite well; this behavior may be considered traditional thermal effects. Species used in the comparison of furnace and microwave obtained yields with similar trends include H₂, CO₂, CH₄, C₂H₄, C₂H₆, C₃H₆ and C₃H₈ for POX conditions and H₂, CO, C₂H₂, C₂H₄ and C₃H₈ for ATR experiments

By matching the furnace and microwave data as demonstrated in Figure 4.3, Figure 4.4 is the estimated system temperatures attained under microwave irradiation with 95% confidence intervals as a function of the input of microwave energy. Despite

Table 4.2: Catalyst exit temperatures recorded under each operating condition. Uncertainty on values is $\pm 12 - 21$ °C.

Condition	POX °C	ATR °C
Waveguide	550	573
Furnace 350 °C	647	606
Furnace 450 °C	684	632
Furnace 550 °C	726	678

excluding species whose trends with temperature do not match between the two modes of heating, variance across species examined led to significant uncertainty in the reported value. Despite this uncertainty, the trend observed is consistent with other methods of estimating temperature within the system. Additional information is derived in this analysis related to the relative temperature experienced by the reaction pathway leading to each product as discussed in section 2.4.1.

4.3.5 Temperature Programmed Oxidation of Carbon

Carbon deposited on reforming catalysts during operation contain information within their structure about the temperature environment in which they were created. The temperature programmed oxidation (TPO) of carbon is a means of determining the temperature at which carbon is oxidized, providing insight into its morphology. Representative TPO peaks for samples having undergone POX and ATR operation are shown in Figure 4.5. Of note is the shift in peak position with increasing irradiation along with the decrease in total carbon present. To further understand the significance of these shifts, calibrations were produced using data from the TPO of carbon deposited during elevated furnace temperature experiments in addition to carbon that was subject to post reaction heat treatment.

Carbon deposited during reaction within the furnace at elevated temperatures was analyzed for TPO behavior shown in Figure 4.6. As with samples exposed to increasing levels of microwave irradiation, a shift in TPO peak position to higher temperatures is observed with increasing furnace temperature. Table 4.3 summarizes

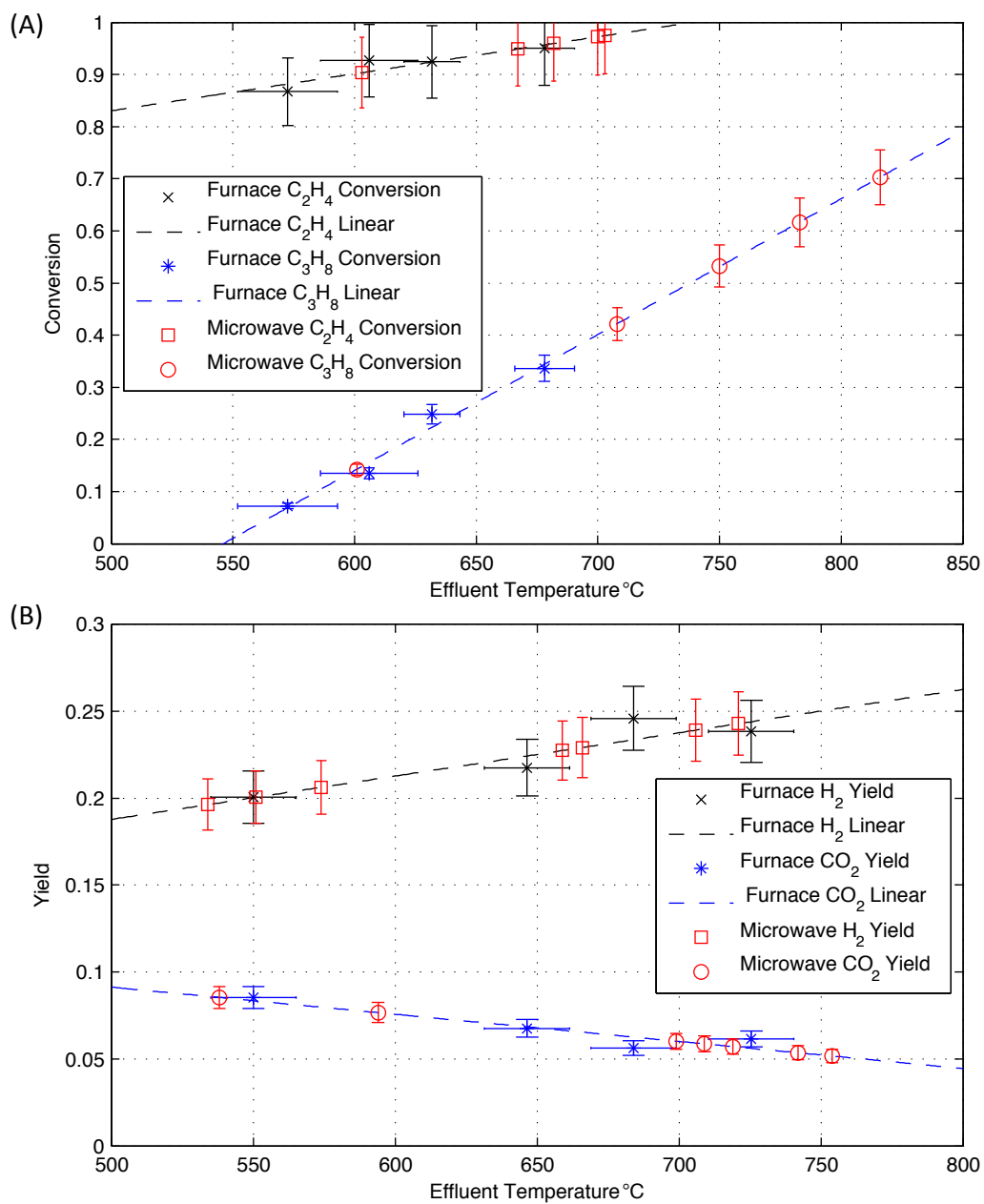


Figure 4.3: Comparison of selected yields and conversions between samples run under microwave conditions and those run under elevated temperatures within a furnace for ATR (A) and POX (B) conditions.

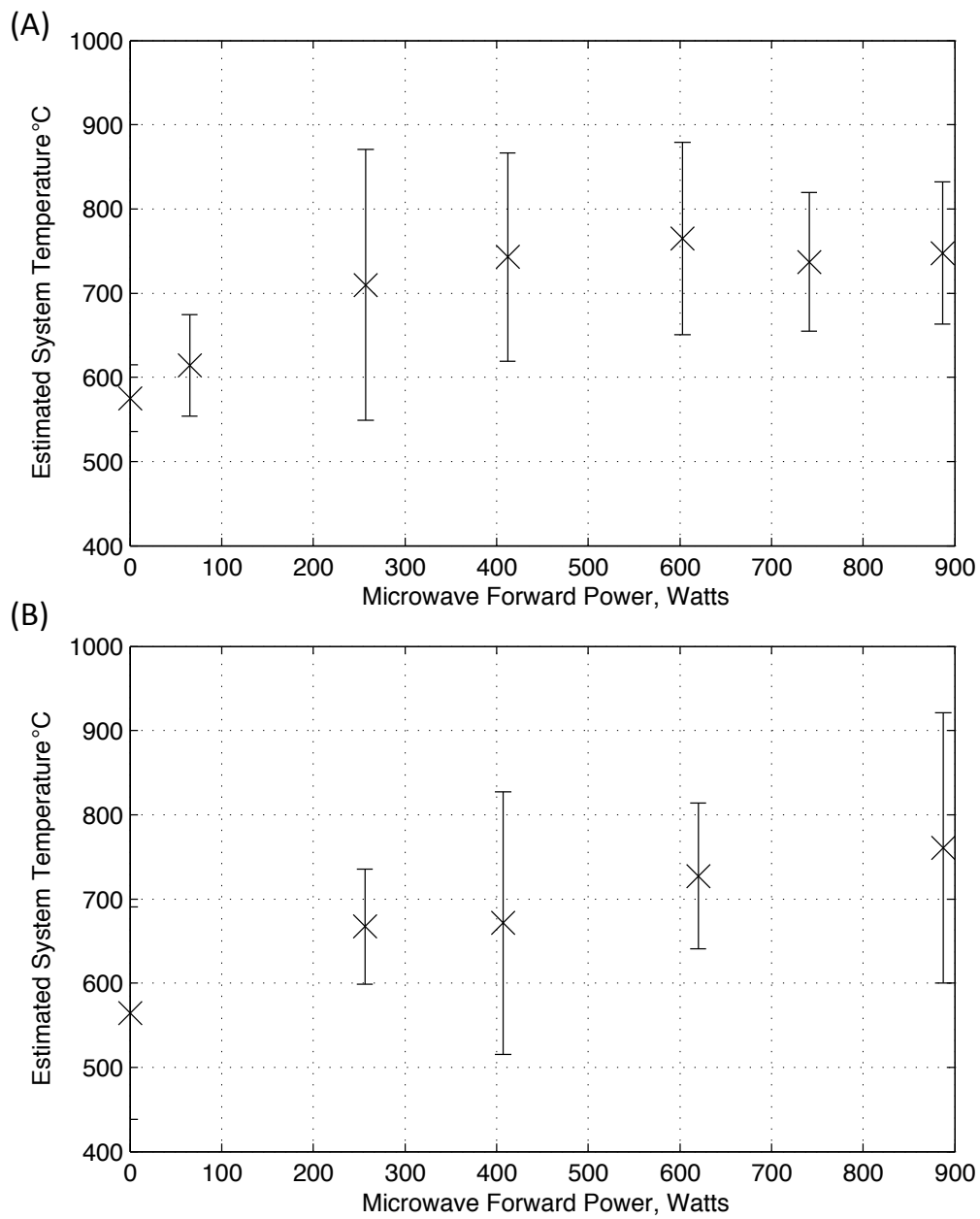


Figure 4.4: POX (A) and ATR (B) temperatures obtained from furnace data comparisons.

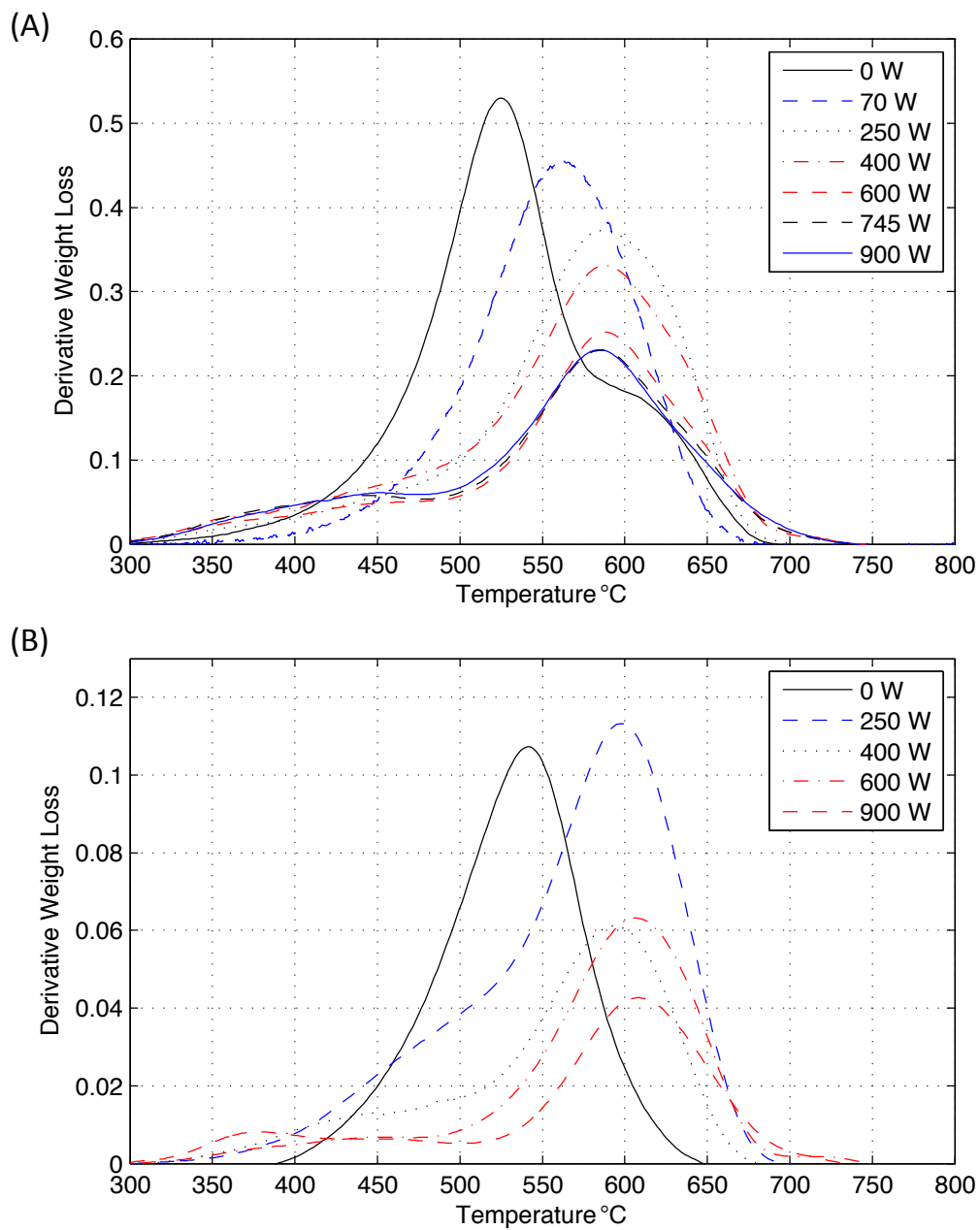


Figure 4.5: Temperature Programmed Oxidation of carbon deposits on catalyst samples after POX (A) and ATR (R) reaction conditions.

Table 4.3: TPO position of maximum peak feature for samples reacted without irradiation in the waveguide and furnace.

Condition	POX °C	ATR °C
Waveguide	525	541
Furnace 350 °C	573	584
Furnace 450 °C	649	583
Furnace 550 °C	641	580

the TPO peak positions of each sample. Compared with the shift in peak position for irradiated samples, elevating the sample temperature within the furnace shifts the POX peaks to a much higher temperature. Conversely, ATR samples exhibited a lesser shift in peak position in the furnace compared with microwave exposure with a maximum shift of 43 °C. In both instances, the relationship between peak position and temperature was not linear, rather the values increase initially and then plateau, leading to significant uncertainty in sample temperatures estimated from comparing shifts in TPO features.

Temperature calibrations were also performed by observing shifts in the TPO peak position of heat treated carbon. Coked samples were obtained from catalysts exposed to a standard 15 minutes of reaction within the waveguide under POX conditions. Samples were subsequently ramped at 10 °C min⁻¹ to a pre-determined treatment temperature between 650 °C and 900 °C under flowing N₂ and held for 60 minutes before rapid cooling to room temperature. Subsequent TPO analysis showed a shift to higher temperatures after thermal treatment similar to that observed under microwave irradiation. Figure 4.7 is a plot of the excess temperature experienced by the sample as a function of the shift in TPO peak position along with 95% confidence intervals. Comparison of irradiated carbon TPO peak position to samples run within the furnace, where effluent temperature is measured, and to heat treated carbon samples provides two additional means of estimating the system temperature as experienced by carbon.

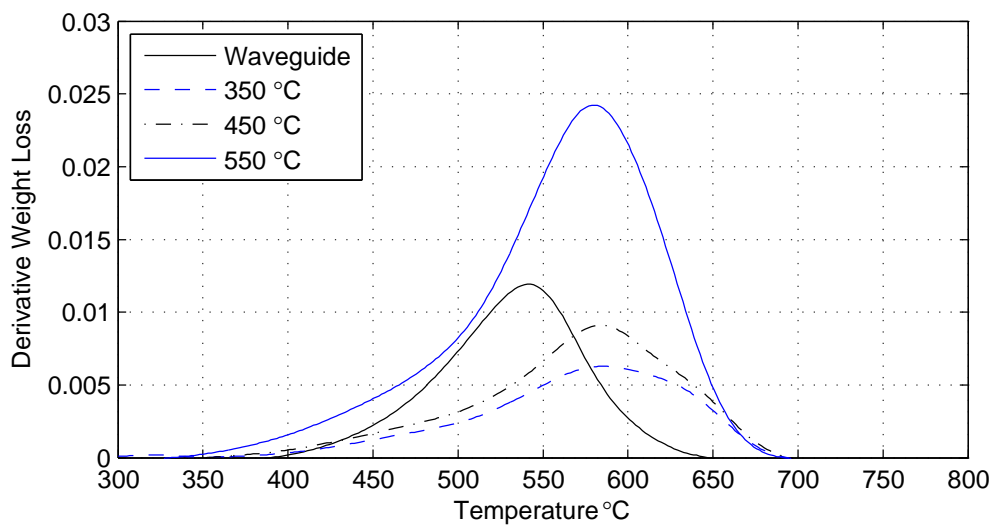
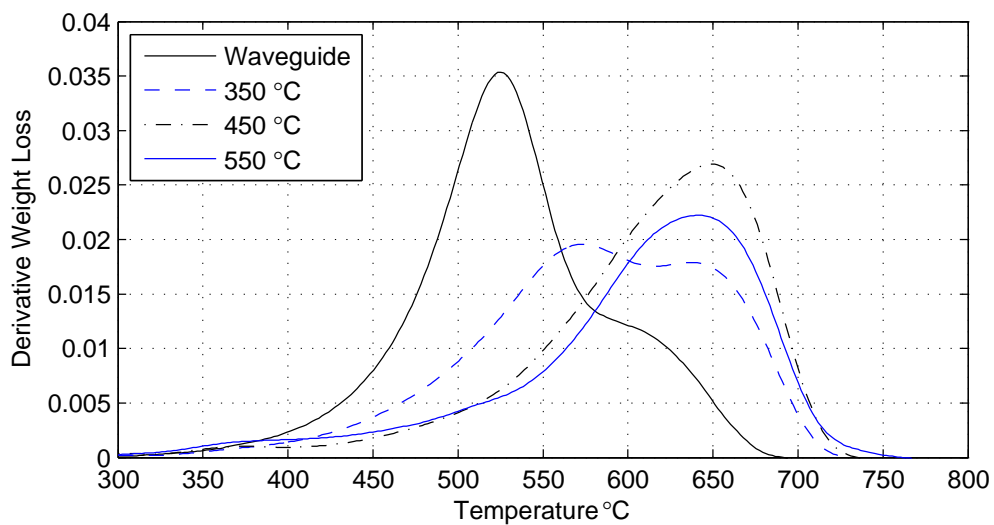


Figure 4.6: TPO peaks of samples run within the microwave waveguide and furnace at specified temperatures under POX (A) and ATR (B) conditions.

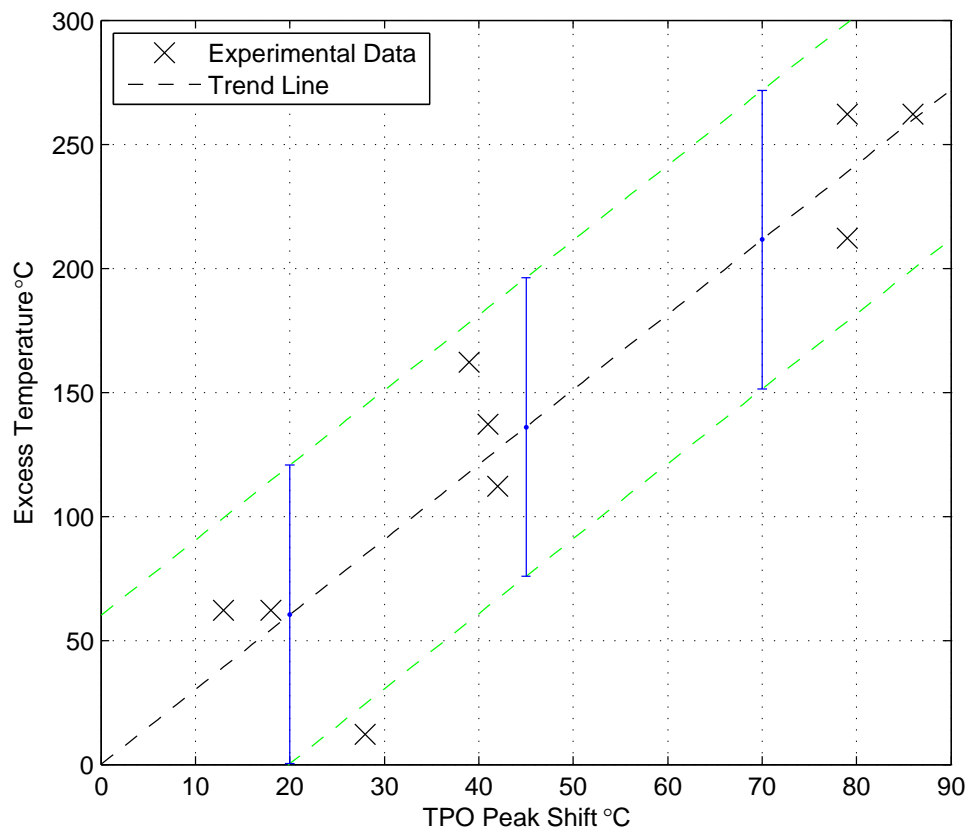


Figure 4.7: Heat treated carbon. Excess heat treatment temperature experienced by sample as a function of the observed TPO peak shift. 95% confidence intervals provided in green.

4.3.6 Water-Gas Shift Equilibrium

The water-gas shift (WGS) reaction, Equation (4.1) is highly temperature dependent and is generally considered to approach equilibrium very quickly, even at short contact times [7]. The WGS equilibrium can therefore be a useful tool to monitor the state of a catalyst. The WGS reaction is only slightly exothermic with $\Delta H_{\text{rxn}} = -41.2$ KJ mol⁻¹ and is frequently carried out over nickel catalysts. Industrially, both a high temperature and low temperature shift reaction is used to take advantage of the increased H₂ produced at low temperatures. Figure 4.8 contains the equilibrium K_{WGS} as defined by Equation (4.2). Within this system, the WGS equilibrium was used in two ways to monitor the temperature within the system. A calibration was first developed using a model WGS system to relate changes in microwave power to catalyst temperature. Secondly the K_{WGS} established during the reforming of hydrocarbons was monitored to correlate changes in product distributions with the catalyst temperature.



$$K_{\text{WGS}} = \frac{[\text{CO}_2][\text{H}_2]}{[\text{CO}][\text{H}_2\text{O}]} \quad (4.2)$$

The goal of initial WGS experiments was to establish the equilibrium K_{WGS} curve for a catalyst and then use this established behavior to reconcile the measured IR temperature with the observed K_{WGS} . This method is very similar to generating a lightoff curve for a catalyst and using the known kinetics to then back out a temperature. A standard monolith catalyst was loaded into the furnace and exposed to flowing CO₂ (4.5 mmol min⁻¹) and H₂ (13.4 mmol min⁻¹) in Argon (40.2 mmol min⁻¹) with the effluent analyzed by mass spectrometer. The furnace temperature was ramped to 750 °C at 5 °C min⁻¹ to obtain the characteristic curve for the catalyst labeled “Furnace Data” in Figure 4.8. Next, the catalyst was moved into the microwave cavity

Table 4.4: Tabular summary of the model water-gas shift analysis presented in Figure 4.8.

Sample Point	MW Power (Watts)	IR Temperature °C	Effective Temperature °C	Temperature Increase °C
A	0	298	N.A.	0
B	190	308	N.A.	10 (IR)
C→C2	393	319	368	70
D→D2	589	336	418	120
E→E2	759	356	496	198

and heated to ~ 298 °C (point A). The catalyst was then exposed to increasing levels of microwave radiation and the effluent K_{WGS} plotted vs. IR measured temperature (points B, C, D, E). Using the previously established K_{WGS} “Furnace Data” curve for the system, the effective temperature of the catalyst can be determined; that is the temperature required to reach the K_{WGS} value achieved under microwave irradiation (Points C2, D2, E2). Observations are summarized in Table 4.4 where it is apparent, that with increasing irradiation, the effective temperature of the catalyst increases by up to 200 °C

4.3.7 Water-Gas Shift Equilibrium Under Reforming Conditions

Previously, the WGS equilibrium was used to track changes in temperature for irradiated model systems containing only CO, H₂O, CO₂, H₂ and Ar. To extend this tool to reforming systems, a similar approach is used where the WGS equilibrium is tracked in catalysts under the POX and ATR conditions described previously. K_{WGS} is first measured in samples placed in the furnace position such that their effluent temperature can be measured at multiple furnace temperatures, T_{Furnace} . Effluent water concentration is not measured by mass spectrometer, thus it is estimated as $0.1F_{\text{O}_2,in}$ for POX cases and as the missing O₂ in the ATR material balance ($F_{\text{O}_2,in} - F_{\text{O}_2,out}$). Various means for estimating water concentration were used with similar results. K_{WGS} values from furnace experiments were then compared with equilibrium WGS values calculated by ASPEN for the reforming gas mixture of interest to obtain a

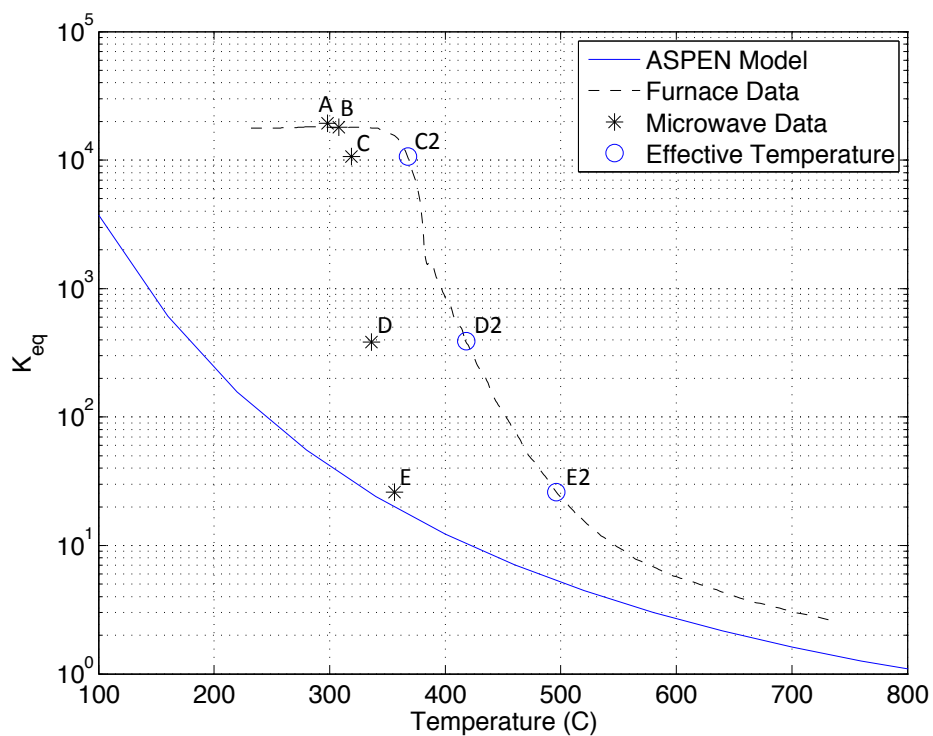


Figure 4.8: Water-Gas Shift data for a catalyst containing equilibrium data (ASPEN Model), characteristic curve of the catalyst (Furnace Data), K_{WGS} plotted vs. IR Temperature (Microwave Data), and actual sample temperature while irradiated (Effective Temperature).

WGS equilibrium temperature, $T_{\text{WGS,eq}}$. Figure 4.9A shows $T_{\text{WGS,eq}}$ vs. T_{Furnace} with a corresponding slope of 0.48. Every degree in WGS equilibrium predicted temperature change correlates to a 2 °C change in the measured sample exit temperature. Figure 4.9B-C are the effluent K_{WGS} viewed in light of Figure 4.9A, suggesting that the ATR system experiences a roughly linear increase in temperature with increasing irradiation, while the POX case appears to level out above 400 W. Variation in the measured values results in the significant uncertainty reflected by 95% confidence intervals in Figure 4.9B-C. At a Forward power level of 400 W, both cases experience an elevated sample temperature by approximately 110 °C.

4.3.8 System Modeling and Model-Data Comparison

Requirements for an adiabatic microwave reactor capable of initiating and sustaining reactions at high temperatures led to the design of a system with complex heat transfer characteristics. Many reaction systems consist of a reactor tube within a heated zone such as a furnace. The microwave reactor presented in this work consists of the catalyst mounted below a furnace, within a microwave waveguide, with an annulus through which hot furnace air is forced over the sample. The microwave waveguide itself is water cooled, placing hot and cold components within very short distances of one another. The primary goal of modeling the Reactor system is to gain insight into the temperature profiles and heat transfer at play.

Initial heat transfer modeling explored the possibility of differentially heating a system with very small metallic particles. Heat transfer from an alumina supported 50 nm diameter Ni particle heated by microwave radiation was examined for the possibility of attaining significant temperature gradients over the short length-scales involved. The Equation of Energy (4.5) was employed in cylindrical coordinates with symmetry, reducing the complexity by one dimension. Numerical solutions were obtained using Matlab and standard finite difference methods [109, 110]. Results

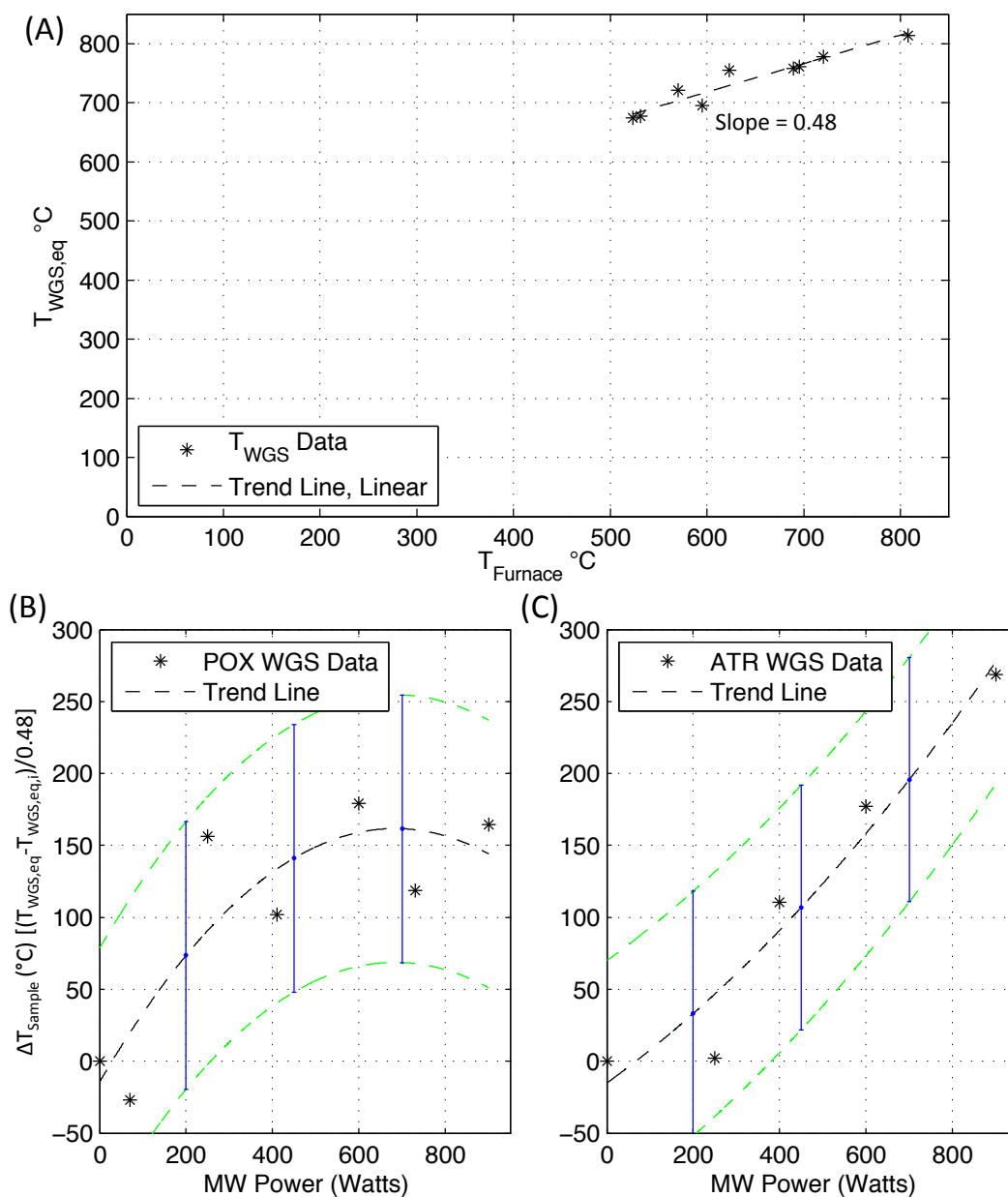


Figure 4.9: Water-Gas shift comparison of thermodynamically predicted system temperature based off of the WGS equilibrium ($T_{WGS,eq}$) as a function of the measured exit temperature within the furnace ($T_{Furnace}$) (A). Observed change in temperature of operation for irradiated samples under POX (B) and ATR (C) conditions as a function of MW power with 95% confidence intervals.

indicate that initial heating rates of the Ni catalyst particle were on the order of 1,000 °C s⁻¹, however temperature gradients between Ni and air or alumina are not sustainable over tens of nanometers, as temperature equilibration occurs very quickly over those length-scales. This work is in agreement with the work of J.R. Thomas Jr. and Perry et al [111, 62].

Figure 4.10 provides several views of the system being modeled and the approach to simplifying the geometries into a solvable problem. Modeling of the reactor system was accomplished by means of a differential volume approach in cylindrical coordinates, assuming axial symmetry ($d\theta = 0$). The governing equations used to describe the transport of mass and energy were the Equation of Continuity (4.3), Equation of Motion (4.4), Equation of Energy (4.5), Equation of Continuity for Species A (4.6) and the Helmholtz Equation for a Rectangular Waveguide (4.7) [110].

$$\frac{\partial \rho}{\partial t} = (\nabla \cdot \rho v) \quad (4.3)$$

$$\rho \frac{Dv}{Dt} = -\nabla p + \mu \nabla^2 v + \rho g \quad (4.4)$$

$$\rho C_p \frac{DT}{Dt} = k \nabla^2 T + \mu \Phi_v \quad (4.5)$$

$$\rho \frac{D\omega_A}{Dt} = \rho D_{AB} \nabla^2 \omega_A + r_A \quad (4.6)$$

$$0 = \partial_x^2 H_z(x) + k_c^2 H_z(x) \quad (4.7)$$

Numerous assumptions went into formulating a problem that was solvable in a reasonable length of time using finite difference techniques. Material properties were obtained at elevated temperatures wherever possible. Some of the assumptions include: constant mass density, ($\rho = \text{constant}$), no r or θ component of velocity, ($v_r = v_\theta = 0$ and $v_z = \text{constant}$). Effects of viscosity and gravity were assumed to be negligible, ($\mu \nabla^2 v = \rho g = 0$), viscous dissipation was also negligible compared with the reaction exotherm, $\mu \Phi_v = 0$. Mass transport by diffusion was determined to be much slower than convective transport within the system and thus $\rho D_{AB} \nabla^2 \omega_A = 0$.

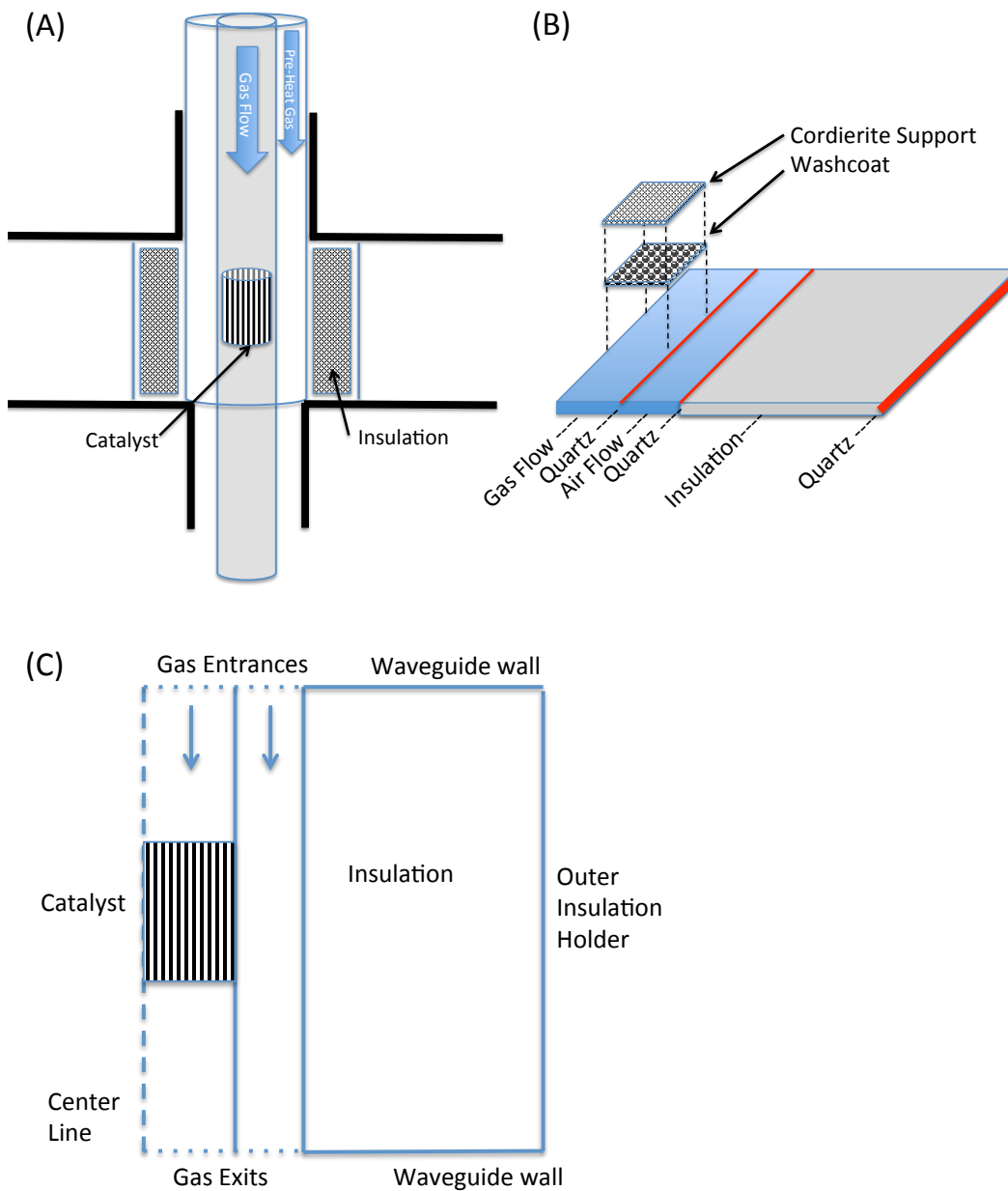


Figure 4.10: Diagrams of Reaction system: (A) Catalyst within reaction tube with annular pre-heat gas flow and insulation contained in waveguide. (B) Layering of model to capture heat transfer dynamics. (C) System layout for modeling

Boundary conditions used in this study include a constant temperature on the waveguide walls as well as at the gas inlets within the reaction tube and annulus. Axial symmetry was observed, setting the first derivative to 0 along $r = 0$ for both the catalyst and air components.

The Ni/CZO/Cordierite monolith catalyst was treated as two continuous solid phases: a Ni/CZO washcoat phase in which reactions occur, and a cordierite support phase to which heat is transferred from the washcoat. Densities of the washcoat and support were based upon their bulk densities as a washcoated catalyst to correct for their treatment as a continuous solid. A major limitation of not modeling the monolith channel is the inability to predict bulk mass transfer limitations within the system. In practice, O_2 is the limiting reagent in all experiments and the conversion of O_2 is near complete in all instances indicating that the oxidation reaction is not mass transfer limited, though this may be due to homogeneous reaction. A reaction rate based on the disappearance of O_2 was established with a reaction order of 1.25 in O_2 . As the primary goal of the model was to capture heat transfer dynamics, this method was deemed sufficient for capturing the majority of the system behavior with much greater computational ease.

It has been shown that radiative heat transfer within a monolith structure can significantly increase the rate of heat transfer at high temperatures [112, 113]. A simplified 1-D heat transfer model was used to approximate radiative heat transfer by changing the effective thermal conductivity of the catalyst block. Thermal conductivity increases roughly exponentially, though a 3rd degree polynomial was used as a more accurate approximation, which is then used to update the catalyst thermal conductivity based on the local temperatures. Thermal conductivity of the catalyst varies from $0.58 \text{ W m}^{-1} \text{ K}^{-1}$ at 273 K to $14.5 \text{ W m}^{-1} \text{ K}^{-1}$ at 1073 K.

Heat transfer between the catalyst and adjacent air was mediated by a solid-gas

heat transfer coefficient according to Fourier's Law:

$$q = -UA\nabla T \quad (4.8)$$

Radiative heat transfer between the outside of the catalyst and surrounding insulation was accounted for using the radiative heat transfer equation:

$$Q_{12} = A_1 \bar{F}_{12} \sigma (T_1^4 - T_2^4) \quad (4.9)$$

As mentioned previously, chemical reactions occur within the washcoat layer which then exchanges heat with the support phase according to:

$$q = -k \frac{dT}{dx} \quad (4.10)$$

A mean distance was determined between the center of mass of the washcoat and cordierite over which the temperature difference and heat transfer rate were determined.

Within a rectangular waveguide, operating in the TE₁₀ mode the EM field is highly constrained, simplifying Equation (4.7) to:

$$E_y(x) = E_0 \sin\left(\frac{\pi x}{a}\right) \quad (4.11)$$

where x is the coordinate along the waveguide width, a . Absorption of microwave energy in a lossy material is modeled by Equation (4.12). When the dielectric loss of the material is unknown, Equation (4.13) may be used as an approximation for

conducting materials.

$$P_E = 2\pi f \epsilon_0 \epsilon'' E_{\text{rms}}^2 \quad (4.12)$$

$$P_E = \sigma E_{\text{rms}}^2 \quad (4.13)$$

Microwave absorption was modeled based on the catalyst composition of 80 wt.% Cordierite, 18 wt.% CZO and 2 wt.% Ni nano-particles. Ceramics such as Cordierite and CZO tend to have very low microwave cross section at room temperature, however at high temperatures, ceramics can exhibit thermal runaway behavior in an EM field due to increasing conductivity. Equation (4.13) was used to model the absorption behavior of Cordierite and CZO, using literature data of their temperature-conductivity behavior [114, 115]. Ni nano-particles were modeled using Equation (4.12) with $\epsilon'' = 0.5 \pm 0.2$ and temperature effects consistent with those observed in the bulk conductivity [116, 117]. Work by Tang and Lau et al. on the heating of particles in EM fields demonstrated that E field heating dominates when the skin depth is much greater than the particle diameter as is the case in this study [118]. A volume average of the material contributions is used to compute the total power absorbed in the system. Figure 4.11 shows the temperature behavior of the effective ϵ'' obtained for each material as well as the volume weighted composite value. Generally, an ϵ'' of greater than 0.1 is required to heat a material in a microwave field.

In silica, implementation of the reactor model was performed using Matlab. A summary of the model parameters are listed in Table 4.5. Discretization of the aforementioned equations was accomplished using finite difference procedures, taking into consideration truncation error, consistency and the stability of the system. Modeling was performed using a forward-difference approach for the time derivative and a central-difference representation with respect to spatial variables. Gradient functions within Matlab were found to be slow and produce instabilities; they were re-written

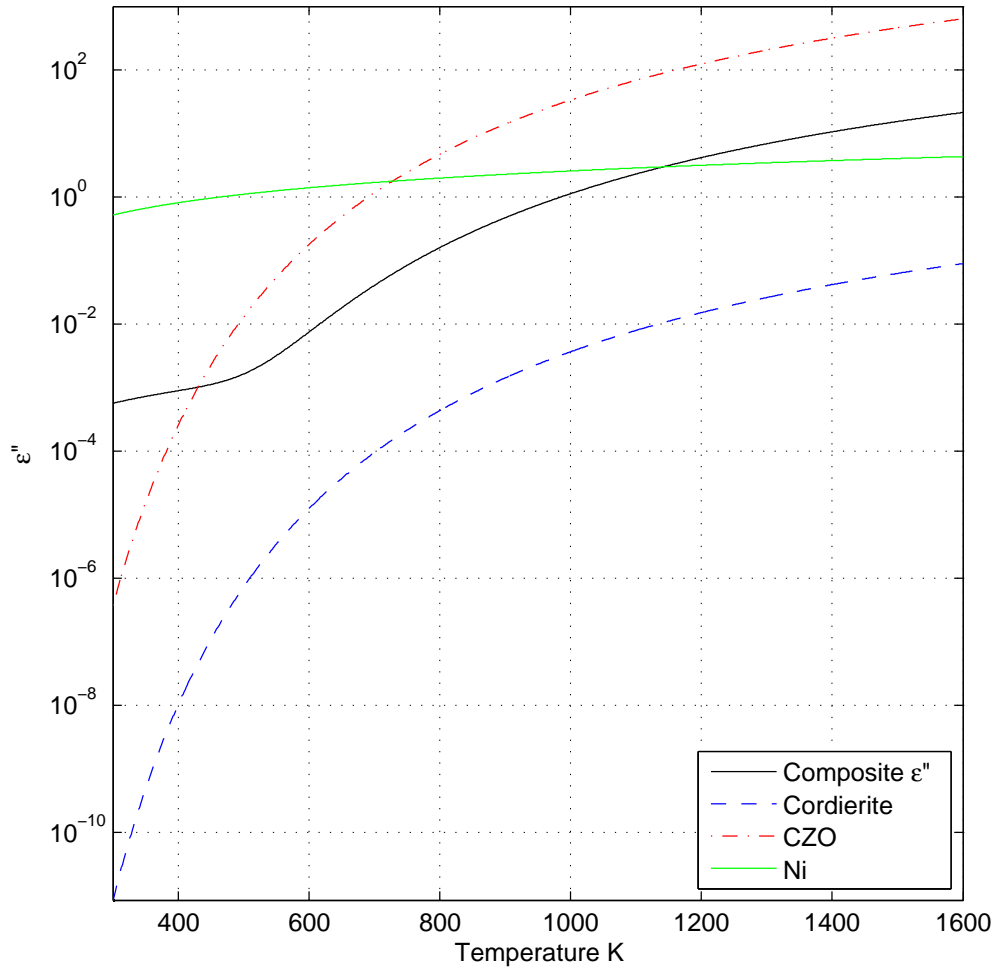


Figure 4.11: Composite ϵ'' using volume average of pure component Cordierite, CZO and Ni nano-particles. Cordierite and CZO ϵ'' values approximated from electrical conductivity data.

Table 4.5: Microwave reactor model parameters.

Parameter	Value	Units
Density of cordierite monolith	356.8	kg m ⁻³
Density of catalyst wash coat	89.2	kg m ⁻³
Catalyst heat capacity	900	J kg ⁻¹ K ⁻¹
Catalyst thermal conductivity	Variable	
Insulation density	44	kg m ⁻³
Insulation heat capacity	670	J kg ⁻¹ K ⁻¹
Insulation thermal conductivity	0.16	J s ⁻¹ m ⁻¹ K ⁻¹
Quartz density	2200	kg m ⁻³
Quartz heat capacity	670	J kg ⁻¹ K ⁻¹
Quartz thermal conductivity	1.4	J s ⁻¹ m ⁻¹ K ⁻¹
Air density	0.363	kg m ⁻³
Air heat capacity	1001	J kg ⁻¹ K ⁻¹
Air thermal conductivity	0.064	J s ⁻¹ m ⁻¹ K ⁻¹
Monolith surface area for heat exchange	3151	m ² m ⁻³
Catalyst-Air heat transfer coefficient	16	J s ⁻¹ m ⁻² K ⁻¹
Reaction gas velocity	2.45	m s ⁻¹
Annulus gas flow velocity	3.0	m s ⁻¹
Exotherm (POX to CO, O ₂ basis)	4,700,000	J kg _{O₂} ⁻¹
O ₂ mass fraction	0.115	
Radiative heat loss view factor	0.35	
Δr	0.000242	m
Δz	0.000251	m
Δt	0.00005	s

to include difference approximations utilizing 3 or more points. Improved difference schemes also reduced the order of truncation error from h to h^4 , where h is the grid spacing (Δr , Δz) with the total truncation error of the order $\Delta t + h^4$. The stability criteria for a 2-D heat equation of $\alpha \Delta t [1/(\Delta r)^2 + (1/\Delta z)^2] \leq \frac{1}{2}$ was utilized to guide system design [119, 109, 120].

Modeling of the microwave reactor system was performed to obtain steady state temperature distributions within the catalyst, gas and surrounding structures. Figure 4.12 shows the temperature distribution within the system, given the parameters stated in Table 4.5. High temperature gradients are established over short distances due to the use of a water cooled waveguide surrounding the reaction zone. The front face of the catalyst is the hottest region, as observed in laboratory work with the ma-

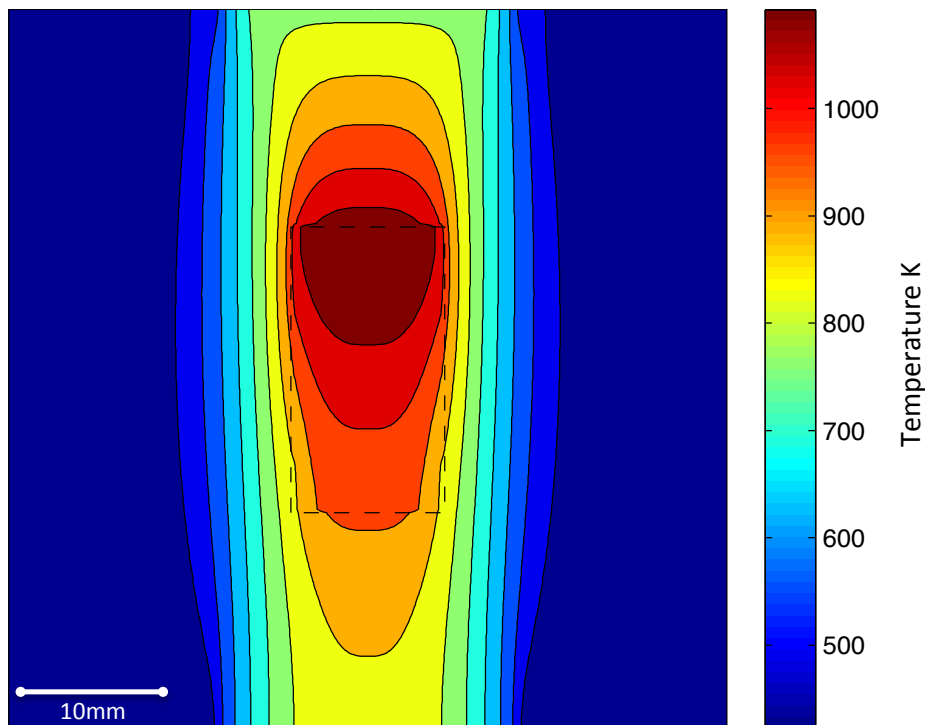


Figure 4.12: Model of catalytic system under steady state operation with catalyst temperature superimposed within dashed box. Image is a vertical slice with gas entering from the top. Exit gas temperature at a thermocouple position is 658 °C, consistent with experimental results.

majority of the exotherm produced within the first few millimeters as oxygen is quickly consumed. These results highlight the importance of accurate thermocouple positioning within the reaction tube. Slight deviations in the axial or radial position between experiments can lead to significant deviations in the measured temperature. It is apparent from this modeling that the catalyst suffers significant heat losses, resulting in greater than 100 °C temperature gradients across the catalyst.

Of primary interest for this study is the influence of EM irradiation on temperature distributions within the catalyst. As noted, it is difficult to determine the exact electric field strength within the cavity, thus a range of field strengths, 0 - 10,000 V m⁻¹ were used with the results summarized in Figure 4.13. The model confirms experimental observations that the system heats readily under EM fields. Compared to the base case conditions, heating by microwaves can raise the center

catalyst temperature by greater than 250 °C. Figure 4.13A provides the change in temperature over base case conditions at three locations. Temperatures measured on the exterior of the catalyst as viewed by an IR pyrometer would underreport the actual temperature of the catalyst in this system, providing further evidence that IR measurements are minimally useful at best. Contour plots of the difference in temperature between the irradiated catalyst and catalyst under base case conditions are provided in Figure 4.13C with the greatest temperature increase occurring along the center line of the catalyst.

At each EM field strength, the volumetric power dissipation was computed for the model, Figure 4.13B, for comparison with experimental power absorption measurements shown in Figure 4.14A. Calibrations were performed with an empty cavity to account for dissipation on the walls and within the sliding short circuit of the waveguide. Based on the experimental power absorption of 2 - 47 MW m⁻³, the model predicted electric field strength is 4,000 - 8,000 V m⁻¹, corresponding to a predicted temperature increase at the catalyst center of 60 - 200 °C. This range of field strengths is reasonable given the low dielectric loss of the catalyst and the orientation of the waveguide components. Increases in operating temperatures for the various conditions are provided in Figure 4.14C. Similar trends in temperature are observed with the model-data comparison as were obtained by other methods with high initial temperature increases.

Apart from the analysis of temperature change within an irradiated catalyst, the system efficiency was evaluated based on the rate of microwave energy absorbed by the catalyst compared with the Lower Heating Value (LHV) of the feed hydrocarbons. Microwave energy accounts for at most, 14% of the feed LHV as shown in Figure 4.14B. Within the microwave system used in this work, only a small fraction of the power produced was absorbed by the sample, the remainder being absorbed by the waveguide and water loads. In an industrial implementation, proper microwave

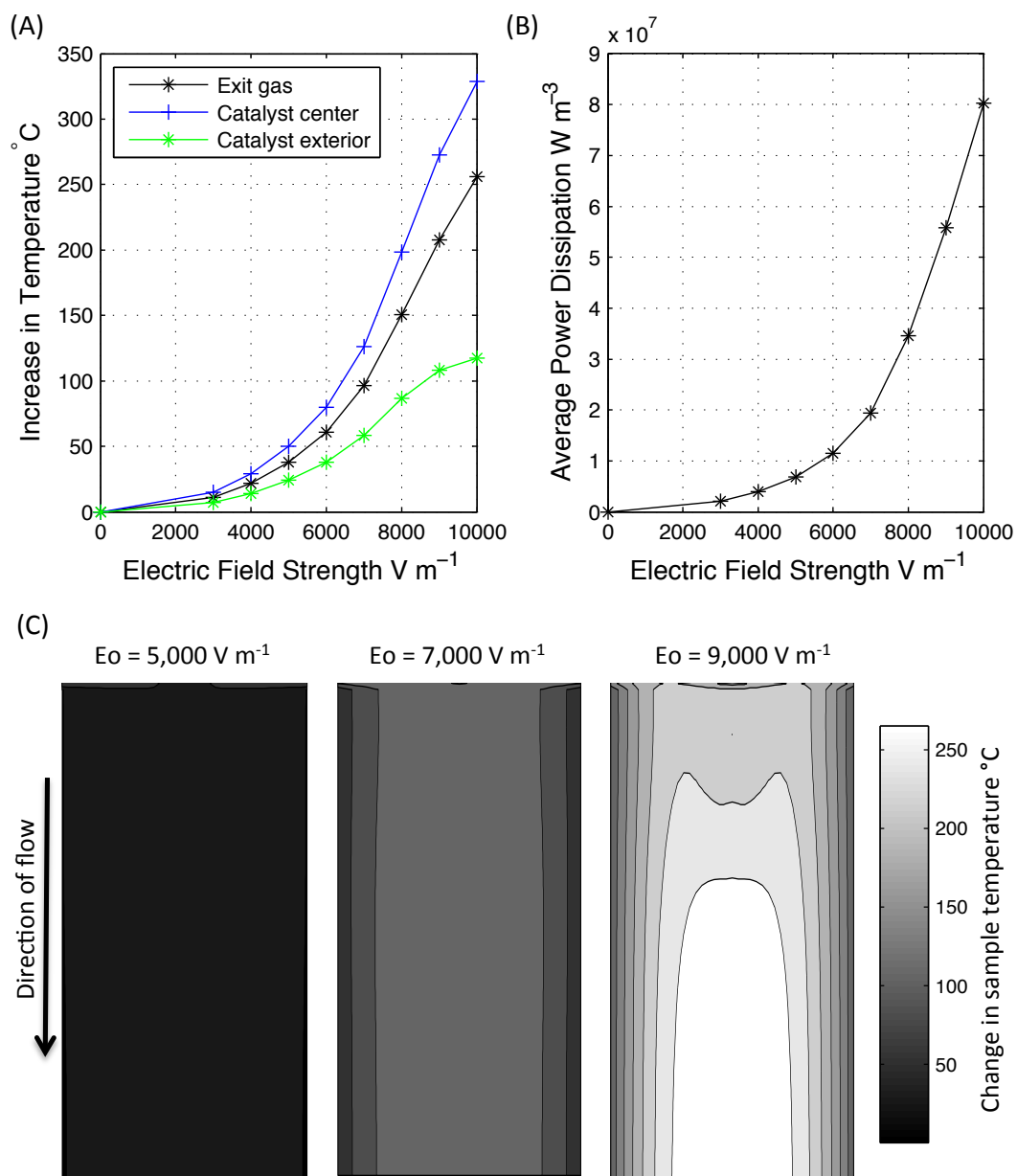


Figure 4.13: (A) Increase in sample temperature over base case conditions at specified points. (B) Power dissipation within catalyst. (C) Profiles of catalyst temperature increase under specified EM field strength.

cavity design can minimize return losses to couple almost all of the microwave radiation generated into the catalyst. Further economic analysis is needed to determine if the energy input provides sufficient benefits in the form of increased syngas yield and decreased deactivation to justify the increased system cost.

4.4 Summary and Limitations

Temperature measurement within a microwave field can be very challenging and brings into light the uncertainty associated with measuring temperature in any system in which significant heat losses and heat generation occur simultaneously. Thermocouples are generally considered accurate, however heat transfer modeling has shown that altering the position of a thermocouple a few millimeters can drastically influence the measured value. Within this work, a series of methods have been presented to estimate the change in sample temperature when subject to irradiation. A summary of the aforementioned approaches to estimating the temperature increase of a reformer operating under ATR and POX conditions is provided in Table 4.6. When all temperature shift determination methods are viewed together, consistent trends are apparent in Figure 4.15. It is clear that sample temperatures increase rapidly in POX systems by around 150 °C and are not subject to further heating above 400 W. ATR systems experience a linear trend of temperature increase with microwave power with a rise of sample temperature in excess of 200 °C.

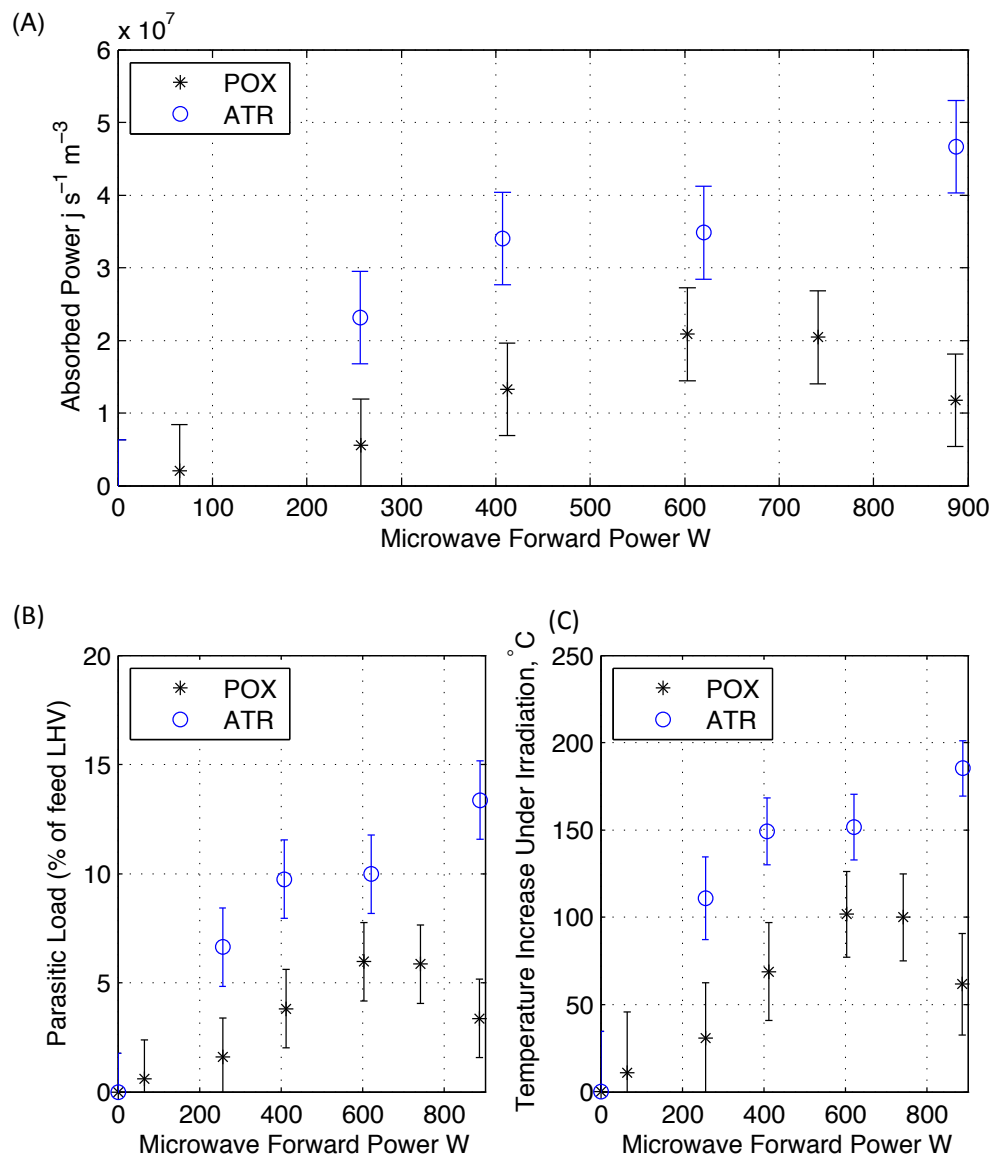


Figure 4.14: Comparison of model and experimental power absorption data. (A) Power absorbed by the experimental system used to obtain values of electric field strength. (B) Estimated parasitic load based on absorbed power as a fraction of LHV. (C) Model estimated catalyst exit temperature increase under irradiation.

Table 4.6: Temperature shift experienced by irradiated catalysts as measured by specified methods (Type of error reported).
 POX Conditions: 0 W Textit = 550 ±15 °C ATR Conditions: 0 W Textit = 573 ±21 °C.

Microwave Power Level, Watts (stdev)	IR Measured Temperature Shift, °C (stdev)	Furnace Effluent Comparison, °C (95%)	Furnace Carbon Comparison, °C (95%)	N ₂ Treated Carbon Comparison, °C (95%)	Water-Gas Shift Equilibrium, °C (N.A.)	Water-Gas Shift Equilibrium, Reforming Conditions, °C (95%)	Model Data Comparison, °C (95%)
POX:							
0 ± 2	0 ± 26	0 ± 39	0 ± 0	0 ± 60	0	0 ± 93	0 ± 35
65 ± 2	21 ± 25	39 ± 60	44 ± 50	113 ± 60	5	-27 ± 93	11 ± 35
257 ± 5	12 ± 25	135 ± 161	73 ± 83	187 ± 60	32	156 ± 93	31 ± 32
412 ± 19	-4 ± 70	168 ± 124	74 ± 84	188 ± 60	69	102 ± 93	69 ± 28
603 ± 14	-61 ± 115	190 ± 114	76 ± 86	193 ± 60	132	179 ± 93	102 ± 25
741 ± 17	35 ± 26	162 ± 83	72 ± 82	184 ± 60	191	119 ± 93	100 ± 25
886 ± 4	-69 ± 81	172 ± 84	71 ± 81	180 ± 60	264	165 ± 93	62 ± 29
ATR:							
0 ± 2	0 ± 63	0 ± 126	0 ± 0	0 ± 60	0	0 ± 85	0 ± 35
256 ± 8	154 ± 34	103 ± 68	81 ± 262	169 ± 60	32	2 ± 85	111 ± 24
407 ± 5	111 ± 90	107 ± 156	77 ± 248	160 ± 60	67	110 ± 85	149 ± 19
620 ± 12	147 ± 22	163 ± 87	95 ± 307	199 ± 60	139	177 ± 85	152 ± 19
887 ± 12	214 ± 29	196 ± 161	97 ± 315	203 ± 60	265	269 ± 85	185 ± 16

Considering all of the methods for estimating temperature change within an irradiated system, there remains significant uncertainty in the final values. Confidence intervals remain large due to scatter in experimental data that influences regressed parameters used for fitting. Error may be reduced by conducting additional experiments. Alternate methods may also be pursued to find other means of temperature estimation. Within a hydrocarbon processing system with very short contact times, thermal cracking models may be beneficial. Thermal cracking products are well established and models exist to predict product composition at given temperatures and residence times. Alternatively, there are a variety of reactions in which the kinetic regime of a lightoff curve may be used to understand the change in temperature under irradiation, in a similar way as the water-gas shift reaction was used in this work.

Multiple methods have been presented for estimating temperature change within an irradiated hydrocarbon reforming system subject to significant heat loss. Due to the inability to use conventional thermocouples and IR temperature measurement devices, a number of alternate means of temperature determination were developed and the error associated with each method reported.

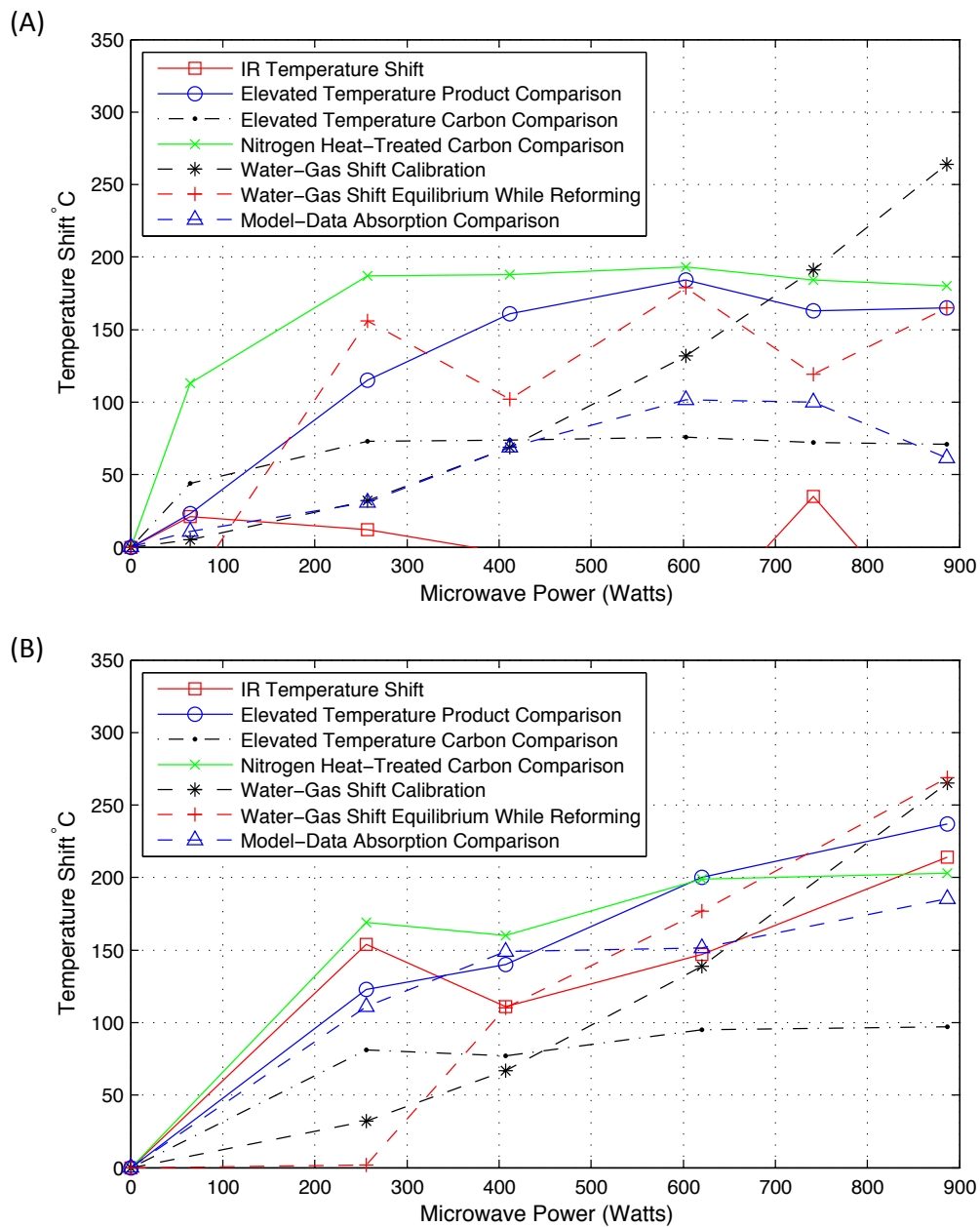


Figure 4.15: Summary of methods for determining temperature change within in irradiated catalyst system under POX (A) and ATR (B) conditions.

CHAPTER V

Conclusions

Within the body of this work, the influence of microwave-band irradiation on the performance of hydrocarbon reforming systems was investigated. Model systems consisting of monolith supported catalysts were irradiated while converting mixtures of propane, ethylene, water and air into hydrogen rich syngas. A novel high temperature microwave reaction system was constructed to enable the experiments described in this work. Chapter II examined conditions of partial-oxidation where only air and water were fed, as well as conditions of autothermal reforming where water is introduced into the feed. Microwave irradiation was found to effect changes in the product distributions and carbon deposited during reforming. Further comparisons between irradiated systems and samples exposed to elevated temperatures within a furnace demonstrated that not all observed changes duplicated within a furnace heated environment. Specifically, those alterations to coking behavior and product distributions that do not match furnace heated samples are termed microwave specific effects. Partial-oxidation experiments were used to demonstrate the similarity between furnace and microwave heating by operating under limited O_2 . The limited availability of O_2 greatly constrains operation and the absence of H_2O limits the endothermic energy demand in the downstream portion of the catalyst. Increasing the system temperature by microwave or furnace thus have very similar results.

Autothermal reforming experiments demonstrate a departure of the irradiated system from a traditional thermal behavior. Carbon deposition increases substantially with temperature in the furnace while remaining constant on the irradiated catalyst. Conversion of C_3H_8 indicates a much greater use of the feed and increased steam reforming activity when irradiated. CO_2 yield decreases with microwave power, consistent with the water-gas shift equilibrium at high temperatures and possibly due to the CO_2 oxidation of carbon deposits to produce additional CO. C_3H_6 also increases, consistent with increased oxydehydrogenation activity. Volumetric introduction of energy acts to raise the temperature of the downstream end of the catalyst, driving the steam reforming and water-gas shift reactions.

Chapter III expands upon the analysis of Chapter II by examining the impact of irradiation on sulfur poisoned catalysts operating under an autothermal reforming environment. Irradiation of a sulfur poisoned catalyst reduces the observed cracking and dehydrogenation products in the effluent while increasing syngas production. Exposure to microwave radiation does not appear to reverse poisoning, rather the volumetric introduction of energy into the downstream portion of the catalyst acts to promote the steam reforming and water-gas shift reactions. Comparison of carbon deposited while reforming in microwave and furnace heated environments demonstrates a clear advantage of microwave heating. Carbon couples strongly to the electro-magnetic field leading to greater catalyst heating and consequently more efficient preferential oxidation of carbon, thereby lessening carbon deposition on the catalyst. Samples exposed to elevated furnace temperatures coke significantly more as the temperature is increased due to greater production of coke precursors in the catalyst entrance region. Microwaves have been shown to favorably interact with active hydrocarbon reforming catalyst experiencing reduced syngas production due to sulfur poisoning. Carbon and coke deposition is eliminated and significant gains in syngas production are observed when irradiated. Volumetric heating of the catalyst increases steam re-

forming rates without additional coke precursor generation due to excessive entrance region temperatures experienced under elevated furnace temperature environments.

Within the body of this work, operation under microwave irradiation at high temperatures within a system of complex geometries prevented the accurate use of thermocouple or infrared temperature measurement devices. Information on the temperature of a catalytic system is essential to understand its operation and to correctly predict behavior. Within Chapter IV the following methods for the measurement of temperature within an electromagnetic field were discussed with respective error analysis:

- Thermocouple
- Infrared temperature measurement
- Comparison of effluent with equilibrium calculated compositions
- Comparison of irradiated samples to those run under elevated furnace temperatures
- Changes in carbon oxidation features
- Use of the water-gas shift equilibrium
- System modeling and model-data comparison

This work has confirmed that microwave frequency radiation can be used to selectively and volumetrically interact with a catalytic reforming system. Carbon was shown to interact in a favorable way, reducing coking under some conditions. Further, the activity of the system was altered to produce effects not observed in traditional thermal cases. The greatest beneficial effects of microwave heating are observed with the introduction of steam, increasing the endothermic energy demand and leading to greater syngas production than achievable by traditional furnace heating. Volumetric

heating appears most suited to applications with large endothermic energy requirements in structured catalysts where heat transfer limitations in the cool downstream region of the catalyst result in slow kinetics.

Microwave heating may be a viable alternative to inter-stage heating in a variety of endothermic reactions. Future work on this topic may examine one of several primary areas. Within hydrocarbon reforming systems, it would be beneficial to understand the specific source of the effects observed within this work. Research into the interaction of microwaves with the types of carbon deposited during hydrocarbon reforming may be of interest. It is conceivable that many endothermic reactions within structured catalysts may benefit from the volumetric introduction of energy due to their traditionally heat-transfer limited nature. The use of structured catalysts also introduces the possibility of designing a catalyst to absorb electromagnetic energy differentially along its length or radius based on the application of microwave absorbent materials within the catalyst.

APPENDICES

APPENDIX A

CO Oxidation on Pd/Al₂O₃: Kinetics in the Absence of Heat and Mass Transfer Effects

The following work is the result of a collaborative project with Ford Motor Company and is co-authored by Paul M. Laing* and Robert W. McCabe*.

*Chemical Engineering and Emissions Aftertreatment Department, Ford Research and Advanced Engineering, Dearborn, MI 48121, USA

Abstract

CO oxidation over supported noble catalysts, despite being one of the most highly studied catalytic reactions is fraught with contradictory kinetic data in the literature, largely owing to the difficulty of obtaining intrinsic kinetics in the absence of both washcoat and external phase heat and mass transfer effects. For automotive catalysts, where CO oxidation controls catalyst lightoff, it is important to enhance kinetics while minimizing pore diffusion effects in the monolith washcoat. We report for the first time, kinetics of CO oxidation over a model automotive monolith catalyst free of pore-diffusion effects. Data were obtained on a single-channel monolithic catalyst coated

with Pd/Al₂O₃. Pure chemical kinetics were obtained by operating with low CO concentrations at volumetric space velocities of ca 1.5 x 10⁶ h⁻¹ (STP), and by utilizing a small channel diameter, thin washcoat layer of wide-pore alumina, and low Pd loading. Reaction orders of roughly -1 (CO) and 1 (O₂) were observed, consistent with the literature. The apparent activation energy (127.9 ± 4.1 kJ mol⁻¹) was near values reported for the heat of adsorption of CO on Pd surfaces, consistent with Langmuir-Hinshelwood kinetics dominated by CO chemisorption. Measurements of turnover frequency (0.021 ± 0.003 @ 445 K) proved similar to literature values for experiments conducted with negligible heat and mass transfer influence. Additional experiments, conducted with powder samples of the same Pd/Al₂O₃ material, demonstrate the challenges of measuring kinetics in powder systems under automotive exhaust conditions. These results point out advantages of the single-channel monolith reactor for obtaining kinetics of fast, highly-exothermic catalytic reactions under conditions of negligible heat and mass transfer influence, and also provide guidance for designing fast lightoff automotive exhaust catalysts.

Introduction

CO oxidation over noble metal catalysts is one of the most highly studied reactions in heterogeneous catalysis, and also of great commercial and environmental significance due to its importance in automotive exhaust catalysis. With regard to the latter, Pd is currently the main component of three-way automotive catalysts (TWCs) utilized for CO and hydrocarbon oxidation, and is typically supported on alumina and/or ceria-containing support phases washcoated onto cordierite honeycomb monolith substrates. Interest in noble metal catalyzed CO oxidation has spanned the range from fundamental ultra-high vacuum studies of the surface reaction mechanism [121, 122, 123, 123, 124] to atmospheric pressure studies [125, 126, 127, 128, 129, 130, 131, 132, 133, 134] focused mostly on experimental and theoretical analysis of

the more complex manifestations of its reaction kinetics (such as rate oscillations, hysteresis, and steady-state rate multiplicities) resulting from coupling of surface reaction kinetics with heat and mass transfer effects. A number of reviews have been published covering the full range of CO oxidation studies on noble metal catalysts.

Focusing on Pd specifically, a significant body of work has examined CO oxidation under UHV conditions where surface structures can be well-characterized and coverages of reactant species can be readily controlled and monitored. UHV experiments have provided insight into differences in reactivity between different crystallographic orientations including differences between terrace and low-coordination sites [127, 135, 136]. Within this body of work, a wide range of reaction activation energies have been reported (60 - 123 kJ mol⁻¹) along with differing reaction orders in CO and O₂ [127, 129, 123, 124]. The most important aspect of CO oxidation under the higher pressure conditions of automotive three-way catalysis is its well-known inhibition of catalyst lightoff, the temperature range over which the catalyst transitions from its cold, inactive state to its fully active warmed up operating condition. Oxidation of CO at moderate to high pressures and low temperatures is characterized by nearly complete coverage of noble metal sites by chemisorbed CO. As a result of high CO coverage, the measured reaction activation energy, E_a , will approach the value for ΔH_{ads} under conditions of near complete CO surface coverage. CO adsorption is strong on the noble metal surfaces with values for ΔH_{ads} of CO on Pd ranging from 100 - 145 kJ mol⁻¹ with most values reported in the range of 121 - 142 kJ mol⁻¹ [137, 138, 139, 127, 123]. As such, CO oxidation is characterized by Langmuir-Hinshelwood kinetics over several orders of magnitude in pressure [140]. Mechanistically, CO oxidation occurs catalytically on noble metals via the adsorption of CO and O₂ and the subsequent dissociation of adsorbed O₂* (possibly assisted by CO*) before reacting to form CO₂ [131, 130]. CO is inhibitory in the system [141] and O* diffusion is rapid compared to the rate of reaction [127]. Overall reaction rates are

generally agreed to be first-order in O_2 and inverse first-order in CO [123, 140, 131]. As the catalyst temperature increases above 390 K, the CO coverage decreases, accompanied by a corresponding though smaller increase in O coverage [142, 129]. The surface coverage, however, of O-atoms remains low at low O_2/CO ratios [129].

Taking these effects together, catalyst lightoff in CO-containing gas mixture such as automotive exhaust is typically thought of as consisting of a low-temperature “kinetic” regime, followed by an intermediate temperature regime with rates influenced by pore diffusion as well as chemical kinetics, and finally, a high temperature regime dominated by rates of external phase mass transfer. These “controlling” regimes have been studied in detail for H_2 oxidation on model Pt/ Al_2O_3 monolithic catalysts by Joshi et al. [143]. A significant finding from that study was the inability to completely isolate the intrinsic kinetics from washcoat diffusion effects for the extremely fast Pt-catalyzed H_2 oxidation reaction, despite utilizing space velocities in excess of 1×10^6 h^{-1} . The observations of the Joshi et al. study point out a flaw (or at least a confounding factor) in the typical evaluation methods for automotive exhaust catalysts [143]. Catalysts are commonly characterized by their so-called lightoff temperature, i.e., the temperature at which the conversion of CO and other exhaust species reaches a specific level, e.g., T(50%) or T(80%). These temperatures usually coincide with a fast rise in conversion across a narrow temperature range associated with the mixed regime of reaction rate influenced by intrinsic kinetics, washcoat diffusion, and external phase mass transfer, thus making it unclear to what extent kinetic factors (e.g., metal loading and dispersion, surface reaction rates) versus diffusion related factors (e.g., washcoat thickness and mean pore dimensions, monolith channel diameter) contribute to the observed conversions. Add to this the challenge of transferring heat quickly to the catalyst for fast lightoff, and it becomes clear that the lightoff temperature provides little guidance on the optimal design of a monolithic automotive exhaust catalyst.

The goal of the present study was to measure CO oxidation kinetics on monolithic Pd/Al₂O₃ catalysts in the absence of heat and mass transfer effects on the observed rates, thereby gaining insight into the relative importance of intrinsic kinetics versus heat transfer and diffusional effects across the temperature range of catalyst lightoff. Experiments were designed to measure intrinsic CO oxidation kinetics under conditions simulating automotive exhaust catalysis. Our results confirmed that intrinsic kinetics could indeed be measured by following the basic approach utilized by Joshi et al. [143], but taking advantage of the inherently slower kinetics of CO oxidation and making further modifications to the catalyst to minimize pore diffusional resistances in the washcoat layer. In addition, we found that corresponding intrinsic kinetic measurements could not be made on powder catalyst samples due to prohibitive pressure drop across the catalyst bed at the very small catalyst particle sizes and high flow rates that would be required to maintain a negligible increase in intra-particle temperatures, relative to bulk gas temperatures.

Experimental

Catalyst preparation

For the purposes of this study, reaction conditions were manipulated to minimize the effects of mass transfer limitations and reaction exotherm upon the measurement of kinetic parameters. Two catalyst supports were chosen to examine the effect of pore structure on measured rates, with the ratio of Palladium mass to support surface area preserved to maintain equivalent crystallite size and dispersion across samples. The two Aluminas chosen were Sasol TH100/150 alumina, similar to those commonly used in automotive washcoat applications, and Sasol TH500 made from the same precursor, but with a much lower specific surface area and larger mean pore diameter.

Catalysts were prepared in single batches of 0.7 wt.% Pd on TH100/150 alumina

and 0.2 wt.% Pd on TH500 alumina via incipient wetness impregnation with similar loadings used industrially. All aluminas were thermally stabilized at a temperature of 800 °C for 3 hours in air before impregnation with an aqueous solution of Pd(NO₃)₂·6H₂O. The catalyst precursor was then dried at 100 °C for 1 hour before calcination in air 1 hour at 750 °C. Calcination temperatures were chosen to exceed those subsequently experienced during reaction, thermally stabilizing the material.

Substrate supported catalysts consisted of the Pd-alumina catalyst material described previously washcoated onto blank cordierite monoliths (900 cpsi, 2.5 mil, Corning). Washcoat slurries were made by sieving catalyst material (5.0 g) to less than 120 mesh (125 μm), and, combining with Hydroxyethylcellulose (0.17 g), Ammonium Polyacrylate (0.17 g) and DI H₂O (28.3 g). This mixture was placed in a 150 ml polypropylene bottle along with 150 g of 5 mm diameter zirconia grinding media. The mixture was ball-milled for 30 minutes followed by material recovery and addition of Acetic Acid to produce a 1 M solution. SEM analysis of the washcoat was used to find the minimum milling time required to reduce the catalyst material to less than 10 μm. Monoliths were cut to size before brief immersion in stirring washcoat slurry (20 wt.% solids) and subsequent clearing of channels with compressed air. Samples were dried for 30 minutes at 100 °C followed by 20 minutes at 550 °C. Washcoat loading was verified by weight and the coating process repeated until the desired loading was achieved, followed by a final calcination at 600 °C for 20 minutes. Throughout the study no loss of washcoat adhesion was observed.

Flow reactor description

Experiments were carried out in a vertically mounted furnace in a down flow configuration. Gases were supplied through a series of mass flow controllers (Matheson), using Airgas primary standard grades of 1.00% CO in N₂, 1.00% O₂ in N₂, 5.00% H₂ in N₂ and UHP N₂. A carbonyl trap consisting of alumina heated to 140 °C was

employed on the CO feed to prevent contamination. Analysis was performed using a low range CO analyzer (Horiba 0-1,000ppm) and computer data logging software. A UEGO sensor was employed to check the oxidation/reduction ratio of the feed. Two thermocouples were utilized for data logging; one positioned immediately above the catalyst and a second immediately below. Quartz thermowells were used with 1/16" thermocouples in 1/4" wide bore tubes. Narrow bore tubes necessitated the use of 1/32" thermocouples without quartz sheathing. Blank runs with exposed stainless steel showed less than 0.5% conversion at 500 °C.

Reaction conditions

Prepared catalysts were tested for the oxidation of CO under conditions of high flow and low concentrations to minimize heat buildup and diffusional limitations in the system. Unless otherwise noted, a gas hourly space velocity of 1,500,000 ($\text{cm}^3_{\text{gas}} \text{cm}^{-3}_{\text{catalyst}} \text{hr}^{-1}$) was used with a CO concentration of 500 ppm and O₂ concentration of 257 ppm. An O/CO ratio of 1.03 was chosen to ensure complete combustion of CO while mimicking slightly lean conditions observed in automotive applications.

Monolith supported catalysts prepared for this study are listed in Table A.1. For each base catalyst material, a high and low level of washcoat was used to probe diffusional resistance. For reference, a typical automotive application will use washcoat loadings in excess of 1.5 g in⁻³. As many kinetic studies are performed on powders, GHSV by weight is reported for each condition. Flux of CO, normalized by the number of available surface Pd sites as determined by chemisorption provided in Table A.1, provides a logical upper bound on measured TOFs.

Experiments were performed under constant flow conditions at a ramp rate of 5 °C min⁻¹ from room temperature to 400 °C followed by a 1 minute dwell and a 5 °C min⁻¹ return to room temperature. System pressure remained under 2 psig at all times. Results are reported in fractional conversion and turnover frequency.

Table A.1: Reaction flow conditions at 1,500,000 GHSV over selected Pd/Al₂O₃ catalysts.

Catalyst	Washcoat Loading wt.% [g in ⁻³]	GHSV (cm ³ g _{cat} ⁻¹ hr ⁻¹)	CO Flux: mol-CO mol-Pd _{surface} ⁻¹ s ⁻¹
0.7wt.%Pd Th100/150	4.0% [0.27]	124,000,000	80.8
0.7wt.%Pd Th100/150	26.6% [1.72]	14,000,000	9.3
0.21wt.%Pd TH500	3.4% [0.17]	147,000,000	289.3
0.21wt.%Pd TH500	25.4% [1.62]	15,000,000	28.75

Activation energy is determined by linearizing the rate equation using data over conversions of 0.5 - 6.0%. Residuals were observed for signs of trending indicating a poor fit and 5 - 10 repeats were performed to assure consistency of results. Where possible, 95% confidence intervals are reported on regressed parameters. Reaction orders in CO and O₂ were determined by minimizing error between model-calculated rates and experimental rate data taken at a constant temperature and varying the concentration of CO and O₂. Experiments were repeated forward and backward with good agreement between repeats and no apparent hysteresis.

Catalyst characterization

Physical surface area measurements were performed via multi-point BET on a Micromeritics ASAP2040 instrument using N₂ adsorption at 77.3 K and relative pressures of 0.052 - 0.304, post 350 °C degas for 1 hour. Metallic surface area and dispersion measurements were performed by H₂ chemisorption using a Micromeritics ASAP 2020 instrument. Samples were degassed under vacuum at 300 °C, followed by reduction in flowing H₂ at 600 °C. Measurements were taken at 35 °C, obtaining two complete isotherms to determine the quantity of strongly adsorbed hydrogen, thereby calculating the number of exposed metallic sites. Arrhenius rate parameters were obtained assuming a first-order reaction in O₂ and inverse first-order in CO.

Table A.2: Surface area and dispersion results for Pd/Al₂O₃ catalysts.

Sample	Surface Area m ² g ⁻¹	Dispersion %
TH100/150	116.7	
TH100/150 0.7 wt.% Pd	114.8	14.4
TH500	37.0	
TH500 0.21wt.% Pd	35.5	16.5

Results

Catalysts were analyzed for their physical and metallic surface areas reported in Table A.2. Both catalysts achieved similar dispersions, with H₂ uptake scaling in proportion to Pd weight loading. Compared with dispersions achieved from a nitrate precursor reported elsewhere [144, 128], this study maintained a relatively high dispersion despite calcining the sample at 750 °C. Higher dispersions may be obtained by use of alternate precursors such as palladium chloride or acetylacetonate.

Figure A displays the conversion curves and TOF plots for high and low washcoat loadings of the two representative catalysts. It is significant to note that despite over an order of magnitude difference in the number of exposed Pd surface atoms, the TOF curves agree well at low conversion. Ordering of the conversion curves also follow the expected order of most to least exposed Pd sites present and TOF values asymptotically approach the feed CO flux per Pd site. Activation energies across samples were found to be in close agreement with a value of $E_a = 127.9 \pm 4.1 \text{ kJ mol}^{-1}$ (95% confidence interval).

Reaction orders with respect to CO and O₂ were determined by varying the reactant concentrations and measuring the steady state rate at low conversion and constant temperature ($264 \pm 1 \text{ °C}$). The reaction rate was monitored at concentrations of 250 - 1,000 ppm CO and 128 - 515 ppm O₂ at 1,500,000 GHSV. Oscillatory reaction behavior on the timescale of several seconds was observed under conditions of 500 ppm CO and 515 ppm O₂ with measured CO concentration deviations of ± 30 ppm CO. Oscillations in CO oxidation have been well described in literature [145, 146, 147].

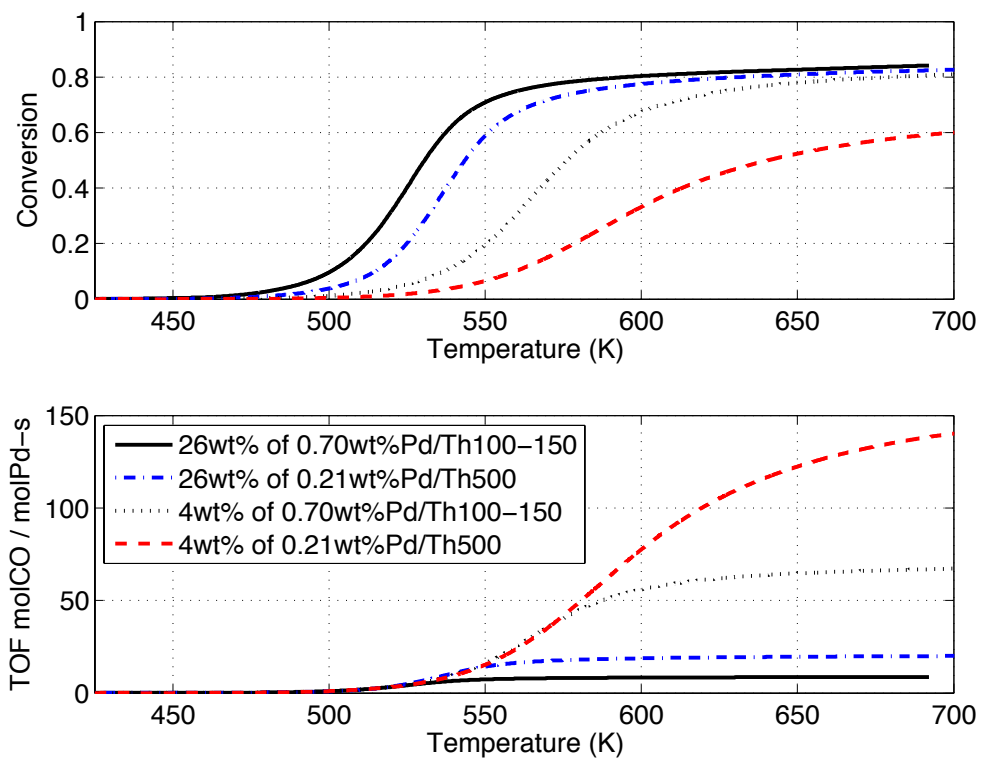


Figure A.1: (Top) Conversion curves for high and low washcoat loadings of the two representative catalysts used. (Bottom) TOF data for the respective catalysts. GHSV of 1,500,000 ($\text{cm}^3_{\text{gas}} \text{cm}^{-3}_{\text{catalyst}} \text{hr}^{-1}$), 500 ppm CO, 257 ppm O_2 .

Table A.3: Activation energy for the oxidation of CO over Pd.

Reference:	System:	Ea (kJ mol ⁻¹)
This Study	Pd/Al ₂ O ₃	127.9 ± 4.1
Kieken 1993 [125]	Pd/Al ₂ O ₃	107
Landry 1990 [126]	Pd/Al ₂ O ₃	112
Hoffman 2002 [127]	Pd/Al ₂ O ₃	60
Berlowitz 1988 [121]	Pd(110)	109
Logan 1992 [122]	Pd(100)	113
Szanyi 1994 [123]	Pd(100)	122.9
Szanyi 1994 [148]	Pd(111)	117.5
Engel 1978 [124]	Pd(111)	104.5
Wang 2010 [128]	Pd/SiO ₂	98.4 - 133.8
Xu 1993 [129]	Pd/SiO ₂	96.1 - 112.9
Wang 2010 [128]	Pd/SiO ₂	36.7

Oscillatory behavior was not observed at any other conditions, however due to the analyzer used in this study, short timescale fluctuations are not observable. An Arrhenius kinetic model was used in data analysis to correct for slight (± 2 °C) variation in temperature between measurements. Overall reaction order was determined to be first order in O₂ and inverse first order in CO, consistent with those established in other non-UHV experimental settings. Results are consistent with a system where CO coverage remains high at low conversions, limiting the rate of reaction.

Discussion

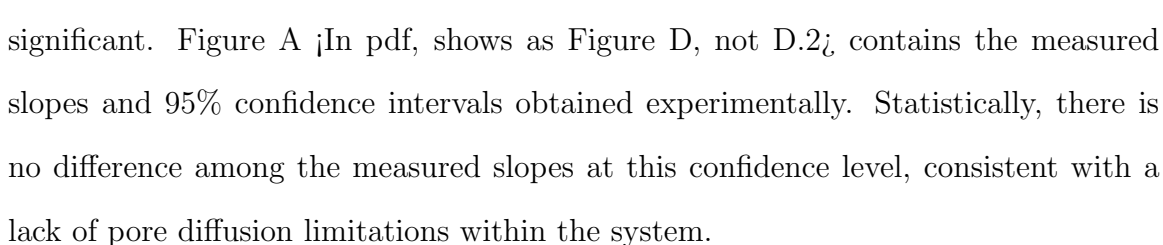
Kinetic analysis of fast and highly exothermic reaction systems such as H₂ and CO oxidation are frequently plagued by issues of slow mass transfer and heat buildup within particles. To gain insight into the relative significance of these phenomena, several dimensionless groupings may be beneficial.

Activation energies obtained for the oxidation of CO are presented in Table A.3. Significant disagreement exists among reported values, highlighting the difficulty in obtaining accurate kinetics in this system. Results of this study are on the higher end of reported values, consistent with obtaining kinetic parameters at high temperatures.

Table A.4: TOF values for the oxidation of CO over Pd systems.

Reference:	System:	Temp. K	TOF:
This Study	Pd/Al ₂ O ₃	445	0.021 ± 0.003
Kieken 1993 [125]	Pd/Al ₂ O ₃	445	0.03
Landry 1990 [126]	Pd/Al ₂ O ₃	445	0.035
Logan 1992 [122]	Pd(100)	445	0.036
Berlowitz 1988 [121]	Pd(110)	445	0.033
Szanyi 1994 [123]	Pd(100)	445	0.15
Szanyi 1994 [148]	Pd(111)	445	0.09
This Study	Pd/Al ₂ O ₃	450	0.032 ± 0.004
Ladas 1981 [137]	Pd/Al ₂ O ₃	450	0.012 ± 0.005
Matsushima 1976 [141]	Pd/SiO ₂	450	0.030 ± 0.030

Turnover values are reported in Table A.4 for Pd, CO oxidation systems at 445 and 450 K. Results of this study are in agreement with those reported elsewhere.

Among the various controlling regimes in CO oxidation, the measurement of diffusion within the washcoat is generally the most challenging to ascertain with any degree of certainty. Diffusion within the washcoat when operating in a washcoat limited regime can be related to the slope of the conversion vs. temperature curve through intermediate values of conversion. Weisz-Prater parameters were calculated for high and low washcoat loadings of 0.7 wt.% Pd TH100/150 catalysts in Table A.5. Based on this analysis, no significant pore diffusional limitations are expected within the various samples. Experimentally, this was confirmed by observing the slope of the conversion vs. temperature curve for similar samples (2 wt.% and 25 wt.% washcoat) over a defined range of $X = 0.45 - 0.55$ where, pore diffusion effects are deemed significant. Figure A  contains the measured slopes and 95% confidence intervals obtained experimentally. Statistically, there is no difference among the measured slopes at this confidence level, consistent with a lack of pore diffusion limitations within the system.

One shortcoming of the above method for determining the impact of washcoat diffusion limitations is the comparison of conversion curve slopes obtained at different temperatures. To more accurately compare samples with significantly different

Table A.5: Weisz-Prater parameter at 540 K. Systems are considered to be free of diffusion limitations when $\Phi \ll 1$.

Sample:	Weisz-Prater Parameter: Φ
4 wt.% of 0.70 wt.% Pd TH100/150	0.09
26 wt.% of 0.70 wt.% Pd TH100/150	0.21

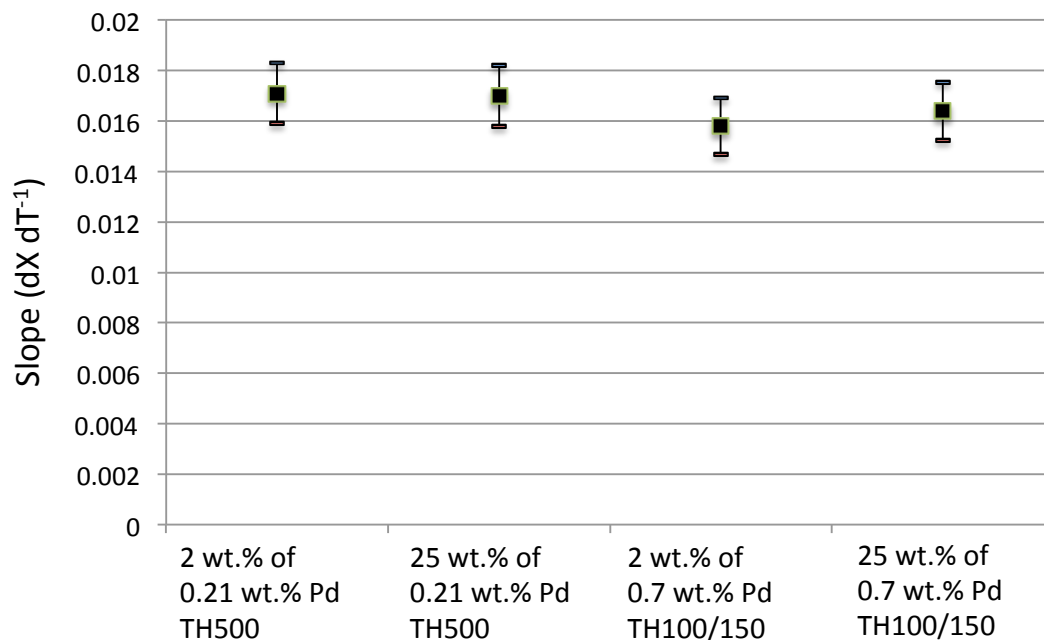


Figure A.2: Slope of the conversion vs. temperature curve for samples over a defined range of $X = 0.45 - 0.55$. GHSV of 1,500,000 ($\text{cm}^3_{\text{gas}} \text{cm}^{-3}_{\text{catalyst}} \text{hr}^{-1}$), CO concentration of 500 ppm and O_2 concentration of 257 ppm.

Table A.6: Catalysts used for aligning conversion curves over different washcoat thicknesses: 0.7 wt.% Pd TH100/150 catalyst material.

Washcoat loading	Blank Alumina / Catalyst dilution ratio	Catalyst mass
8.8 ± 0.5 wt.%	0 / 1	0.00728 g
45 ± 5 wt.%	7.3 / 1	0.00681 g

loadings of precious metal and washcoat requires aligning the light off of those samples; else the Arrhenius nature of the change in rate with temperature dominates. To accomplish this, samples were produced with identical loadings of catalyst, but with varying levels of washcoat by using blank alumina as a filler. Samples listed in Table A.6 were run under conditions of 500 ppm CO, 257 ppm O₂ and a CO flux of 4,110 mol-CO per surface mol-Pd per second with a 9 cell (3 by 3) monolith sample 1" long. Light off curves for the samples listed in Table A.6 are shown in Figure A. The observed difference in high temperature conversion can be partially accounted for by the slight difference in catalyst loading, however even on a TOF basis, there remain differences in the bulk mass transfer limit that will propagate into measurements of the washcoat diffusion regime slope. Increased bulk mass transfer limitations are suspected to result from increased backpressure in the thick washcoat sample, causing an increase in bypass of the primary sample channels. At this point, further experiments with a modified system design are necessary to obtain more precise experimental measurements. An alternative to additional experiments is the greater use of modeling tools to capture the bypass behavior and use the existing experimental results to understand washcoat parameters. Due to time constraints, further experimental work on this avenue of study was not completed.

High space velocities have been utilized in this study as a means to push CO light off to higher temperatures than are typically studied. Use of high space velocities also introduces additional mass transfer limitations in the form of an upper bulk mass transfer limit illustrated in Figure A.4 for a first order system. Bulk mass transfer limitations primarily influence the system behavior at high temperatures, however

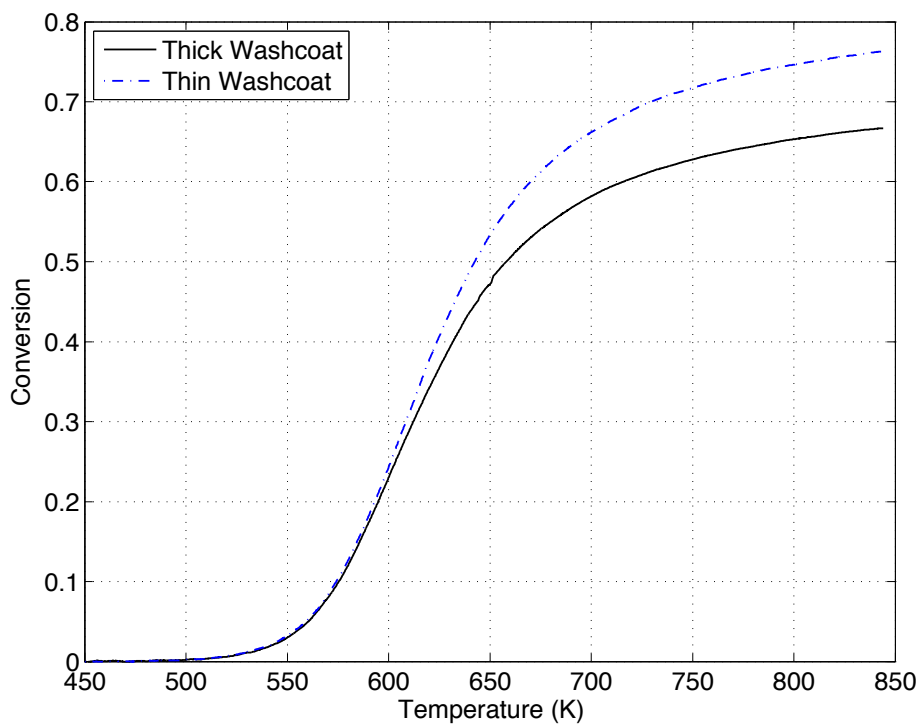


Figure A.3: Conversion curves for samples with similar catalyst loadings and differing washcoat thicknesses at $1,500,000 \text{ (cm}^3_{\text{gas}} \text{ cm}^{-3}_{\text{catalyst}} \text{ hr}^{-1})$, 500 ppm CO and 257 ppm O₂. Thick and thin washcoat loadings are $45 \pm 5 \text{ wt.}\%$ and $8.8 \pm 0.5 \text{ wt.}\%$ respectively.

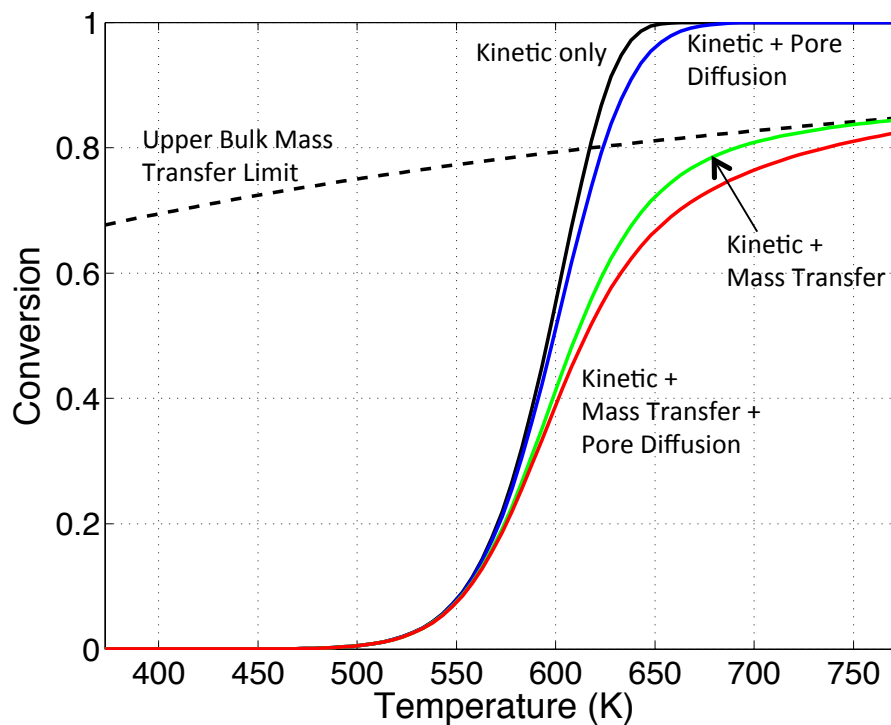


Figure A.4: Sample conversion curves for a first-order system demonstrating the effects of various mass transfer limitations on conversion curves: generated by Paul Laing.

the effects of bulk mass transfer also influence the kinetic regime. Modeling by Paul Laing at Ford Motor Company was used to quantify the effect of bulk mass transfer limitations on measured activation energies in systems similar to those being studied. Bulk mass transfer limitations in monolith systems were found to decrease the measured E_a by 2.6 %, well within the uncertainty of measurement for the experimental system.

Conclusions

Measurements of reaction kinetics for the fast and highly exothermic oxidation of CO have been successfully performed in a monolith based system, where the effects of mass transfer limitations have been minimized to within the experimental error of measured parameters. Activation energies and turnover frequencies are in general

agreement with those reported in literature and the reaction order was found to be consistent with high CO surface coverage, even at high temperatures. Initial results examining the impact of pore diffusion within the washcoat indicate little to no effect of washcoat thickness or alumina type on system performance. Additional experiments and analysis are required to gain a more full understanding of the impact of washcoat thickness and composition on catalyst lightoff and operation.

Acknowledgements

I would like to acknowledge the support of Ford Motor Company and the many wonderful individuals within the Research and Innovation Center that made this work possible. In particular, Paul Laing and Robert McCabe were wonderful supervisors, collaborators and mentors, teaching me much about automotive emissions control.

APPENDIX B

Technology Disclosures and Patents

Initial research into the use of microwave frequency radiation to influence catalytic systems led to the declaration of 3 University of Michigan technology disclosures around the interactions of microwaves with catalytic reforming systems. Those disclosures were titled:

- Process using Microwave energy to remove carbon from the surface of a reforming catalyst
- Microwave Assisted NO_x Abatement
- Process using microwave energy to remove sulfur from a reforming catalyst

Based off of the above disclosures, the filing of a patent application Use of Microwave Energy to Remove Contaminating Deposits from a Catalyst was pursued and is pending [US 2011/0118105 A1]: [149]. Figure B.1 shows the first page of the patent.

Figure B.1: Patent Application: Use of Microwave Energy to Remove Contaminating Deposits from a Catalyst US 2011/0118105 A1.

(19) **United States**

(12) **Patent Application Publication**
Schwank et al.

(10) **Pub. No.: US 2011/0118105 A1**

(43) **Pub. Date: May 19, 2011**

(54) **USE OF MICROWAVE ENERGY TO REMOVE CONTAMINATING DEPOSITS FROM A CATALYST**

Publication Classification

(51) **Int. Cl.**
B01J 38/12 (2006.01)
B01J 19/08 (2006.01)
H01M 8/10 (2006.01)
B01J 38/04 (2006.01)
B01J 38/10 (2006.01)
 (52) **U.S. Cl.** 502/38; 422/186; 429/479; 502/34; 502/53

(75) **Inventors:** Johannes Schwank, Ann Arbor, MI (US); Steven Edmund, Whitmore Lake, MI (US)

(73) **Assignee:** The Regents of the university of Michigan, Ann Arbor, MI (US)

(57) **ABSTRACT**

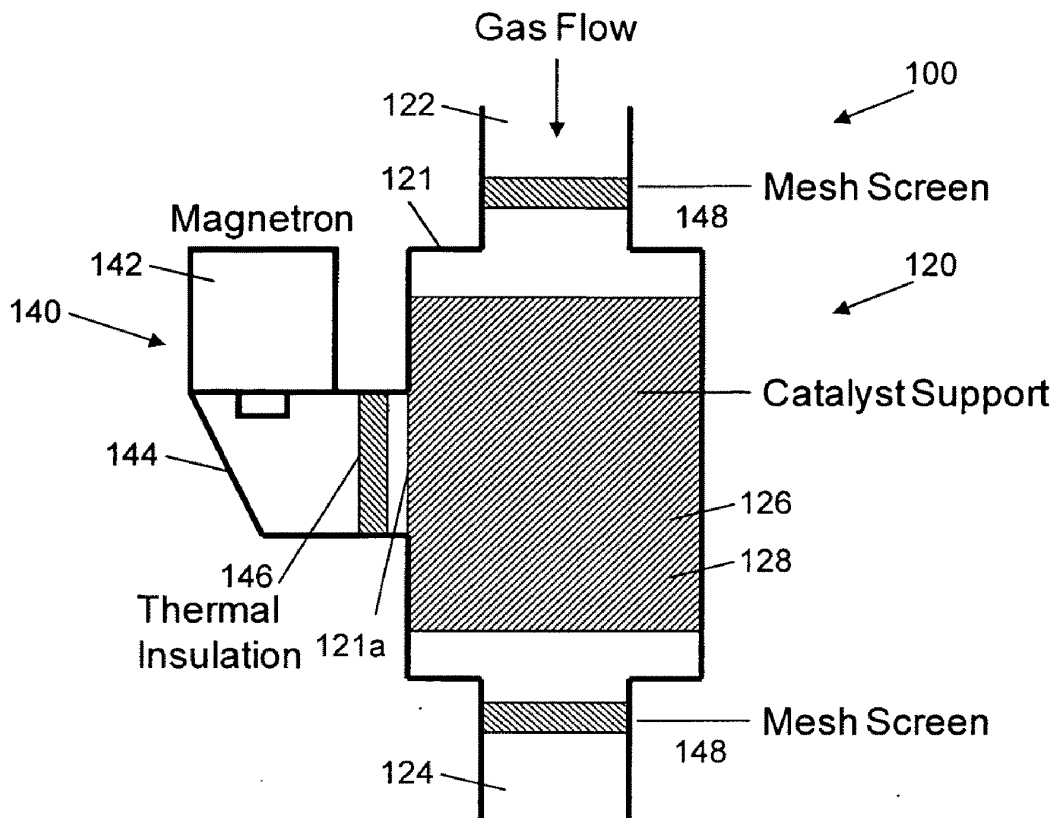
The disclosure relates to apparatus, systems, and methods (a) for performing catalytic reactions using a fixed-bed catalyst (e.g., packed particulate bed or catalyst supported on a monolithic substrate) and (b) for regenerating the catalytic activity of the catalyst. An autothermal reformation (ATR) reaction system is described for illustrative purposes, although the apparatus, systems, and methods can be applied more generally to other catalytic cracking/reformation reaction systems and other catalytic reaction systems, in particular reaction systems in which carbon-based and/or sulfur-based catalyst contaminants are produced during system operation.

(21) **Appl. No.:** 12/927,526

(22) **Filed:** Nov. 17, 2010

Related U.S. Application Data

(60) Provisional application No. 61/262,239, filed on Nov. 18, 2009.



APPENDIX C

Mass Spectrometer Calibration

As described in section 2.2.6, an online Mass Spectrometer (MS) was utilized to obtain information on the concentrations of species exiting the reactor system. Mass spectra were obtained over a range of $m/z = 1:50$, this data was then combined with an adaptive spectral deconvolution program to obtain mass fractions of H_2 , H_2O , O_2 , N_2 , CH_4 , C_2H_2 , C_2H_4 , C_2H_6 , C_3H_6 , C_3H_8 , CO , CO_2 , and Ar in the effluent. Electron ionization mass spectrometers can be difficult to calibrate due to the tendency for the sum of the ionization intensities to change based on changes in gas composition, leading to a non-unity sum of mole fractions. Another more difficult challenge to address is the overlap in spectra of the various species to obtain relative ionization intensity values (the relative number of ions generated for each species entering the MS). Figure C.1 is the electron ionization mass spectra from NIST for the aforementioned species, assigning each a relative intensity of 1,000 for the major peak [97, 95]. Relative electron ionization intensities were obtained by combining the NIST spectral data with experimental mass spectra for a known gas composition similar to that expected from the reactor. A constrained matrix optimization routine was used to find the values of relative ionization intensity that combined with the NIST data and known mole fractions could reproduce the experimental mass spectra. Table C

Table C.1: Relative Ionization Intensities obtained for this study.

Species	Relative Intensity
Hydrogen	10.6
Water	96.6
Methane	63.1
Oxygen	85.0
Nitrogen	48.2
Ethane	376.4
Ethylene	156.5
Propane	125.0
Propylene	24.4
Carbon Monoxide	230.0
Carbon Dioxide	40.0
Argon	50.0
Acetylene	40.0

provides the relative ionization intensities obtained and used in this study. Once the relative ionization intensities are known the inverse matrix operation is performed to obtain mass fractions for the effluent gas given the relative ionization intensities, NIST data and experimental mass spectra. Results were monitored for poor fitting by tracking residuals for each m/z .

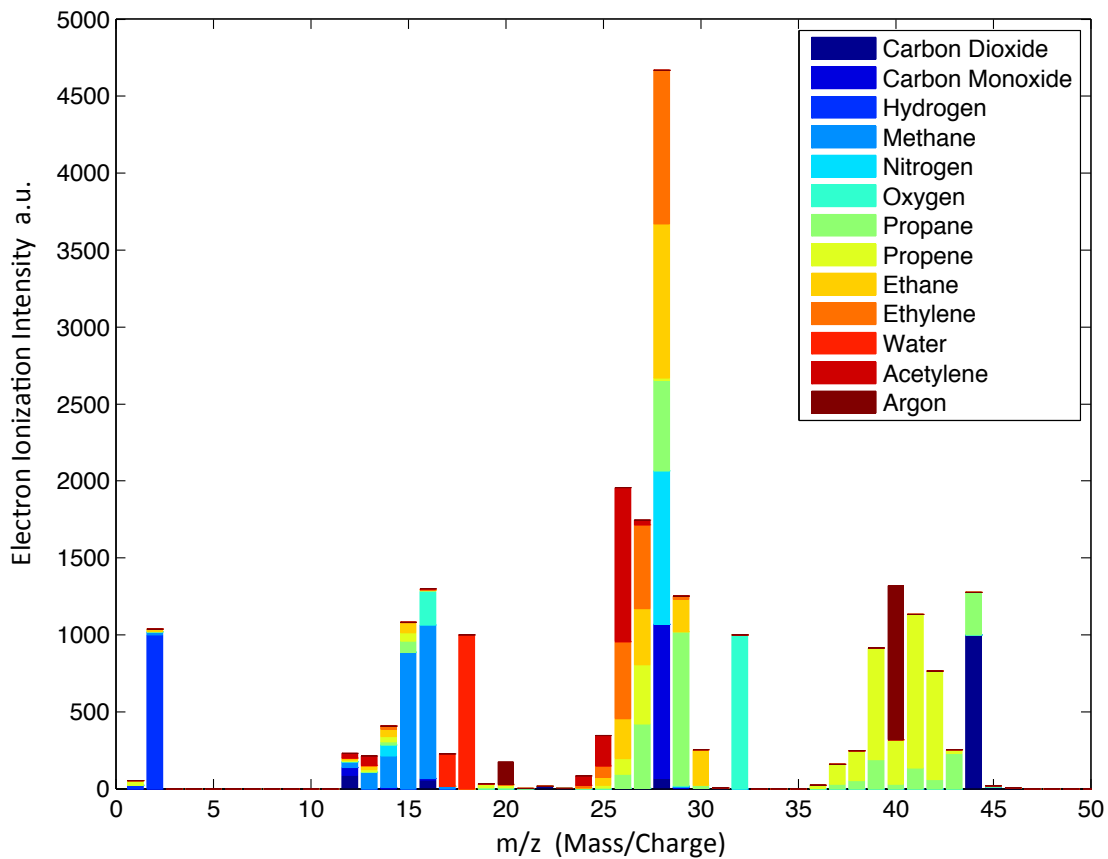


Figure C.1: Electron Ionization Mass Spectra data from the NIST Chemistry Database. Primary peak for each species is scaled to 1,000 a.u.

APPENDIX D

Experimental Error Analysis

Unless otherwise noted, all experiments have been verified by repetition of procedure to assure the validity of results. Error analysis on reported mole fractions, yields and conversions are calculated by Standard Error ($SE_{\bar{x}}$) between sample results as well as by propagation of error, with the greater of the two values reported. The equation used to calculate $SE_{\bar{x}}$ is given in Equation (D.1) where \bar{x} is the mean value, x is the sample value and n the sample size.

$$SE_{\bar{x}} = \frac{\sqrt{\sum(x - \bar{x})^2}}{n} \quad (\text{D.1})$$

Propagation of error was performed using the standard method outlined by D. Harris [150], examining the sources of error that could contribute to observed differences in reported mole fractions, yields and conversions. Table D.1 contains the values for error from the various contributing sources. Assuming a linear relationship between the described variables as a first approximation, total error on a measured mole fraction is $\pm 7.4\%$ of the measured value. The corresponding error for yields and conversions are $\pm 7.8\%$.

Table D.1: Propagation of error: Contribution of error from reactor system components.

Contributing Process:	Error \pm	Source of error:
Gas Mass Flow Controllers (rate)	$\sqrt{3}\%$	3 flow controllers at $\pm 1\%$ each
Liquid Flow Controller (rate)	2%	Dispensing uncertainty
Catalyst Sample Weight	3.2%	Variation across monoliths
MS concentration	6.1%	Error in spectral deconvolution

BIBLIOGRAPHY

BIBLIOGRAPHY

- [1] Annual Energy Outlook 2012. Technical report, Energy Information Administration, 2012.
- [2] T. Friedman. *Hot, Flat, and Crowded: Why We Need a Green Revolution And How It Can Renew America*. Farrar, Straus and Giroux, New York, 2008.
- [3] S. Jain, H. Chen, and J. Schwank. Techno-economic analysis of fuel cell auxiliary power units as alternative to idling. *Journal of Power Sources*, 160(1):474, 2006.
- [4] K. Damen, M. Troost, A. Faaij, and W. Turkenburg. A comparison of electricity and hydrogen production systems with CO₂ capture and storage. Part A: Review and selection of promising conversion and capture technologies. *Progress in Energy and Combustion Science*, 32(2):215, 2006.
- [5] C. Athanasiou, F. Coutelieres, E. Vakouftsi, V. Skoulou, E. Antonakou, G. Marnellos, and A. Zabaniotou. From biomass to electricity through integrated gasification/SOFC system-optimization and energy balance. *International Journal of Hydrogen Energy*, 32(3):337, 2007.
- [6] N. Darwish, N. Hilal, G. Versteeg, and B. Heesink. Feasibility of the direct generation of hydrogen for fuel-cell-powered vehicles by on-board steam reforming of naphtha. *Fuel*, 83(4-5):409, 2004.
- [7] C. Wheeler, A. Jhalani, E. Klein, S. Tummala, and L. Schmidt. The water-gas-shift reaction at short contact times. *Journal of Catalysis*, 223(1):191 – 199, 2004.
- [8] R. Horn, N. Degenstein, K. Williams, and L. Schmidt. Spatial and temporal profiles in millisecond partial oxidation processes. *Catalysis Letters*, 110(3-4):169–178, 2006.
- [9] M. Barsan and F. Thyron. Kinetic study of oxidative dehydrogenation of propane over Ni-Co molybdate catalyst. *Catalysis Today*, 81(2):159–170, 2003.
- [10] K. Sundaram and G. Froment. Modeling of thermal cracking kinetics - 3. Radical mechanisms for the pyrolysis of simple paraffins, olefins, and their mixtures. *Ind Eng Chem Fundam*, 17(3):174 – 182, 1978.

- [11] V. Choudhary, V. Rane, and A. Rajput. Simultaneous thermal cracking and oxidation of propane to propylene and ethylene. *AIChE Journal*, 44(10):2293–2301, 1998.
- [12] M. Bettahar, G. Costentin, L. Savary, and J. Lavalley. On the partial oxidation of propane and propylene on mixed metal oxide catalysts. *Applied Catalysis A: General*, 145(12):1–48, 1996.
- [13] M. Berreni and M. Wang. Modeling and dynamic optimization of thermal cracking of propane for ethylene manufacturing. *Computers & Chemical Engineering*, 35(12):2876–2885, 2011.
- [14] R. Horn, K. Williams, N. Degenstein, A. Bitsch-Larsen, D. Nogare, S. Tupy, and L. Schmidt. Methane catalytic partial oxidation on autothermal Rh and Pt foam catalysts: Oxidation and reforming zones, transport effects, and approach to thermodynamic equilibrium. *Journal of Catalysis*, 249(2):380–393, 2007.
- [15] K. Hardiman, C. Cooper, A. Adesina, and R. Lange. Post-mortem characterization of coke-induced deactivated alumina-supported CONi catalysts. *Chemical Engineering Science*, 61:2565–2573, 2006.
- [16] C. Bartholomew. Mechanisms of catalyst deactivation. *Applied Catalysis A: General*, 212(1-2):17, 2001.
- [17] E. Nikolla, A. Holewinski, J. Schwank, and S. Linic. Controlling carbon surface chemistry by alloying: Carbon tolerant reforming catalyst. *J. Am. Chem. Soc.*, 128(35):11354–11355, 2006.
- [18] J. Rodriguez. The chemical properties of bimetallic surfaces: Importance of ensemble and electronic effects in the adsorption of sulfur and SO₂. *Progress in Surface Science*, 81(4):141, 2006.
- [19] M. Chen, Y. Cai, Z. Yan, K. Gath, S. Axnanda, and D. Goodman. Highly active surfaces for CO oxidation on Rh, Pd, and Pt. *Surface Science*, 601(23):5326 – 5331, 2007.
- [20] B. Gould, A. Tadd, and J. Schwank. Nickel-catalyzed autothermal reforming of jet fuel surrogates: n-dodecane, tetralin, and their mixture. *Journal of Power Sources*, 164(1):344, 2007.
- [21] B. Gould, X. Chen, and J. Schwank. Dodecane reforming over nickel-based monolith catalysts. *Journal of Catalysis*, 250(2):209–221, 2007.
- [22] K. Sato and K. Fujimoto. Development of new nickel based catalyst for tar reforming with superior resistance to sulfur poisoning and coking in biomass gasification. *Catalysis Communications*, 8(11):1697, 2007.
- [23] J. Rostrup-Nielsen. Catalytic steam reforming. *Catalysis: Science and Technology*, 5:1–117, 1984.

- [24] S. Helveg, C. Lopez-Cartez, J. Sehested, P. Clausen, J. Rostrup-Nielsen, F. Abild-Pedersen, and J. Nørskov. Atomic scale imaging of carbon nanofiber growth. *Nature*, 427:426–429, 2004.
- [25] A. Huczko. Synthesis of aligned carbon nanotubes. *Applied Physics A: Materials Science & Processing*, 74(5):617, 2002.
- [26] M. Ibe, S. Gomez, K. Malinger, P. Fanson, and S. Suib. Microwave-assisted desulfurization of NO_x storage-reduction catalyst. *Applied Catalysis B: Environmental*, 69(3-4):235–239, 2006.
- [27] T. Davidian, N. Guilhaume, E. Iojoiu, H. Provendier, and C. Mirodatos. Hydrogen production from crude pyrolysis oil by a sequential catalytic process. *Applied Catalysis B: Environmental*, 73(1-2):116, 2007.
- [28] J. Wan and M. Depew. The potential of microwave induced catalytic process: A recent revisit. *Ceramic Transactions*, 111(Microwaves):241, 2001.
- [29] H. Puschner. *Heating With Microwaves*. Springer-Verlag New York Inc., New York, 1966.
- [30] T. Chen. Relative transparency of minerals to microwave radiation. *Canadian Metallurgical Quarterly*, 23(3):349, 1984.
- [31] A. Baulig. Microwave drying of ceramic materials on a laboratory scale. Measurement technology background. *ZI International*, 43(7):386, 1990.
- [32] Z. Xie, J. Yang, X. Huang, and Y. Huang. Microwave processing and properties of ceramics with different dielectric loss. *Journal of the European Ceramic Society*, 19(3):381–387, 1999.
- [33] M. Arai, J. Binner, G. Carr, and T. Cross. High temperature dielectric measurements on ceramics. In *Dielectric Materials, Measurements and Applications, 1992., Sixth International Conference*, pages 69–72, Sep 1992.
- [34] M. Gupta and E. Wong Wai Leong. *Microwaves and Metals*. John Wiley & Sons (Asia), Singapore, 2007.
- [35] G. Viau, F. Ravel, O. Acher, F. Fievet-Vincent, and F. Fievet. Preparation and microwave characterization of spherical and monodisperse Co—Ni particles. *Journal of Magnetism and Magnetic Materials*, 140-144(Part 1):377, 1995.
- [36] G. Viau, F. Fievet-Vincent, F. Fievet, P. Toneguzzo, F. Ravel, and O. Acher. Size dependence of microwave permeability of spherical ferromagnetic particles. *Journal of Applied Physics*, 81(6):2749–2754, 1997.
- [37] D. Agrawal. Metal parts from microwaves. *Materials World*, 7(11):672, 1999.

- [38] D. Zhao, Y. Liu, and Z. Shen. Microwave permittivity and permeability of Ni-coated carbon nanotube/polymer composites. *Key Engineering Materials*, 334:681–684, 2007.
- [39] V. Palma, M. D’Amore, P. Russo, A. D’Arco, and P. Ciambelli. Regeneration of a soot-trap ceramic foam by a single-mode microwave cavity. *Combustion Science and Technology*, 174(11):295 – 308, 2002.
- [40] A. Harutyunyan, B. Pradhan, J. Chang, G. Chen, and P. Eklund. Purification of single-wall carbon nanotubes by selective microwave heating of catalyst particles. *J. Phys. Chem. B*, 106(34):8671–8675, 2002.
- [41] H. Chen, H. Lee, S. Chen, Y. Chao, and M. Chang. Review of plasma catalysis on hydrocarbon reforming for hydrogen production: Interaction, integration, and prospects. *Applied Catalysis B: Environmental*, 85(1-2):1–9, 2008.
- [42] M. Heintze and B. Pietruszka. Plasma catalytic conversion of methane into syngas: the combined effect of discharge activation and catalysis. *Catalysis Today*, 89(1-2):21, 2004.
- [43] O. Mutaf-Yardimci. *Plasma Catalysis in Hydrocarbon Processing by Using Non-Equilibrium Plasma Discharges*. University of Illinois at Chicago, 2001.
- [44] H. Nagazoe, M. Kobayashi, T. Yamaguchi, H. Kimuro, and K. Onoe. Characteristics of methane conversion under combined reactions of solid catalyst with microwave plasma. *J. Chem. Eng. Japan*, 39:314–320, 2006.
- [45] T. Oberreuther, C. Wolff, and A. Behr. Chemicals from carbon dioxide in a technical scale low temperature plasma reactor from the chemical engineering viewpoint. *IEEE 29th International Conference on Plasma Science*, page 133, 2002.
- [46] X. Wang, A. Wang, N. Li, X. Wang, Z. Liu, and T. Zhang. Reduction of SO₂ by CO under plasma-assisted catalytic system induced by microwave. *Catalysis Letters*, 109(1):109, 2006.
- [47] Y. Wang, C. Tsai, W. Chang, and Y. Kuo. Methane steam reforming for producing hydrogen in an atmospheric-pressure microwave plasma reactor. *International Journal of Hydrogen Energy*, 35(1):135–140.
- [48] L. Xiang, L. Xu, R. Xuzao, B. Meigui, D. Xiaoyan, and Y. Yongxiang. Carbon dioxide reforming of methane to syngas by warm plasma: Low energy consumption. In *Power and Energy Engineering Conference (APPEEC), 2010 Asia-Pacific*, pages 1–5.
- [49] R. Roy, D. Agrawal, J. Cheng, and S. Gedevanishvili. Full sintering of powdered-metal bodies in a microwave field. *Nature*, 399(6737):668, 1999.

- [50] K. Saitou. Microwave sintering of iron, cobalt, nickel, copper and stainless steel powders. *Scripta Materialia*, 54(5):875, 2006.
- [51] R. Meredith. *Engineers' Handbook of Industrial Microwave Heating*. Power Series 25. The Institution of Electrical Engineers, Exeter, 1998.
- [52] A. Metaxas. Applicators for industrial microwave processing. *Ceramic Transactions*, 36(Microwaves):549, 1993.
- [53] K. Takatsu, F. Kurogi, and M. Kasaya. Development of the microwave heated catalyst system. *JSAE Review*, 20(3):431, 1999.
- [54] E. Thostenson and T. Chou. Microwave processing: fundamentals and applications. *Composites Part A: Applied Science and Manufacturing*, 30(9):1055, 1999.
- [55] C. Ovalles, A. Morales, L. Rivas, and N. Urbano. Microwave heated catalyst and process, 2000.
- [56] C. Kappe and D. Dallinger. Controlled microwave heating in modern organic synthesis: highlights from the 2004-2008 literature. *Molecular Diversity*, 13(2):71–193, 2009.
- [57] T. Chan and H. Reader. *Understanding Microwave Heating Cavities*. Artech House Inc., Norwood MA., 2000.
- [58] S. Kalhori, B. Minaev, S. Stone-Elander, and N. Elander. Quantum chemical model of an S_{N2} reaction in a microwave field. *J. Phys. Chem. A*, 106(37):8516–8524, 2002.
- [59] A. Metaxas. *Foundations of Electroheat; A Unified Approach*. John Wiley & Sons, New York, 1996.
- [60] S. Orfandis. Electromagnetic waves and antennas, March 20 2008.
- [61] J. Walkiewicz. Microwave heating characteristics of selected minerals and compounds. *Minerals & metallurgical processing*, 5(1):39, 1988.
- [62] J. Thomas. Particle size effect in microwave-enhanced catalysis. *Catalysis Letters*, 49(3):137–141, 1997.
- [63] F. Ament and E. Gonze. Microwave regenerated diesel particulate trap, 2002.
- [64] F. Ament, E. Gonze, and M. Paratore. Catalyst temperature control via microwave-induced partial oxidation, 2004.
- [65] V. Palma, P. Russo, G. Matarazzo, and P. Ciambelli. Microwave improvement of catalyst performance in soot oxidation without additives. *Applied Catalysis B: Environmental*, 70(1-4):254, 2007.

- [66] J. Beckers, L. Zande, and G. Rothenberg. Clean diesel power via microwave susceptible oxidation catalysts. *Chem Phys Chem*, 7(3):747–755, 2006.
- [67] F. Walton and R. Kempster. Method and apparatus for detecting soot concentration in particulate trap. 5,157,340, 1992.
- [68] A. Knitt and M. DeCou. Radio frequency particulate sensing system. 7,253,641, 2007.
- [69] X. Zhang, C. Lee, D. Mingos, and D. Hayward. Carbon dioxide reforming of methane with Pt catalysts by using microwave dielectric heating. *Catalysis Letters*, 88(3):129, 2003.
- [70] M. Turner, R. Laurence, K. Yngvesson, C. Conner, F. Melo, S. Mendioroz, A. Corma, and J. Fierro. *Studies in Surface Science and Catalysis: Microwave effects in exhaust catalysis*, volume 130, Part 2, page 1625. Elsevier, 2000.
- [71] M. Turner, R. Laurence, K. Yngvesson, and W. Conner. The effect of microwave energy on three-way automotive catalysts poisoned by SO₂. *Catalysis Letters*, 71(3):133, 2001.
- [72] Y. Zhang-Steenwinkel, H. Castricum, J. Beckers, E. Eiser, and A. Blik. Dielectric heating effects on the activity and SO₂ resistance of La_{0.8}Ce_{0.2}MnO₃ perovskite for methane oxidation. *Journal of Catalysis*, 221(2):523, 2004.
- [73] S. Vallee and W. Conner. Microwaves and sorption on oxides: a surface temperature investigation. *J. Phys. Chem. B*, 110(31):15459–15470, 2006.
- [74] S. Kobayashi, Y. Kim, C. Kenmizaki, S. Kushiyama, and K. Mizuno. Control of adsorption by microwave irradiation. *Chemistry Letters*, (9):769–770, 1996.
- [75] R. Guerneur and C. Jacolin. Influence of surface silanols on the dielectric properties of nitrogen adsorbed on activated silica. *Surface Science*, 315(3):323, 1994.
- [76] L. Villegas, F. Masset, and N. Guilhaume. Wet impregnation of alumina-washcoated monoliths: effect of the drying procedure on Ni distribution and on autothermal reforming activity. *Applied Catalysis A: General*, 320:43, 2007.
- [77] J. Thiebaut, G. Roussy, M. Medjram, F. Garin, L. Seyfried, and G. Maire. Durable changes of the catalytic properties of alumina-supported platinum induced by microwave irradiation. *Catalysis Letters*, 21(1-2):133–138, 1993.
- [78] Y. Pan, C. Liu, and P. Shi. Preparation and characterization of coke resistant Ni/SiO₂ catalyst for carbon dioxide reforming of methane. *Journal of Power Sources*, 176(1):46, 2008.
- [79] P. Reddy, N. Seshu Babu, N. Pasha, N. Lingaiah, and P. Sai Prasad. Influence of microwave irradiation on catalytic decomposition of nitrous oxide over Rh/Al₂O₃ catalyst. *Catalysis Communications*, 9(14):2303–2307, 2008.

- [80] G. Roussy, S. Hilaire, J. Thibaut, G. Maire, F. Garin, and S. Ringler. Permanent change of catalytic properties induced by microwave activation on 0.3% Pt/Al₂O₃ (EuroPt-3) and on 0.3% Pt-0.3% Re/Al₂O₃ (EuroPt-4). *Applied Catalysis A: General*, 156(2):167, 1997.
- [81] G. Roussy, E. Marchal, J. Thiebaut, A. Kiennemann, and G. Maire. C₂+ selectivity enhancement in oxidative coupling of methane over microwave-irradiated catalysts. *Fuel Processing Technology*, 50(2-3):261, 1997.
- [82] L. Seyfried, F. Garin, G. Maire, J. Thiebaut, and G. Roussy. Microwave electromagnetic-field effects on reforming catalysts: 1. Higher selectivity in 2-methylpentane isomerization on alumina-supported Pt catalysts. *Journal of Catalysis*, 148(1):281, 1994.
- [83] F. Gokaliler, B. Selen Caglayan, Z. Ilse Onsan, and A. Erhan Aksoylu. Hydrogen production by autothermal reforming of LPG for PEM fuel cell applications. *International Journal of Hydrogen Energy*, 33(4):1383–1391, 2008.
- [84] M. Westbrook. *The Electric Car*. The Institute of Electrical Engineers, London, 2001.
- [85] R. Farrauto and R. Heck. Catalytic converters: state of the art and perspectives. *Catalysis Today*, 51(3-4):351, 1999.
- [86] T. Nijhuis, A. Beers, T. Vergunst, I. Hoek, F. Kapteijn, and J. Moulijn. Preparation of monolithic catalysts. *Catalysis Reviews: Science and Engineering*, 43(4):345 – 380, 2001.
- [87] R. Heck and R. Farrauto. Automobile exhaust catalysts. *Applied Catalysis A: General*, 221(1-2):443, 2001.
- [88] B. Gould, X. Chen, and J. Schwank. n-Dodecane reforming over nickel-based monolith catalysts: deactivation and carbon deposition. *Applied Catalysis A: General*, 334(1-2):277–290, 2008.
- [89] X. Chen, B. Gould, and J. Schwank. n-Dodecane reforming over monolith-based Ni catalysts: SEM study of axial carbon distribution profile. *Applied Catalysis A: General*, 356(2):137–147, 2009.
- [90] C. Agrafiotis, A. Tsetsekou, and A. Ekonomakou. The effect of particle size on the adhesion properties of oxide washcoats on cordierite honeycombs. *Journal of Materials Science Letters*, 18(17):1421–1424, 1999.
- [91] B. Mitra. Washcoating of different zeolites on cordierite monoliths. *Journal of the American Ceramic Society*, 91(1):64–70, 2008.
- [92] J. Zamaro, M. Ulla, and E. Mir. Zeolite washcoating onto cordierite honeycomb reactors for environmental applications. *Chemical Engineering Journal*, 106(1):25–33, 2005.

- [93] M. Stutz and D. Poulidakos. Optimum washcoat thickness of a monolith reactor for syngas production by partial oxidation of methane. *Chemical Engineering Science*, 63(7):1761 – 1770, 2008.
- [94] A. Metaxas and R. Meredith. *Industrial Microwave Heating*. IEE Power Engineering Series 4. Peter Peregrinus Ltd. on behalf of the Institution of Electrical Engineers, London, 1983.
- [95] Steven E. Edmund. Matlab File Exchange, <http://www.mathworks.com/matlabcentral/fileexchange/authors/37220>.
- [96] J. Mayne. *Influence of Sulfur on Liquid Fuel Reforming*. 2010. Dissertation (Ph.D.)—University of Michigan.
- [97] NIST chemistry webbook, <http://webbook.nist.gov/chemistry/>.
- [98] D. Goodman. Chemical modification of chemisorptive and catalytic properties of nickel. *Applications of Surface Science*, 19(1-4):1–13, 1984.
- [99] C. Bartholomew. Mechanisms of nickel catalyst poisoning. In B. Delmon and G. Froment, editors, *Catalyst Deactivation 1987 Proceedings of the 4th International Symposium*, volume 34 of *Studies in Surface Science and Catalysis*, pages 81–104. Elsevier, 1987.
- [100] J. Rostrup-Nielsen and I. Alstrup. Ensemble control by sulfur poisoning of nickel catalysts for steam reforming. In J. Ward, editor, *Catalysis 1987 Proceedings of the 10th North American Meeting of the Catalysis Society*, volume 38 of *Studies in Surface Science and Catalysis*, pages 725–732. Elsevier, 1988.
- [101] J. Rostrup-Nielsen and K. Pedersen. Sulfur poisoning of Boudouard and methanation reactions on nickel catalysts. *Journal of Catalysis*, 59(3):395–404, 1979.
- [102] J. Butt. Catalyst poisoning and chemical process dynamics. In B. Delmon and G. Froment, editors, *Catalyst Deactivation*, volume 6 of *Studies in Surface Science and Catalysis*, pages 21–41. Elsevier, 1980.
- [103] P. Fanson, H. Hirata, M. Ibe, S. Suib, S. Gomez, and K. Maling. Microwave assisted desulfurization of nitrogen oxide storage reduction catalysts, 2006.
- [104] J. Mayne, A. Tadd, K. Dahlberg, and J. Schwank. Influence of thiophene on the isooctane reforming activity of Ni-based catalysts. *Journal of Catalysis*, 271(1):140–152, 2010.
- [105] N. Elander, J. Jones, S. Lu, and S. Stone-Elander. Microwave-enhanced radiochemistry. *Chemical Society reviews*, 29(4):239, 2000.
- [106] C. Kappe. Controlled microwave heating in modern organic synthesis. *Angewandte Chemie International Edition*, 43(46):6250–6284, 2004.

- [107] T. Durka et al. On the accuracy and reproducibility of fiber optic (FO) and infrared (IR) temperature measurements of solid materials in microwave applications. *Measurement Science and Technology*, 21(4):045108, 2010.
- [108] H. Ramaswamy. Evaluation of shielded thermocouples for measuring temperature of foods in a microwave oven. *Journal of Food Science and Technology*, 35(4):325, 1998.
- [109] R. Rice and D. Do. *Applied Mathematics and Modeling for Chemical Engineers*. John Wiley & Sons, Inc., New York, 1995.
- [110] B. Bird, W. Stewart, and E. Lightfoot. *Transport Phenomina*. John Wiley & Sons, Inc., New York, 2nd edition, 2002.
- [111] W. Perry, D. Cooke, J. Katz, and A. Datye. On the possibility of a significant temperature gradient in supported metal catalysts subjected to microwave heating. *Catalysis Letters*, 47(1):1, 1997.
- [112] S. Lee and R. Aris. On the effects of radiative heat transfer in monoliths. *Chemical Engineering Science*, 32(8):827–837, 1977.
- [113] A. Boehman. Radiation heat transfer in catalytic monoliths. *AIChE Journal*, 44:12, 1998.
- [114] E. Schmidbauer and P. Mirwald. Electrical conductivity of cordierite. *Mineralogy and Petrology*, 48(2):201–214, 1993.
- [115] G. Chiodelli, G. Flor, and M. Scagliotti. Electrical properties of the ZrO₂-CeO₂ system. *Solid State Ionics*, 91(12):109–121, 1996.
- [116] B. Lu, X. Dong, H. Huang, X. Zhang, X. Zhu, J. Lei, and J. Sun. Microwave absorption properties of the core/shell-type iron and nickel nanoparticles. *Journal of Magnetism and Magnetic Materials*, 320(6):1106–1111, 2008.
- [117] M. Yousuf, P. Sahu, and K. Rajan. High-pressure and high-temperature electrical resistivity of ferromagnetic transition metals: nickel and iron. *Physical Review B*, 34:8086–8100, December 1986.
- [118] W. Tang, H. Bosman, Y. Lau, and R. Gilgenbach. The Ohmic heating of particulates in a lossless medium. *Journal of Applied Physics*, 97(11):114915, 2005.
- [119] J. Tannehill, D. Anderson, and R. Pletcher. *Computational Fluid Mechanics and Heat Transfer*. Taylor & Francis, Philadelphia, PA, 2nd edition, 1997.
- [120] S. Edmund and J. Maneval. *Nuclear Magnetic Resonance Measurements of Fluid-Solid Interactions in Dialysis-Membrane Materials*. PhD thesis, Bucknell University, 2007.

- [121] P. Berlowitz, C. Peden, and D. Goodman. *J. Phys. Chem*, 92:5213, 1988.
- [122] D. Logan and M. Paffett. *J. Catal.*, 133:179, 1992.
- [123] J. Szanyi and D. Goodman. CO oxidation on palladium. 1. A combined kinetic-infrared reflection absorption spectroscopic study of Pd(100). *Journal of Physical Chemistry*, 98(11):2972–2977, 1994.
- [124] T. Engel and G. Ertl. A molecular beam investigation of the catalytic oxidation of CO on Pd(111). *The Journal of Chemical Physics*, 69(3):1267–1281, 1978.
- [125] L. Kieken and M. Boudart. Rate of oxidation of CO on Pd at pressure between 10^{-1} and 10^2 mbar. *Catalysis Letters*, 17:1–10, 1993.
- [126] S. Landry, R. Betta, J. Lfi, and M. Boudart. *Journal of Physical Chemistry*, 94:1203, 1990.
- [127] J. Hoffmann, S. Schauermaun, J. Hartmann, V. Zhdanov, B. Kasemo, J. Libuda, and H. Freund. Nanofacet-resolved CO oxidation kinetics on alumina-supported Pd particles. *Chemical Physics Letters*, 354, 2002.
- [128] Z. Wang, B. Li, M. Chen, W. Weng, and H. Wan. Size and support effects for CO oxidation on supported Pd catalysts. *Science China Chemistry*, 53:2047–2056, 2010.
- [129] X. Xueping and D. Goodman. An infrared and kinetic study of CO oxidation on model silica-supported palladium catalysts from 10^{-9} to 15 Torr. *Journal of Physical Chemistry*, 97:7711–7718, 1993.
- [130] A. Allian, K. Takanabe, K. Fujidala, X. Hao, T. Truex, J. Cai, C. Buda, M. Neurock, and E. Iglesia. Chemisorption of CO and mechanism of CO oxidation on supported platinum nanoclusters. *Journal of the American Chemical Society*, 133(12):4498–4517, 2011.
- [131] R. Nibbelke, M. Campman, J. Hoebink, and G. Marin. Kinetic study of the CO oxidation over Pt/Al₂O₃ and Pt/Rh/CeO₂/Al₂O₃ in the presence of H₂O and CO₂. *Journal of Catalysis*, 171(2):358–373, 1997.
- [132] R. Nibbelke, A. Nievergeld, J. Hoebink, and G. Marin. Development of a transient kinetic model for the CO oxidation by O₂ over a Pt/Rh/CeO₂/Y-Al₂O₃ three-way catalyst, 1998.
- [133] K. Zorn, S. Giorgio, E. Halwax, C. Henry, H. Gronbeck, and G. Rupprechter. CO oxidation on technological Pd/Al₂O₃ catalysts: Oxidation state and activity. *The Journal of Physical Chemistry C*, 115(4):1103–1111, 2011.
- [134] A. Galwey, D. Bettany, and M. Mortimer. Kinetic compensation effects observed during oxidation of carbon monoxide on alumina supported palladium, platinum, and rhodium metal catalysts: toward a mechanistic explanation. *International Journal of Chemical Kinetics*, 38(11):689–702, 2006.

- [135] L. Piccolo, C. Becker, and C. Henry. Kinetic modeling of the CO oxidation reaction on supported metal clusters. *The European Physical Journal D - Atomic, Molecular, Optical and Plasma Physics*, 9:415–419, 1999.
- [136] M. Eriksson and L. Petersson. Spillover of hydrogen, oxygen and carbon monoxide in oxidation reactions on SiO₂ supported Pd. *Surface Science*, 311(12):139–152, 1994.
- [137] S. Ladas, H. Poppa, and M. Boudart. The adsorption and catalytic oxidation of carbon monoxide on evaporated palladium particles. *Surface Science*, 102(1):151–171, 1981.
- [138] H. Conrad, G. Ertl, J. Kuppers, and E. Latta. Interaction of NO and O₂ with Pd(111) surfaces. *Surface Science*, 65(1):235–244, 1977.
- [139] J. Fischer-Wolfarth, J. Farmer, J. Flores-Camacho, A. Genest, I. Yudanov, N. Rösch, C. Campbell, S. Schauermaun, and H. Freund. Particle-size dependent heats of adsorption of CO on supported Pd nanoparticles as measured with a single-crystal microcalorimeter. *Phys. Rev. B*, 81:241416, Jun 2010.
- [140] S. McClure and D. Goodman. New insights into catalytic CO oxidation on Pt-group metals at elevated pressures. *Chemical Physics Letters*, 469(13):1–13, 2009.
- [141] T. Matsushima, C. Mussett, and J. White. The adsorption of carbon monoxide on palladium during the catalyzed reaction $\text{CO} + 1/2\text{O}_2 \rightarrow \text{CO}_2$. *Journal of Catalysis*, 41(3):397–404, 1976.
- [142] M. Bowker. Automotive catalysis studied by surface science. *Chemical Society Reviews*, 37(10):2204–2211, 2008.
- [143] S. Joshi, M. Harold, and V. Balakotaiah. Overall mass transfer coefficients and controlling regimes in catalytic monoliths. *Chemical Engineering Science*, 65(5):1729–1747, 2010.
- [144] D. Roth, P. Gelin, M. Primet, and E. Tena. Catalytic behaviour of Cl-free and Cl-containing Pd/Al₂O₃ catalysts in the total oxidation of methane at low temperature. *Applied Catalysis A: General*, 203(1):37–45, 2000.
- [145] S. Ladas, R. Imbihl, and G. Ertl. Kinetic oscillations during the catalytic CO oxidation on Pd(110): the role of subsurface oxygen. *Surface Science*, 219:88–106, 1989.
- [146] G. Ertl. Self-organization in reactions at surfaces. *Surface Science*, 287288, Part 1(0):1–11, 1993.
- [147] M. Ehsasi, M. Berdau, T. Rebitzki, K. Charlé, K. Christmann, and J. Block. A reactive phase diagram of CO oxidation on Pd(110): steady and oscillatory states. *The Journal of Chemical Physics*, 98(11):9177–9184, 1993.

- [148] J. Szanyi, W. Kuhn, and D. Goodman. CO oxidation on palladium: 2. A combined kinetic-infrared reflection absorption spectroscopic study of Pd(111). *Journal of Physical Chemistry*, 98:2978–2981, 1994.
- [149] J. Schwank and S. Edmund. Use of microwave energy to remove contaminating deposits from a catalyst. US 2011/0118105 A1, 2011.
- [150] D. Harris. *Quantitative Chemical Analysis*. W. H. Freeman and Company, 6th edition, 2003.